Surface and interface characterization of thin-film silicon solar cell structures

Von der Fakultät für Mathematik, Naturwissenschaften und Informatik
der Brandenburgischen Technischen Universität Cottbus

zur Erlangung des akademischen Grades

Doktor der Naturwissenschaften
(Dr. rer. nat.)

genehmigte Dissertation

vorgelegt von

Diplom-Physiker

Dominic Gerlach

geboren am 2.4.1984 in Hildesheim

Gutachter: Prof. Dr. Marcus Bär

Gutachter: Prof. Dr. Bernd Rech

Gutachter: Prof. Dr. Dieter Schmeißer

Tag der mündlichen Prüfung: 21. Februar 2013

Abstract

The properties of Si thin films for solar cells, the interaction with different substrates and the influence of dopants are examined with synchrotron based x-ray spectroscopy – primarily x-ray emission spectroscopy (XES) and hard x-ray photoelectron spectroscopy (HAXPES). The films are studied as-deposited (i.e., amorphous, a-Si) and after conversion into polycrystalline (poly-Si) employing solid phase crystallization (SPC).

Si $L_{2,3}$ XES spectra of thin-film Si samples can be described by a superposition of a-Si and monocrystalline Si-wafer (c-Si) reference spectra. According to a quantification based on that superposition principle, none of the investigated samples are completely crystallized – a measurable a-Si component always remains (5-20 %) regardless of deposition and treatment conditions. Based on additional results from electron back scattering diffraction different models are developed which may explain this finding. According to these models, the remnant a-Si component can be attributed to amorphous/disordered material at the grain boundaries. Using one of these models, the thickness of this grain-surrounding material s could be approximated to be (1.5 ± 0.5) nm.

Further investigations of the SPC process reveal a faster crystallization for boron-doped samples, and a slower crystallization for phosphorous-doped samples, when compared to the crystallization of undoped a-Si:H thin films. The peculiarities of B K XES spectra (and observed changes upon SPC) indicate that boron could act as a nucleation center promoting crystallization. Si $L_{2,3}$ XES spectra of a-Si:H and P-doped poly-Si exhibit spectral features above the valence band maximum at 100 eV that could be attributed to a-Si defect states and n^+-dopant states, respectively.

The SPC crystallization velocity of Si thin films on ZnO:Al/glass is found to be faster than that on SiN_x/glass substrate. Multiple indications for oxidization at the poly-Si/ZnO:Al interface are found based on our Si $L_{2,3}$ XES analysis. Spatially resolved x-ray photoelectron spectroscopy data support this and even suggest the formation of sub-oxides or zinc silicate as an interface species.

The electronic structure of the buried a-SiO_x:H(B)/ZnO:Al and µc-Si:H(B)/ZnO:Al interfaces are unraveled with “depth resolved” hard x-ray photoelectron spectroscopy. A surface band

bending limited to the very surface of the silicon layers is found. The valence band maxima for the Si cover layers and the ZnO:Al TCO are determined and interface induced band bending for both interfaces are derived. At the a-SiO_x:H(B)/ZnO:Al interface a tunnel barrier of (0.22 ± 0.31) eV and at µc-Si:H(B)/ZnO:Al interface a tunnel barrier of (-0.08 ± 0.31) eV is determined. This explains a previously empirically found solar cell efficiency increase produced by introducing a µc-Si:H(B) buffer layer between an a-Si p-i-n cell and the ZnO:Al/glass substrate.

Contents

1. Introduction

Most of the currently produced solar cell modules are based on crystalline silicon wafer technology that depends on a high energy process [i.e., Czochalsky crystal growth to produce monocrystalline Si (c-Si) or cooling of molten Si to produce multicrystalline Si (mc-Si)]. From this raw material, Si wafers are cut with wire saws, which results in waste material. Although high efficiencies can be reached (record module efficiencies η: c-Si: 22.9%; mc-Si: 18.5% [1]), relatively thick layers are necessary (~200 µm) to absorb the light due to the fact that silicon is an indirect semiconductor.

To reduce the use of material and energy and therefore module prices, thin-film solar cells have been under development and in production over the last decades. Instead of cutting wafers from crystalline raw material, thin films are deposited onto carrier substrates such as glass. Direct semiconductors like cadmium telluride (CdTe), copper indium gallium selenide (CIGSe) and amorphous silicon (a-Si) have a higher absorption coefficient than crystalline Si and thus µm thin layers are sufficient to absorb most of the incoming light.

Although solar cells based on CIGSe (record lab-scale efficiencies η = 20.3% [1]) and CdTe (η = 17.3% [1]) result in higher efficiencies than those based on a-Si (η = 10.1% [2]), Si has the advantage of non-toxicity and earth-abundance. One major disadvantage of a-Si is the degradation of the efficiency upon illumination (also known as Staebler-Wronsky effect [3]) which causes decreases of up to 30 % in efficiency during the first 1000 hours of illumination [4].

Degradation is absent or only mildly present [5] in directly deposited small-grained Si layers. These layers are nanocrystalline Si (nc-Si) or microcrystalline Si (µc-Si) with grain sizes below 1 µm [6]. But grain boundaries usually act as recombination centers for the photogenerated charge carriers – therefore only similar record cell efficiencies as for a-Si are reached (η = 10.1% [1]). Another reason for the limited performance of these small-grained Si films, is that the absorber is again an indirect semiconductor, and thus it is essential to trap the

incoming light inside the film by specially designing the interfaces, which increases the optical path and thus absorption.

Highest efficiencies for Si thin films are currently only reached by combining a-Si and nc-Si into multijunction tandem cells. In these layered thin-film solar cells, a-Si forms the top and µc-Si (or nc-Si) the bottom cell. Due to their different band gaps, different parts of the solar spectrum can be absorbed efficiently in each cell, resulting in a current lab-scale cell record of $\eta = 12.4\%$ [1].

Recently, efforts were made to increase the grain size of the thin-film crystalline Si layers to decrease recombination at grain boundaries. This was achieved by converting amorphous Si films into polycrystalline silicon (poly-Si) by post deposition treatments. Examples of such treatments include solid phase crystallization (SPC, [7][8][9]), aluminum induced crystallization [10] and laser crystallization [11], resulting in grain sizes in the µm range.

The current world record poly-Si cell was processed with SPC and has an mini-module efficiency of $\eta = 10.5\%$ [12]. The respective device presented in 2007 by CSG Solar used a complex contact scheme to access the front contact of the cell.

Transparent conductive oxides (TCO) are typically used for contacting thin-film solar cells. One prominent representative of this material class is ZnO (used in the current world record a-Si cell by Benagli et. al. in 2009 [2]). Big advantages of ZnO is the chemical robustness during most deposition methods (especially plasma-enhanced chemical vapor deposition [PECVD]) and the easy to introduce light-trapping schemes by chemically etching the surface [13].

The implementation of aluminum-doped ZnO as a front contact for Si thin films has therefore been a focus of research at the Helmholtz-Zentrum Berlin für Materialien und Energie GmbH (HZB; for poly-Si cells) and Forschungszentrum Jülich (for a-Si/µc-Si tandem cells) in recent years. The optimization of SPC processes and development of faster a-Si deposition methods (e-beam deposition instead of PECVD) are current research topics.

Synchrotron-based x-ray spectroscopic methods have been developed over the last decades to investigate the chemical and electronic structure of surfaces, interfaces and bulk material. Due to the brightness of 3rd generation synchrotrons new x-ray emission based studies are

accessible and open new ways to reveal unknown aspects of even well-studied materials as silicon.

This thesis centers around the investigation of thin film a-Si, µc-Si and poly-Si and the properties of the interface to ZnO:Al employing different synchrotron based x-ray spectroscopies.

Chapter 2 describes the basic properties of the different thin film Si absorber materials, explains relevant deposition techniques and discusses post deposition treatment processes (especially SPC). At the end, different solar cell designs are presented.

Chapter 3 introduces the used x-ray spectroscopy methods, synchrotron radiation and describes the various experimental setups. A short introduction into Raman spectroscopy and electron backscattering microscopy is given.

Chapter 4 presents the x-ray emission (XES) and x-ray absorption spectroscopy (XAS) based investigation of the SPC process of hydrogenated a-Si (a-Si:H) and reveals influences of grain size, dopants and substrate on the degree and rate of crystallization of the a-Si films. Models for the distribution of residual a-Si at grains and grain boundaries in poly-Si are introduced and discussed.

Chapter 5 presents a study of the impact of SPC on the buried a-Si/ZnO:Al interface by XES and XAS as well as x-ray photoelectron emission microscopy (X-PEEM). Additional influences of hydrogen passivation on XES spectra are discussed, too.

Chapter 6 presents a hard x-ray photoelectron spectroscopy (HAXPES) investigation of the buried a-SiO_x:H(B)/ZnO:Al, and the µc-Si:H(B)/ZnO:Al interface. The band alignment at the tunnel junction is revealed, and the comparison of a-SiO_x and µc-Si was used to explain an empirically found efficiency gain brought about by using a µc-Si:H(B) buffer layer between a-SiO_x:H(B) and ZnO:Al.

2. Thin-film silicon solar cells

This chapter will introduce the basics of photovoltaic energy conversion using thin-film silicon solar cell absorbers. In particular, the focus will be the solar cell design and how it is changed by introducing a transparent conductive oxide front contact. In this thesis, it will be studied how and why this alternative solar cell design influences the solar cell performance.

2.1 Thin film silicon absorbers

Silicon absorber material can be differentiated into amorphous and crystalline Si, while crystalline Si can be differentiated further by grain size. Ranging from monocrystalline (c-Si) and multycrystalline (mc-Si) silicon with macroscopic grains [employed as wafers in the dominating PV technology to date] to microcrystalline (µc-Si) and nanocrystalline (nc-Si) silicon with µm and nm sized grains. Apart from that, the term polycrystalline silicon (poly-Si) is often used for material that has been produced by solid phase crystallization of amorphous silicon (a-Si).

2.1.1 Amorphous silicon (a-Si)

The following introduction to amorphous silicon (a-Si) is based on the text book by Street [14] and the PhD thesis of Tim Schulze [15] of HZB.

Amorphous materials are defined by their absence of long-range order. The short-range order between individual atoms is the same as for their crystalline counterpart. As crystalline Si, amorphous silicon mainly has a tetrahedral structure (fourfold coordination), but distances to nearest neighbors and binding angles vary slightly. Cumulative effects of these variations lead to a significant deviation from the long-range diamond structure in crystalline silicon.

The electronic structure in crystalline semiconductors is defined by the periodicity of the lattice. Bonding and antibonding hybrid orbitals form periodic Bloch waves that result in the electronic band structure and the E(k) dispersion relation. In amorphous semiconductors, however, a lattice is absent and the atoms rather form a tetrahedrally coordinated random-network structure [16]. Well-defined Bloch states therefore do not exist and the electronic structure is dominated by the molecular orbitals. Atomic 3s and 3p orbitals form molecular $3sp^3$ hybrid orbitals, which split into bonding and antibonding states in the solid. The valence band is represented by the bonding and the conduction band by the antibonding states. Due to the variation in atomic distances in the amorphous material, tails extend into the band gap and no abrupt valence and conduction band edge occurs. The resulting band structure is illustrated in Figure 2.1.

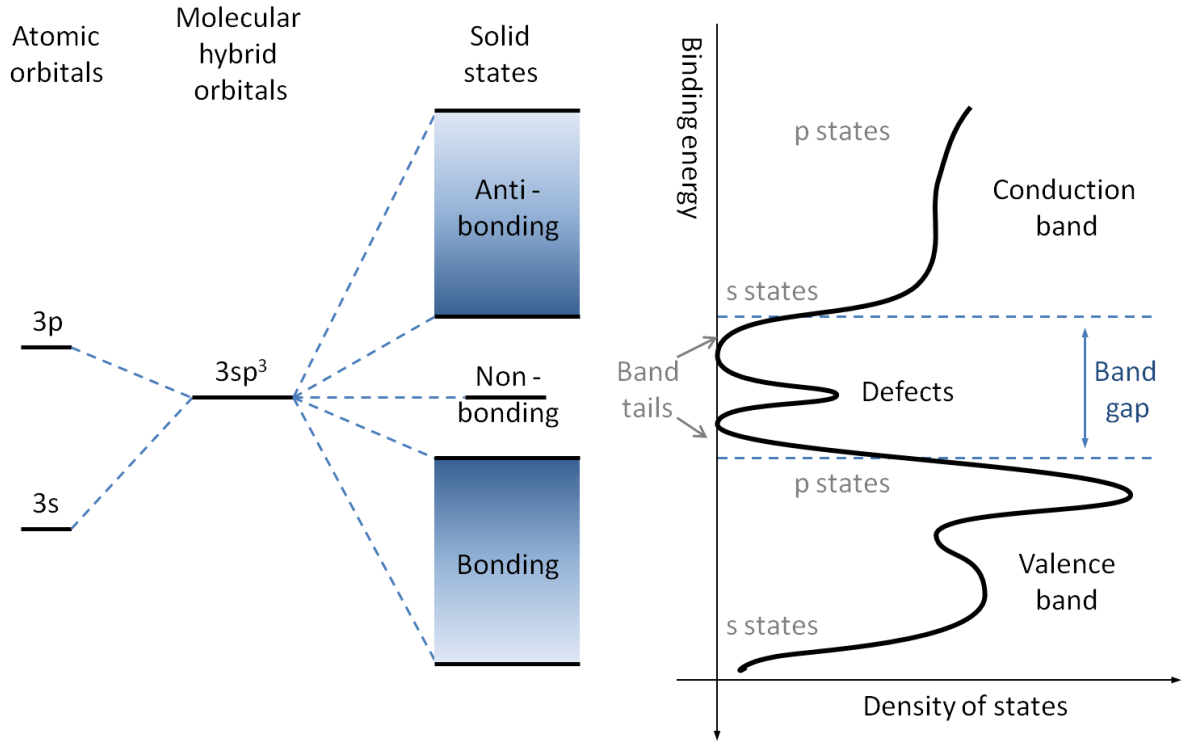

Figure 2.1: Schematic of the atomic and molecular orbitals that result in a band structure for amorphous silicon (redrawn from [14]).

The main defect in amorphous silicon originates from bonding defects that result in threefold coordinated silicon. These non-bonding sp^3 orbitals are called dangling bonds and form defect states inside the band gap. The dangling bond can be found in three charged states, depending on whether no, one or two electrons are contained. [Other known defects result from divacancies (twofold coordination), weak Si-Si bonds (fourfold coordination with deviating pair distances or binding angles) and floating bonds (fivefold coordination). All of these

defects, except of the weak Si-Si bond (that contributes to the band tails), result in states inside the gap [14]]. Hydrogen is included in amorphous silicon (a-Si:H) for the passivation of these dangling bonds [and other defect states]; it terminates the dangling bond and makes it electrically inactive.

Doping of amorphous Si is not as easily achieved as in crystalline Si because the dopant atoms cannot be substituted into a lattice and by doing so, contribute (remove) electrons. They are rather built into the random structure. The number of covalent bonds Z that are formed in the energetic optimum is described by the $Z = 8$ - N rule (with N being the number of valence electrons) and thus phosphorous (boron) is most likely to be bound in a threefold (fivefold) environment, which renders it inactive as dopants. Still, doping is possible with low doping efficiencies (ratio between mobile carriers concentration to dopant atom concentraton) in the order of 1%. This is understood for phosphorous doping by a neutral fourfold silicon Si_4^0 and a neutral threefold phosphorous P_3^0 reacting to a positively charged P_4^+ and a negatively charged dangling bond D^-. An analogous process is known for boron [17][18]. Due to the formation of dangling bonds, doping therefore increases the defect density.

2.1.2 Deposition methods

This subchapter describes the methods that were used to deposit amorphous silicon samples characterized in this thesis. Information was acquired from the text book of Street [14] and due to their work on the specific deposition chambers – from the PhD thesis of Tim Schulze [15] (for plasma-enhanced chemical vapor deposition) and Tobias Sontheimer [19] (for e-beam evaporation) of HZB.

Amorphous Si films can be either produced by physical vapor deposition (PVD; i.e., sputtering or e-beam evaporation) or chemical vapor deposition (CVD) methods. For this thesis electronic beam (e-beam) evaporation and plasma-enhanced chemical vapor deposition (PECVD) were used.

During PECVD hydrogen-diluted silane precursor is decomposed in a plasma and deposited onto the substrate to form hydrogenated amorphous silicon (a-Si:H). The plasma can be ignited by applying a RF voltage onto two surrounding electrode plates, as seen in Figure 2.2.

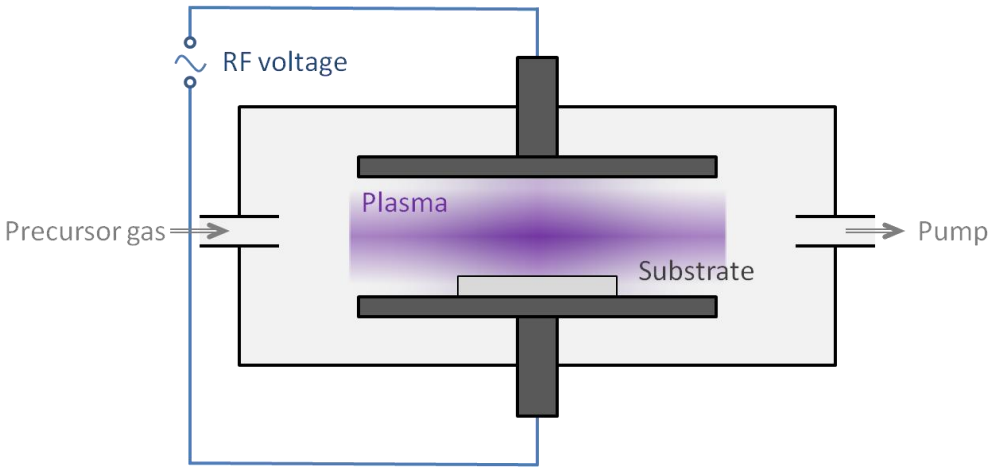

Figure 2.2: Schematic of a PECVD deposition chamber that uses electrode plates with an applied RF voltage to ignite the plasma (redrawn from [14][15]).

In a very simplified picture, silane (SiH_4) decomposes into a silyl (SiH_3) radical in the plasma, sticks to the surface and reacts with an existing dangling bond, resulting in an additional SiH group on the surface and a free H_2 molecule. The SiH group can react with another SiH_3, forming a dangling bond and free SiH_4 [20]. This process is very dependent on RF power, gas pressure, substrate temperature and hydrogen dilution. Highly diluted silane as well as high substrate temperatures result in ordered growth, forming nm- or µm-sized grains and therefore a nano- or microcrystalline structured silicon.

Doping is achieved by including additional substances into the precursor gas: For phosphorous doping, phosphine (PH_3) is common, while for boron doping diborane (B_2H_6) or trimethyl borate (TMB, $B(OCH_3)_3$) can be used.

For e-beam evaporation, an electron beam is accelerated onto a silicon target to evaporate Si onto a substrate. Figure 2.3 shows a schematic of a respective deposition chamber which was used for e-beam deposited samples described in this thesis.

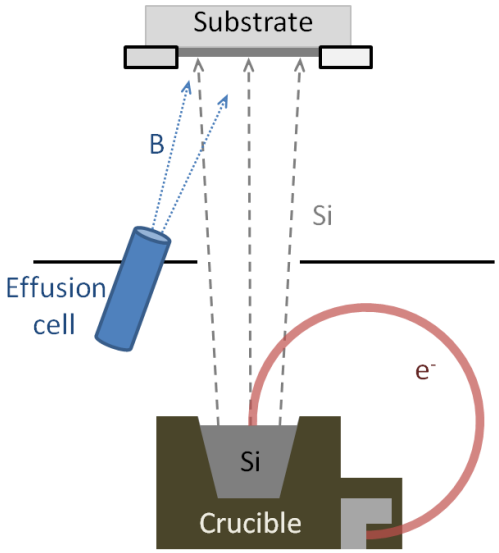

Figure 2.3: Schematic of an e-beam evaporation chamber (edited from [19])

A magnetic field is used to guide the 10 or 20 kV electron beam onto the crucible. To achieve p-doping, an effusion cell containing elemental boron is heated above 1600 °C. Rotating the substrate ensures uniform Si deposition and doping.

Due to the directional deposition of e-beam evaporation, shadowing effects occur and the resulting Si layers contain voids and usually have a columnar structure [21][22][23] which is a disadvantage over PECVD, where the plasma ensures a randomized deposition angle ensuring conformal growth even on rough substrates. In addition, SiH_3 radicals can also diffuses into the surface, to find and attach onto a dangling bond [24], healing existing voids. A big advantage of e-beam evaporation over PECVD is, however, the much higher deposition rates (20-30 times faster [25]).

Direct deposition of crystalline material by e-beam evaporation is possible by using substrate temperatures above 350 °C, which results in nanocrystalline layers. Towards even higher substrate temperatures (600 °C) the deposited silicon layer consists of bigger grains and thus is considered to be microcrystalline [19][26].

2.1.3 Polycrystalline silicon (solid phase crystallization)

In a solid phase crystallization (SPC) annealing process amorphous silicon is converted into polycrystalline silicon below the melting temperature of silicon. This is possible due to the

metastability of the amorphous silicon phase (the free energy of c-Si is lower than that of a-Si). The theory behind SPC is briefly addressed below, however, for more details refer to [19][27][28] and citations therein.

Assuming non-epitaxial growth without a seed layer, nucleation theory determines the crystallization process in the amorphous layer. In a first step, nucleation starts and forms a crystalline cluster of i atoms. The change in free energy ΔG_i due to this cluster can be expressed as [27]:

$$\Delta G_i = -\Delta g_{ac}\, i + \sigma_{ca}\, N_{if} \qquad \textbf{2.1}$$

with Δg_{ac} as the difference in free energy between the amorphous and the crystalline phases, σ_{ca} as the interface energy of each atom and N_{if} as the number of atoms at the crystalline-amorphous interface. The number of surface atoms N_{if} can be estimated by dividing the surface of a spherical cluster with radius R by the square of the atomic distance a and the number of atoms i, by dividing the cluster volume by the average atom volume [27]:

$$N_{if} = \frac{4\pi R^2}{a^2} \quad ; \quad i = \frac{4\pi R^3}{3a^3} \qquad \textbf{2.2}$$

With this, the change in free energy (equation 2.1) can be related to the radius of the cluster with the following relation:

$$\Delta G_i \propto -A\, R^3 + B\ R^2 \qquad \textbf{2.3}$$

with the constants A and B. With increasing cluster size R, the free energy therefore increases until a critical radius R_c (about 0.58 nm [27]) with ΔG^* is reached, the free energy increases upon cluster growth. As soon as R_c is surpassed, the decreasing free energy results in grain growth. Extrinsic effects like impurity atoms can alter the crystallization kinetics as well as heterogeneous effects at the interface to the substrate, resulting in a lower value for ΔG^* and therefore an increased nucleation at interfaces (the effects of impurity atoms can be seen in chapter 4.2 and those of substrates in chapter 4.4). Before the crystallization starts, a time lag can be observed [29].

2.2 Aluminum-doped zinc oxide as front contact

Aluminum-doped zinc oxide (ZnO:Al) is a transparent conductive oxide (TCO) often used in thin-film photovoltaics: It's advantages are high carrier mobility (45 cm^2/Vs [30]) and the ease with which it may be patterned to introduce light-trapping schemes by chemical etching [31][32]. A good overview on this material can be provided by the text book of Ellmer [13] and the PhD theses of Mark Wimmer of HZB [33] and Michael Berginski of FZ Jülich [34].

In this thesis highly n-doped ZnO:Al layers were examined as front contact in a-Si-, µc-Si- and poly-Si-based solar cell structures. If a semiconductor is highly n-doped, a shift of optical absorption to higher energies can be observed, which is called the Burstein-Moss effect [35][36]. It can be explained by electrons from doping states filling up the conduction band, resulting in a shift of the Fermi energy into the conduction band. This can be observed for aluminum doping of ZnO by the optical bandgap shifting from 3.3 eV for intrinsic ZnO [37][38] up to 3.9 eV [39][40] for high Al concentrations (2.1% Al; 4.5×10^{20} cm^3 [39]).

2.3 Solar cell devices

In a solar cell absorber photons with a higher energy than the band gap are absorbed by emitting an electron from the valence band into the conduction band (inner photoelectric effect [41]). The photogenerated electron-hole pair is separated by an internal voltage (build-in voltage) that is created by the pn-junction of the solar cell. To test the efficiency of a solar cell, it is usually illuminated with the AM1.5 light spectrum, which can be seen in Figure 2.4.

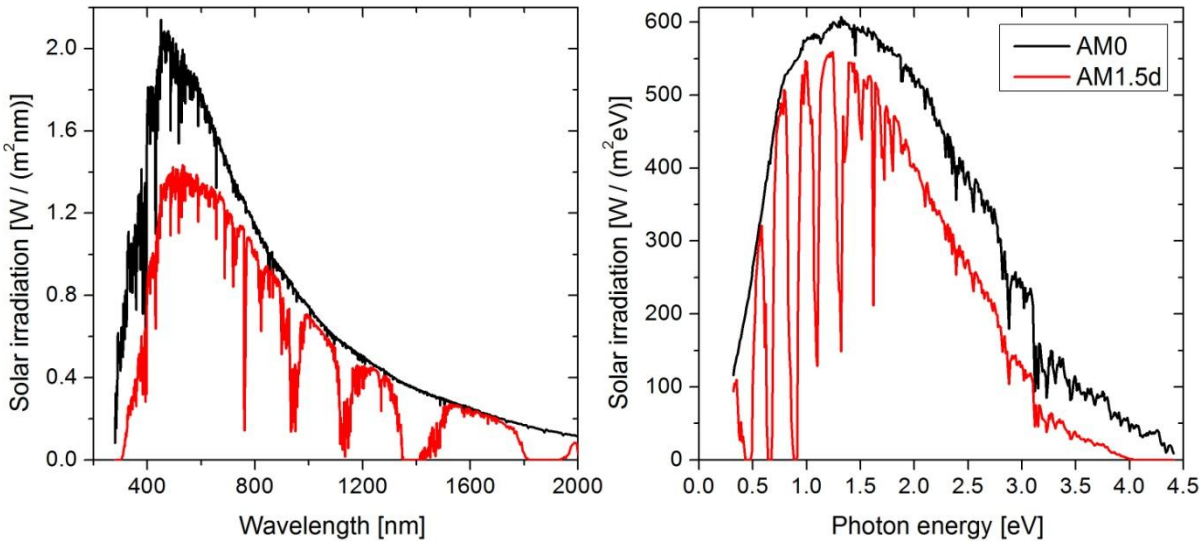

Figure 2.4: Reference solar irradiation spectra at the mean earth-sun distance (AM0 – extraterrestrial) and the direct AM1.5d spectrum over photon wavelength (data from [42]) and energy (table in [43]).

AM1.5 is the solar radiation that passes 1.5 times the atmosphere (48.2° incidence). The pass through the atmosphere results in loosing intensity through Raileigh scattering, Mie scattering and absorption due to atmospheric gas molecules. By measuring a current-voltage (J-V) curve under AM1.5 illumination at 25 °C, the efficiency of the solar cell is measured under standard-test conditions. Characteristic parameters are the open circuit voltage V_{oc} and the short circuit current density J_{sc}. The maximum electrical power $P_{el,max} = J_{mp} \times V_{mp}$ is produced at the maximum power point on the J-V curve, so that the efficiency of the cell is given with the illumination power P_{il} as:

$$\eta = \frac{P_{el,max}}{P_{il}} = \frac{J_{mp} \times V_{mp}}{P_{il}} = \frac{J_{sc} \times V_{oc} \times FF}{P_{il}} \qquad 2.4$$

here the fill factor is defined as: $FF \equiv (J_{mp} \times V_{mp})/(J_{sc} \times V_{oc})$. J-V curves can be seen in Figure 2.7 and Figure 6.1. For more details on the principal functions of solar cells the study of text books like that of Green [44] or Wagemann [45] is recommended.

Three solar cell device architectures are discussed in this subchapter: the a-Si:H p-i-n and a-Si p-i-n / µc-Si:H p-i-n tandem cell designs (based on [5]), and the poly-Si:H n^+-p^--p cell design (based on [7]).

Hydrogen-passivated amorphous silicon (a-Si:H) has proven to be a viable absorber material in single-junction solar cells (resulting in efficiencies of up to 10.1% [2]) as well as tandem

devices (resulting in efficiencies of up to 12.4% [46]). In the commonly-used p-i-n a-Si:H based homojunction solar cell structure, glass is used as a substrate, ZnO:Al forms the front contact of the device, followed by a thin highly p-doped, thick intrinsic and thin n-doped a-Si:H layer. The back contact consists of a ZnO:Al layer for light trapping and silver as seen in Figure 2.5.

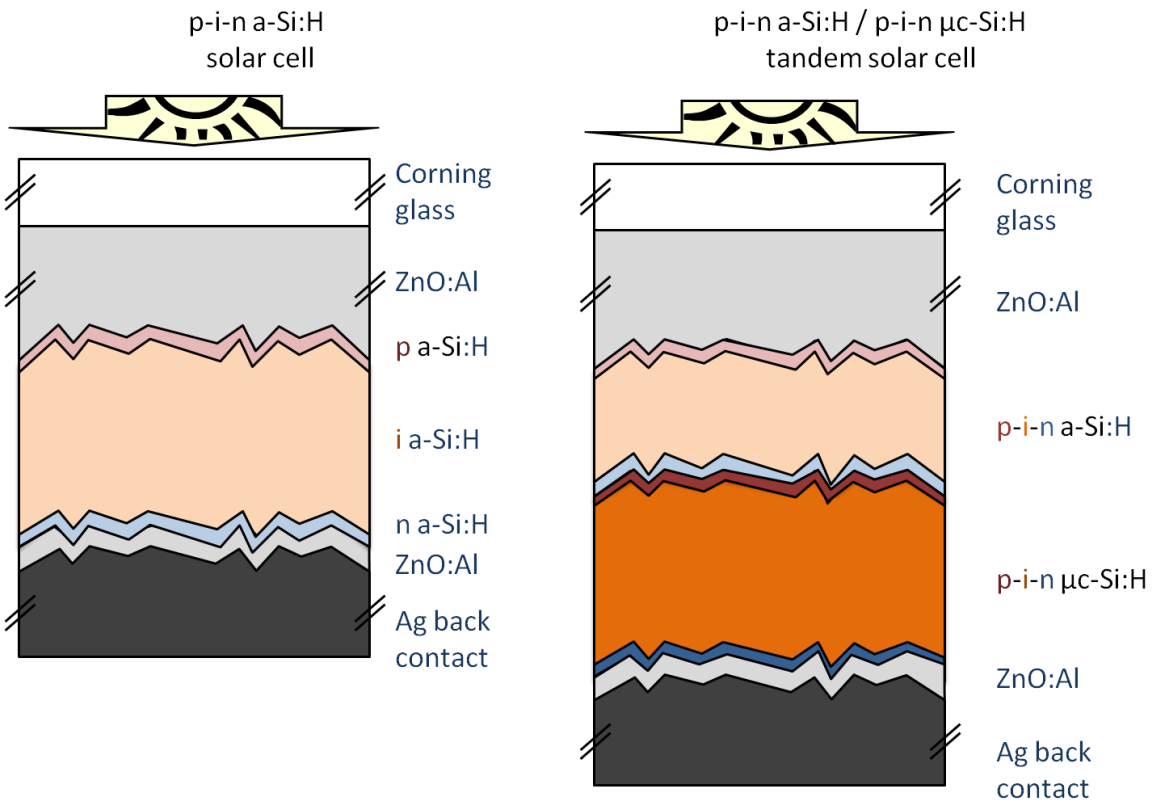

Figure 2.5: Schematics of the homojunction p-i-n a-Si:H solar cell design (left) and the heterojunction a-Si:H/µc-Si:H tandem solar cell design [5].

Depending on hydrogen content, a-Si:H has an approximated optical band gap of (1.6…1.8) eV [47]. Photons of the solar spectrum with lower energies (see Figure 2.4) are not absorbed in the absorber of this solar cell design. The optical band gap of µc-Si:H is closer to that of crystalline Si (1.1 eV) and thus smaller than for a-Si:H. Thus, by growing a microcrystalline silicon (µc-Si:H) p-i-n cell after the a-Si:H p-i-n stack, the photons below the gap of a-Si:H can be absorbed in the bottom cell of this tandem stack (shown in Figure 2.5).

The main function of the p-layer of the a-Si or µc-Si cell is to span the space charge region in the intrinsic layer that results in the separation of the photogenerated electron-hole pairs. Light absorption and photogeneration in the p-doped layer does not result in a charge separation and is therefore not beneficial for the performance of the solar cell. Recent studies

involve making this layer transparent by increasing its bandgap. This can be achieved by adding carbon or oxygen precursors during layer deposition. Non- stoichiometric SiC_x window p-layers thus have an increased band gap of 1.8-2.4 eV [48]. A related increase in solar cell performance was shown for using SiC_x [49] and SiO_x p-layers [50].

Solar cells based on hydrogenated a-Si:H suffer from degradation, also known as the Staebler-Wronski-Effekt [3]. Upon illumination, the defect density increases, resulting in increased recombination and a decrease of efficiency.

Solar cells based on µc-Si and polycrystalline silicon (poly-Si) do not suffer from this disadvantage [5]. Direct deposition of µc-Si:H is, however, usually slower than that of a-Si:H, therefore the whole n^+-p^--p structure is grown as an amorphous layer stack and then crystallized with SPC. Solar modules using a poly-Si n^+-p^--p design achieve efficiencies of up to 10.5 % [12]. These devices, however do not use a TCO front contact but instead use a rather complicated contact scheme that included etching grooves into the cell to contact the front [7][12].

Ultimately, the implementation of ZnO:Al as a front contact in poly-Si based solar cells is one major goal of the research efforts of the HZB. A respective schematic of the cell design can be seen in Figure 2.6.

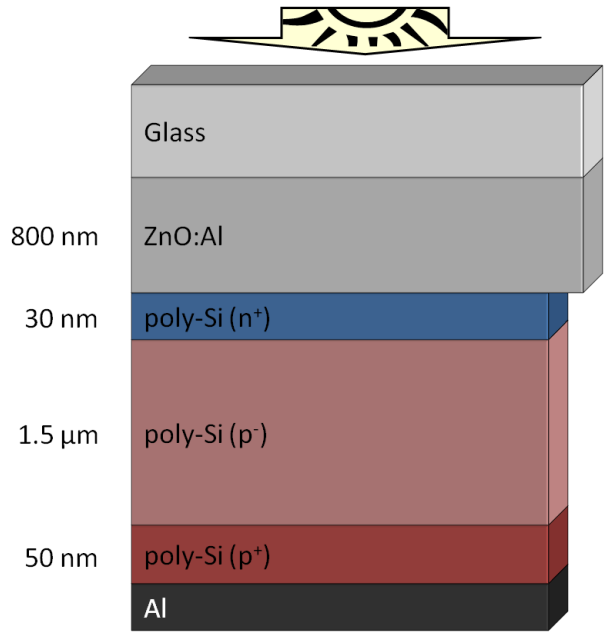

Figure 2.6: Schematic of a poly-Si n^+-p^--p solar cell design using a ZnO:Al TCO front contact.

After deposition of the n^+-p^--p a-Si:H layers with PECVD or e-beam evaporation, the layer stack is SPC annealed under N_2 atmosphere (typically 600 °C for 24 hours) in a glass furnace. After this SPC process, rapid thermal annealing (RTA) is performed by halogen lamp illumination in N_2 atmosphere up to 950 °C for several minutes to heal crystal defects [51][52]. After that, hydrogen passivation is performed by igniting a RF plasma in H_2 atmosphere to infuse atomic hydrogen into the poly-Si layer stack to passivate remaining defects (i.e. dangling bonds) [53]. Contacting is achieved by depositing aluminum on the back side and connecting the bare TCO front contact at the edge of the cell.

The implementation of the TCO front contact remains challenging. It was found recently that the SPC and RTA process of the glass/ZnO:Al/poly-Si layer stack result in an efficiency drop. This is shown in Figure 2.6 where the J-V curve of a cell using a 50 nm thick SiN_x diffusion barrier between the poly-Si and the ZnO:Al [54] is compared to the glass/ZnO:Al/poly-Si cell before and after RTA [19].

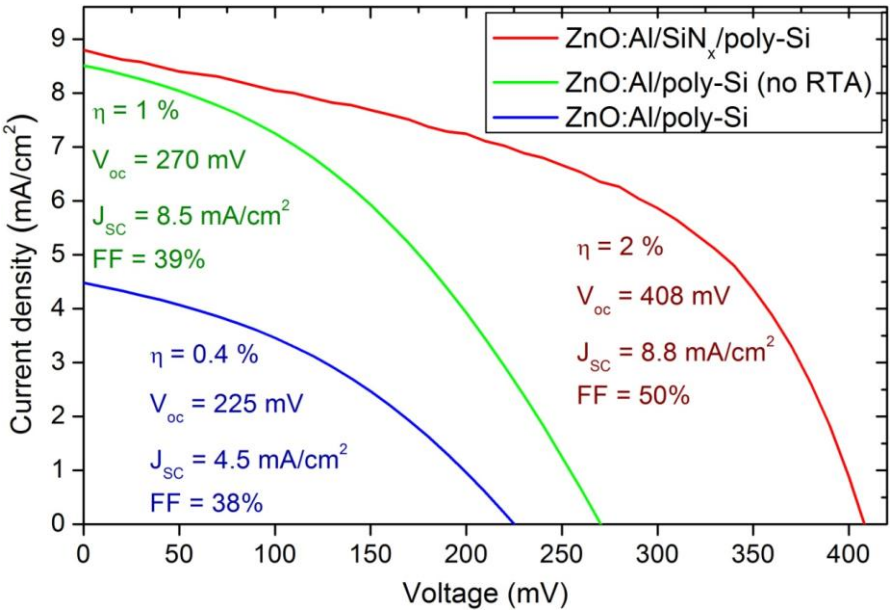

Figure 2.7: J-V curve of three n^+-p^--p poly-Si cells on ZnO:Al before hydrogen passivation. A 50 nm thick SiN_x layer was introduced between the poly-Si stack and the TCO (red line) for one cell, another one did not undergo RTA (green line) (after[19])

The lower efficiency of the solar cell on ZnO:Al before RTA compared to the one with the SiN_x diffusion layer (after RTA) suggests, that detrimental effects already occur upon SPC. Therefore one main pupose of this study is to reveal possible species interaction at the buried Si/ZnO:Al interface (see chapter 5). Before doing so, the applied experimental methods are used to investigate the SPC process (chapter 4), and after that (chapter 6) the electronic structure of a-Si:H(B)/ZnO:Al and µc-Si:H(B)/ZnO:Al is unraveled.

3. Characterization methods

This chapter introduces and briefly explains the methods and experimental setups that were used in this thesis. The employed methods were synchrotron based x-ray emission spectroscopy (XES), x-ray absorption spectroscopy (XAS), x-ray photoelectron emission microscopy (X-PEEM), x-ray photoelectron spectroscopy (XPS), hard x-ray photoelectron spectroscopy (HAXPES), Raman spectroscopy, scanning electron microscopy (SEM) and electron back scatter diffraction (EBSD).

Most of these methods use photon induced electron transitions from an initial $|\psi_i\rangle$ to a final state $|\psi_f\rangle$. The probability $P_{f;i}$ for such a photon stimulated electronic transition is generally expressed with Fermi's golden rule [55]:

$$P_{f;i} = \frac{1}{h} \left| \langle \psi_f | \, \hat{H} \, | \psi_i \rangle \right|^2 \, \delta(E_f - E_i - h\nu) \qquad \textbf{3.1}$$

with the Planck constant h, delta function $\delta(\ldots)$, energy of the final (initial) state E_f (E_i), the photon frequency ν and the perturbation operator $\hat{H}$. The perturbation operator can be expressed as [56]:

$$\hat{H} = \frac{e}{2m_e c} \left(\hat{A} \cdot \hat{p} + \hat{p} \cdot \hat{A} \right) + \frac{e^2}{2m_e c} \hat{A}^2 \qquad \textbf{3.2}$$

with the electron charge e, mass m_e, vacuum speed of light c, the vector potential operator $\hat{A}$ und the momentum operator $\hat{p}$.The last term including $\hat{A}^2$ can me neglected for moderate photon intensities [56]. $\hat{A}$ commutes with $\hat{p}$ if div $\hat{A} = 0$ which is the case for long wavelength in the dipole approximation [55]. With these approximations, equation 3.2 can be rewritten to:

$$\hat{H} = \frac{e}{m_e c} \left(\hat{A} \cdot \hat{p} \right) \qquad \textbf{3.3}$$

As the system consist of more than one electron, all states ψ can be approximated as a state consisting of M one-electron functions ϕ with $\psi_M = \phi_n \cdot \psi_{M-1}$ and the resulting energy consisting of an addition of the one-electron energies ϵ with $E_M = \epsilon_n + E_{M-1}$. In this context, and assuming the perturbation $\hat{H}$ only affects the nth initial one-electron function $\phi_{i,n}$, equation 3.1 can be rewritten to:

$$P_{f;i} = \frac{1}{h} \left| \langle \phi_{i,n} | \hat{H} | \phi_{i,n} \rangle \right|^2 \langle \psi_{f,M-1} | \psi_{i,M-1} \rangle \; \delta(\epsilon_{f,n} + E_{f,M-1} - E_{i,M} - h\nu) \qquad \textbf{3.4}$$

In a further approximation according to Koopmans theorem [55] or frozen-orbital approximation [57], one can assume that the initial and final states without the nth electron are equal: $\psi_{f,M-1} = \psi_{i,M-1} \rightarrow E_{f,M-1} = E_{i,M-1}$ equation 3.4 changes to:

$$P_{f;i} = \frac{1}{h} \left| \langle \phi_{i,n} | \hat{H} | \phi_{i,n} \rangle \right|^2 \delta(\epsilon_{f,n} - \epsilon_{i,n} - h\nu) \qquad \textbf{3.5}$$

The delta function results in a transition only if $\epsilon_{f,n} = \epsilon_{i,n} + h\nu$. For photoelectron spectroscopy, where the final state is a free electron with the kinetic energy E_{kin} plus the work function φ and the initial state as the negatives Hartree-Fock binding energy E_B this results in the relation:

$$E_{kin} = h\nu - E_B - \varphi \qquad \textbf{3.6}$$

which of course is only a rough estimate of the kinetic energy due to the mentioned assumptions (primarily the Koopmans theorem) but supports the approach of identifying photoemission lines with occupied one-electron states. Similar considerations are also possible for auger electron spectroscopy (AES), XAS and XES but more complicated due to different final states.

3.1 Synchrotron based x-ray sources

Synchrotrons are bright x-ray sources that allow a variety of experiments. Synchrotron facilities mainly consist of a storage ring in which charged particles cycle in vacuum with a constant speed close to the speed of light. The cyclic path is guided by bending magnets along the storage ring. Synchrotron radiation is generated as a side effect at these bending magnets and (for so called 3rd-generation facilities) in special insertion devices, which are placed in the straight sections of the storage ring. This radiation is guided through beamlines to the experimental endstation.

The particle beam is originally created in a linear accelerator, then shaped in axially space packs (bunches) and accelerated in a smaller booster ring before being injected into the storage ring. The acceleration and shaping is achieved with radio frequency in klystrons. A klystron in the storage ring constantly supplies the beam with energy to compensate energy losses due to bending magnets and insertion devices. The most relevant elements and the underlying principles of synchrotron based x-ray sources are explained in the following – mainly based on the text book by Attwood [58].

When charged particles are accelerated, they generally emit radiation. If a magnet forces the particle on a cyclic path, it is accelerated towards the center of this cycle – resulting in what is called synchrotron radiation. For synchrotron radiation, this particle has a velocity close to the speed of light. Therefore relativistic effects have to be taken into account. Here the Lorentz factor γ is of high relevance. It is defined with the velocity of the particle v and the speed of light in vacuum c to [58]:

$$\gamma \equiv \frac{1}{\sqrt{1 - \frac{v^2}{c^2}}} \qquad \textbf{3.7}$$

The trajectory of an electron passing a constant magnetic field and the resulting emission of synchrotron radiation is shown in Figure 3.1.

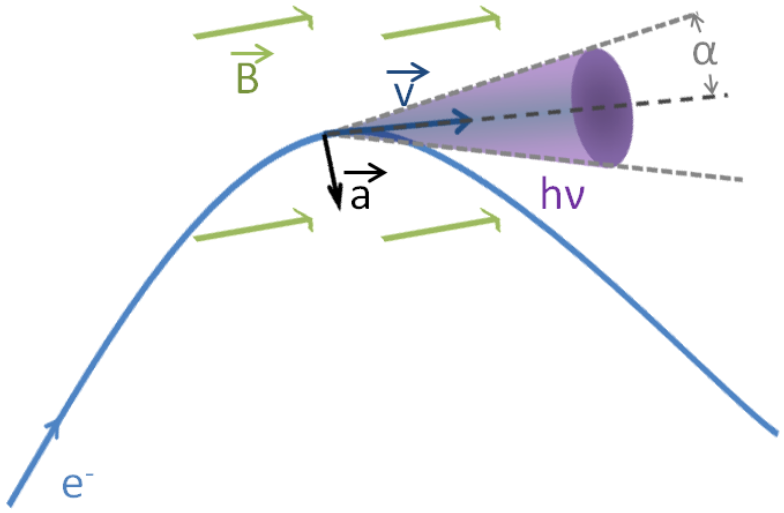

Figure 3.1: Scheme of an electron traveling through a constant magnetic field $\vec{B}$ with the relativistic velocity $\vec{v}$. The electron is accelerated towards a circle centre with the acceleration $\vec{a}$ and therefore emits synchrotron radiation in a radiation cone with an angle α (after [58]).

It can be shown, that the relativistic speed of the charged particle (usually an electron) causes synchrotron radiation to be emitted in a radiation cone tangential to its path in an angle $\alpha \cong \frac{1}{2\gamma}$ [58]. The radiation spectrum is very broad and could span over the whole electromagnetic spectrum. The energy spectra associated with bending magnets can be characterized by the critical photon energy E_c which is the energy at which half of the photon intensity is below and the other half is above. For a magnetic flux density B, the charge e, the mass m and the Planck constant h it can be expressed as [58]:

$$E_c = \frac{3ehB\gamma^2}{4\pi m} \qquad \textbf{3.8}$$

The root mean square of the photon energy spread ΔE can be further determined to [58]:

$$\Delta E \geq \frac{ehB\gamma^2}{\pi m} \qquad \textbf{3.9}$$

In the course of this research, synchrotron based measurements were done at three different sites. The Advanced Light Source (ALS) in Berkeley, the Berliner Elektronen Synchrotron (BESSY II) in Berlin and the Super Photon Ring – 8 GeV (SPring-8) in Hyōgo. Electrons in the storage rings have a specific ring energy E_r, which is 1.9 GeV (ALS), 1.7 GeV (BESSY II)

and 8 GeV (SPring-8). For highly relativistic particles Equation 3.8 can be rewritten with the energy of the electrons E_r when using $\gamma = \frac{E_r}{mc^2}$ and substituting the constants to [58]:

$$E_c\,[\mathrm{keV}] = 0.665\,E_r^2\,[GeV]\;\;B\,[T] \qquad \textbf{3.10}$$

Higher ring energies therefore result in a higher critical energy. If assuming a magnetic flux density B to be 1 T (which is roughly in the order of magnitude of values for synchrotron bending magnets [58]), the resulting critical energies E_c are 2.4 keV for ALS, 1.9 keV for BESSY II and 42.6 keV for SPring-8. Synchrotron radiation at ALS and BESSY II is therefore most intense in the soft x-ray and at Spring-8 in the hard x-ray regime.

Besides the above discussed bending magnets, synchrotron light can also be generated by insertion devices which are differentiated based on their magnetic field strength and dimensions into undulators and wigglers. A general scheme of an insertion device is shown in Figure 3.2.

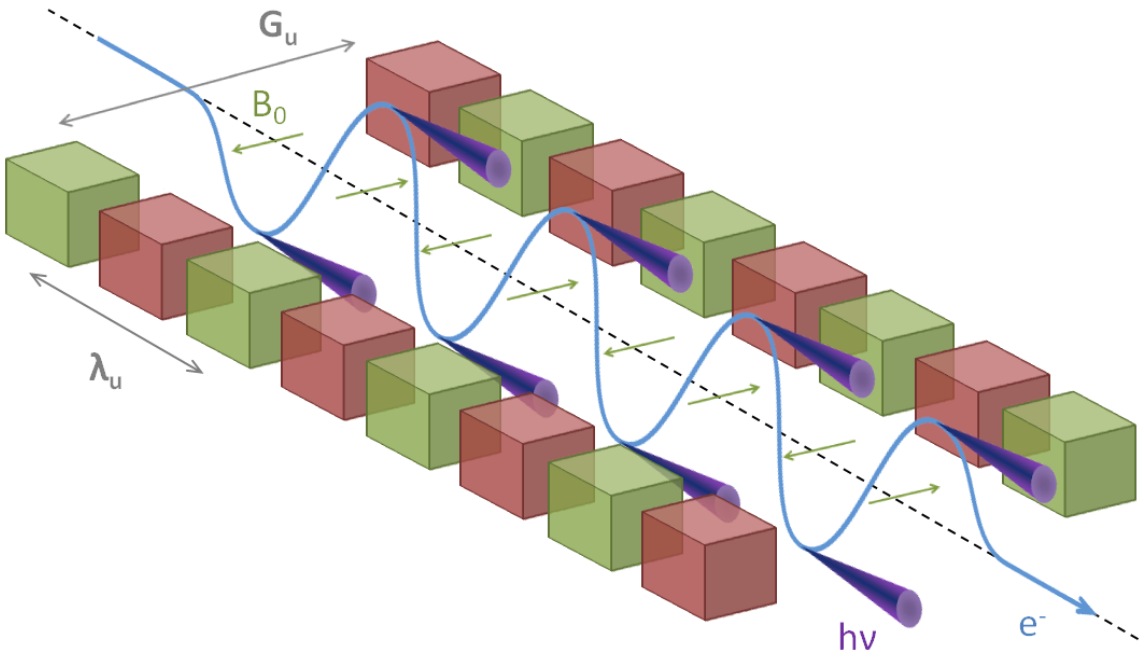

Figure 3.2: Schematic of an insertion device featuring alternating magnetic dipole pairs with the undulator frequency λ_u as the distance between equally poled magnets and the undulator gap G_u as the distance between the magnetic arrays. The path of the electronic beam (blue), synchrotron radiation cones (indigo) and the magnetic field density at center axis B_0 is indicated. Magnet dimensions, synchrotron radiation cone size and the electron path amplitude are off-scale (after [58]).

They consist of arrays of permanent magnet pairs that are stacked with alternating polarity; the spacing defines the undulator frequency λ_u. The electron beam travels through this array, being accelerated in the alternating magnetic field B_0, which results in an oscillating path along the central axis. As in Figure 3.1 synchrotron radiation is generated. Due to the magnet arrangement, some of the emission cones are aligned codirectional along the center axis.

These synchrotron emission cones can overlap and if certain conditions are met, constructive interference occurs, which results in a significant gain of intensity at specific photon energies.

An indicator for this is the non-dimensional magnetic strength K. It is defined as [58]:

$$K \equiv \frac{eB_0\lambda_u}{2\pi mc} = 0.9337\ B_0\ [T]\ \lambda_u[cm] \qquad \textbf{3.11}$$

If K is much larger than 1, the cyclotron radiation cones are spatially too far apart to overlap and cannot interfere. This is the case for the wiggler, which results in a similar “white light” emission as a bending magnet but typically at higher intensities.

For an undulator, where K is close to or smaller than one, the cones interfere, which gives a significant rise at the wavelength λ_n and its higher harmonics. The undulator equation describes this wavelength. For the nth harmonic it can be deduced to [58]:

$$\lambda_n = \frac{\lambda_u}{2n\gamma^2}\left(1+\frac{K^2}{2}+\alpha^2\gamma^2\right) \qquad \textbf{3.12}$$

The last term describes an angular dependence of the wavelength with α. Equation 3.12 can be expressed in energies as [58]:

$$E_n[keV] = \frac{0.9496\ n\ E_r^2\ [GeV]}{\lambda_u[cm]\left(1+\frac{K^2}{2}+\alpha^2\gamma^2\right)} \qquad \textbf{3.13}$$

To change the photon energy, the magnetic field density B_0 is usually varied by increasing or reducing the undulator gap (G_u in Figure 3.2).

After the bending magnet or insertion device, the synchrotron radiation is guided through a beamline to the experiment. The beamline usually consists of a monochromator that use

Bragg reflection at the crystal lattice for hard x-rays or diffraction at ruled gratings for soft x-rays to further monochromatize the radiation, of other optical elements to guide the beam and of ionization chambers or gold meshes to measure the intensity of the x-ray beam. The specific layouts of the beamlines will be discussed in the following subchapters.

3.2 Photoelectron (PES) and Auger electron spectroscopy (AES)

Most of the theoretical part of this section is a summary from textbooks by Briggs [59] and by Lüth [55]. For a more detailed view on PES and AES a study of these books is advised.

PES is based on the external photoelectric effect, where the material is irradiated with photons, and electrons are excited into the vacuum. As shown at the beginning of chapter 3 in eqution 3.6, the resulting kinetic energy of the excited electron E_{kin} directly relates to the energy of the photon hν over the binding energy of occupied states E_B and the work function $\varphi = E_{vac} - E_F$, which is the difference between Fermi level E_F and vacuum level E_{vac}.

This process is visualized for a semiconductor in Figure 3.3. In PES the sample is irradiated with monochromatic light and electrons are detected according to their kinetic energy in an electron analyzer. Since the kinetic energy is directly related to the binding energy of the materials core and valence levels, PES is chemically sensitive.

Electrons are usually detected by a concentric hemispherical analyzer (CHA) that uses a variable repellant voltage and the constant electric field between two concentric hemispheres to select electrons by kinetic energy and an electron multiplier to detect them. The detector and the sample are usually grounded and therefore share the same Fermi level. In this case, the term φ is determined by the work function difference of the sample and the detector. For the experiment, clean gold references are usually measured to determine the work function of the analyzer and kinetic energies are related to the Fermi energy.

Based on excitation energy PES can be differentiated into UPS (ultraviolet PES), XPS and HAXPES. PEEM or X-PEEM combines PES with electron optics to gain spatial resolution.

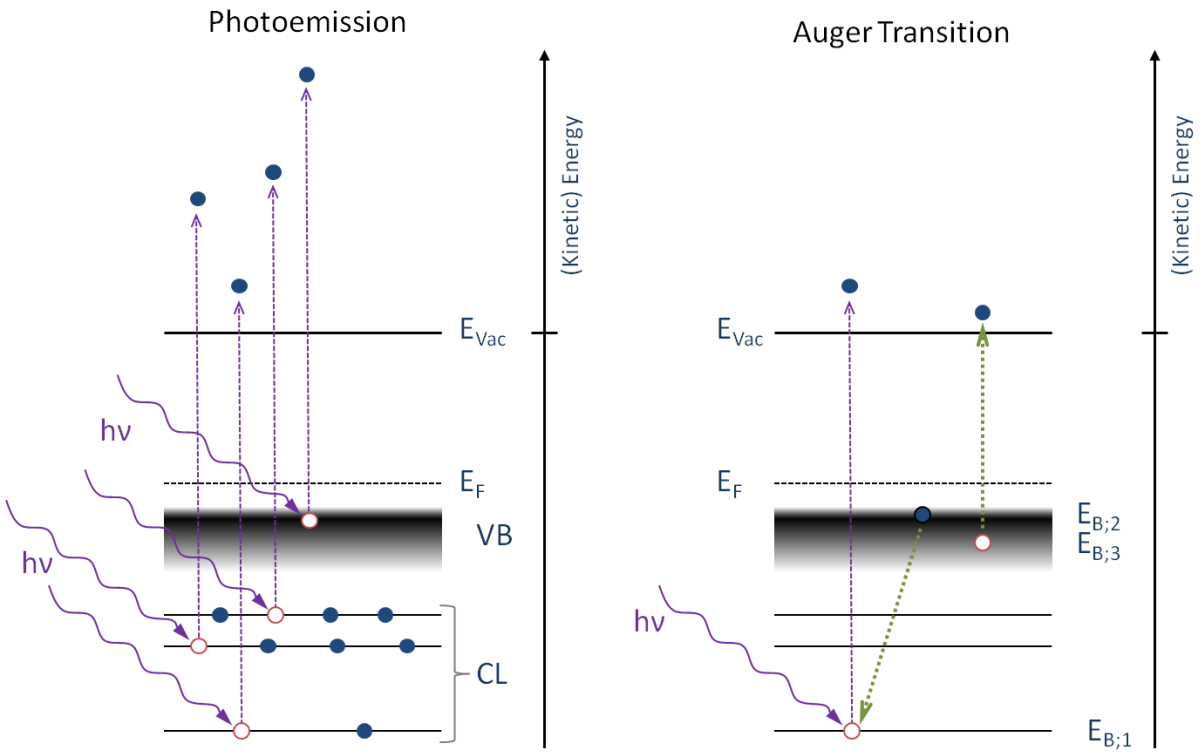

Figure 3.3: Left: Schematic of the photoelectric effect in a semiconductor where monochromatic photons (hν) excite electrons from core levels (CL) and valence band states above the vacuum level (E_{vac}). Right: Schematic of the electronic recombination of the CL hole resulting in an Auger transition (green dotted line).

The photo-generated hole can be filled with electrons from energy levels with lower binding energy through relaxation resulting in fluorescence (see XES in chapter 3.3) or Auger transitions. During the Auger transition, the energy that is gained by the relaxing electron ($E_{B;1}$ - $E_{B;2}$) is used to excite a third electron (the Auger electron at $E_{B;3}$) above the vacuum level. The kinetic energy of this Auger electron is independent of the excitation energy and only determined by the binding energy difference of the three involved electronic states. With a correction term $\Delta E_{2;3}$ that takes the binding energy shift due to holes into account [55], the kinetic energy of the Auger electron E_{kin}^{AGL} can be written as:

$$E_{kin}^{AGL} = E_{B;1} - E_{B;2} - E_{B;3} - \Delta E_{2;3} - \varphi \qquad \textbf{3.14}$$

Auger lines usually appear in XPS and HAXPES spectra which can be used to gain additional chemical information from the sample by calculating the Auger parameter α, which is commonly used to identify chemical compounds and has the advantage that it is independent of sample charging effects and band bending [60][61][62].

Due to the use of different photon sources in this thesis, the modified Auger parameter α^* is more relevant because of excitation energy independence [63]. From the kinetic energy of a specific Auger line (E_{kin}^{AGL}), the kinetic energy (E_{kin}^{PEL}) and the binding energy of a specific photoelectron line (E_B^{PEL}) it is calculated using:

$$\alpha^* = \alpha + h\nu = E_{kin}^{AGL} - E_{kin}^{PEL} + h\nu = E_{kin}^{AGL} + E_B^{PEL} \quad \textbf{3.15}$$

The information depth (ID) of PES and AES is governed by the inelastic mean free path (IMFP) of the photoelectrons or Auger electrons which describes the distance it takes for the electron signal with an initial intensity I_0 to travel and get attenuated by the factor of 1/e through inelastic scattering. The remaining intensity from the emission depth d together with the emission angle θ relative to the surface normal is given as:

$$I(d) = I_0 \, e^{\frac{-d}{IMFP * \cos\theta}} \quad \textbf{3.16}$$

The ID is defined as $3 \times IMFP$ in this thesis, resulting in an intensity loss of 95% (assuming normal emission; θ = 0) according to equation 3.16. The IMFP is dependent on the material and the energy of the electron, which is illustrated in Figure 3.4 for the materials and energy ranges relevant in this thesis. The values for a-Si were estimated assuming that a-Si has 5% less density than c-Si [64].

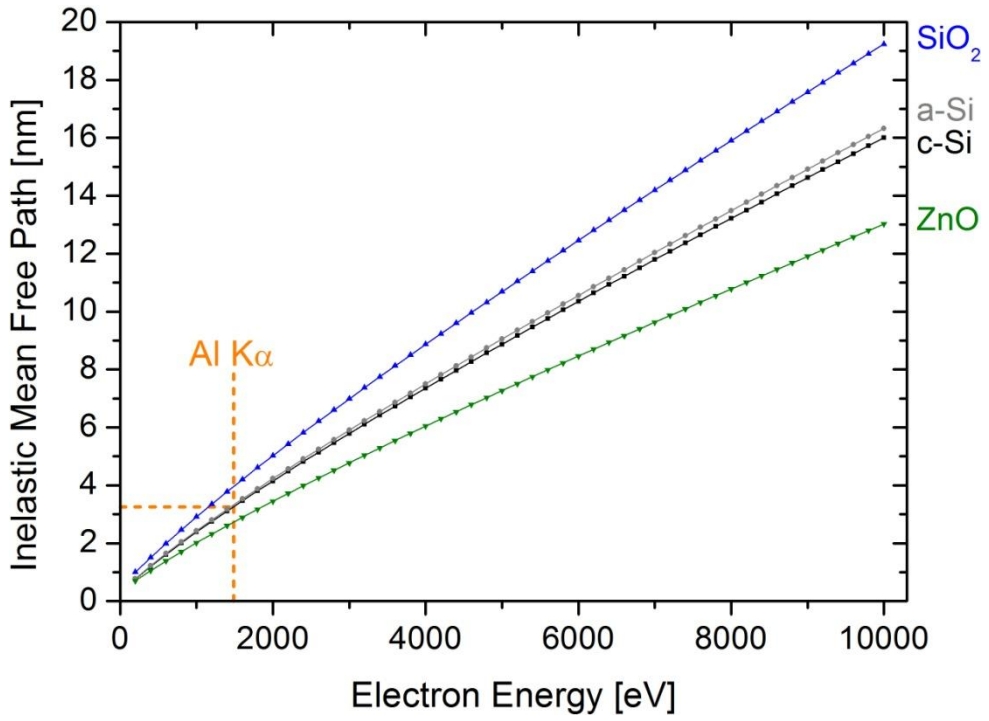

Figure 3.4: IMFP dependence for kinetic energies and materials relevant for this thesis (data points taken from [65] after [66]). For comparison the values for Al Kα excitation are indicated.

According to equation 3.6 the maximum electron energy is limited by the excitation energy. The maximal information depth of a typical lab-based XPS with an aluminum source ($h\nu_{Al\ K\alpha}$ = 1486.58 eV) can therefore be estimated to 10 nm in silicon. Higher information depths are possible with HAXPES due to higher excitation energies. If using hν = 6 keV excitation, the maximal information depth in Si can be increased to up to 31 nm [65].

Due to the much higher attenuation length of the exciting photons, compared to the IMFP of emitted photoelectrons, the attenuation of the photons can be neglected when estimating the information depth of PES.

3.2.1 HAXPES at BESSY II and Spring-8

The HAXPES measurements in this thesis were performed at the SPring-8 (beamline BL15XU [67]) and BESSY II (beamline KMC-1 [68], HIKE endstation [69][70]) synchrotron light sources.

KMC-1 uses a bending magnet and a water cooled double-crystal monochromator (DCM) to generate x-rays. Bragg reflection in the DCM's crystal pair monochromatizes the "white light" produced by the bending magnets. As the Bragg condition [71] is also fulfilled for multiples of the fundamental energy, higher harmonics are also generated and used.

By changing the crystal's tilt, the photon energy leaving the monochromator can be varied from 2-12 keV. Different crystal pairs [Si (111), Si (311) and Si (422)] are positioned on linear translation stages so that they can be changed in situ. In this thesis Si (111) and Si (311) crystals were used.

The energy resolution of the resulting beam and its flux varies with photon energy, harmonic order and crystal pair. This is shown in Figure 3.5 where the resolution was determined by measuring the experimental broadening of Au 4f photoemission lines. The light intensity is measured in an ionization chamber upstream of the HIKE endstation. The crystal is selected based on required resolution and photon flux.

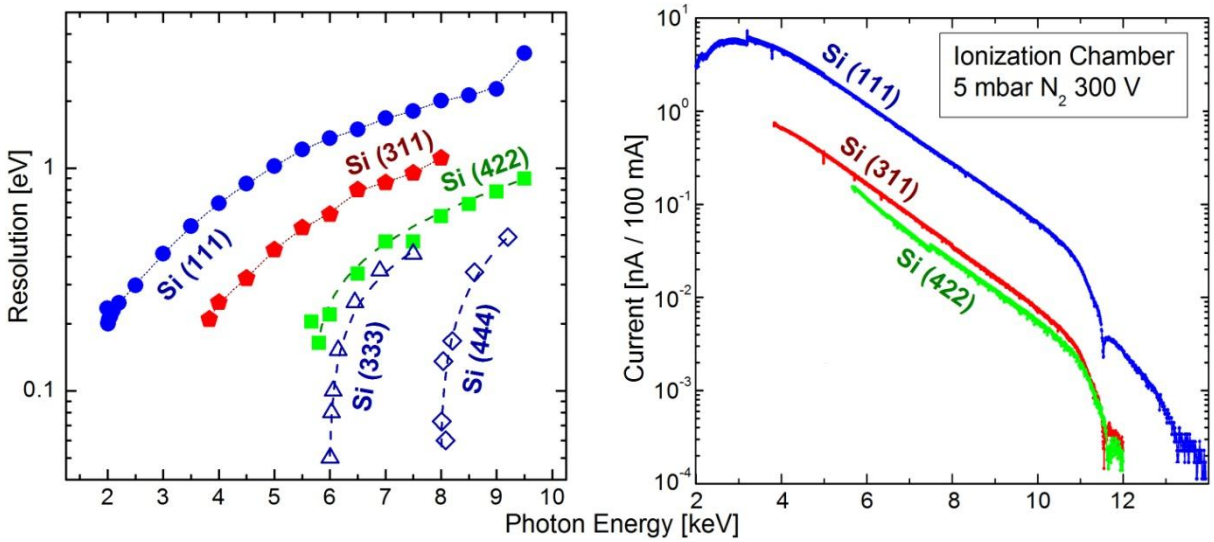

Figure 3.5: Left: Energy resolution of the KMC-1 beamline photons using the Si (111) in first, third [Si(333)] and fourth [Si(444)] order compared the Si (311) and Si (422) crystal Right: Intensity of the light measured as ionization current in an ionization chamber for all three crystals (from [69] and [72])

A toroidal mirror between the bending magnet and the DCM is used to focus the beam into the HIKE endstation. An x-ray capillary at the end of the beamline additionally focuses the beam into the experimental chamber and onto the sample.

The HIKE endstation is illustrated in Figure 3.6. Because of the grazing photon incidence, the SCIENTA R4000 concentrically hemispherical analyzer (CHA) is positioned almost normal ($\theta \approx 90°$) to the sample surface – resulting in maximal information depth according to equation 3.16. The energy scales were calibrated using Au 4f and Au Fermi edge reference measurements.

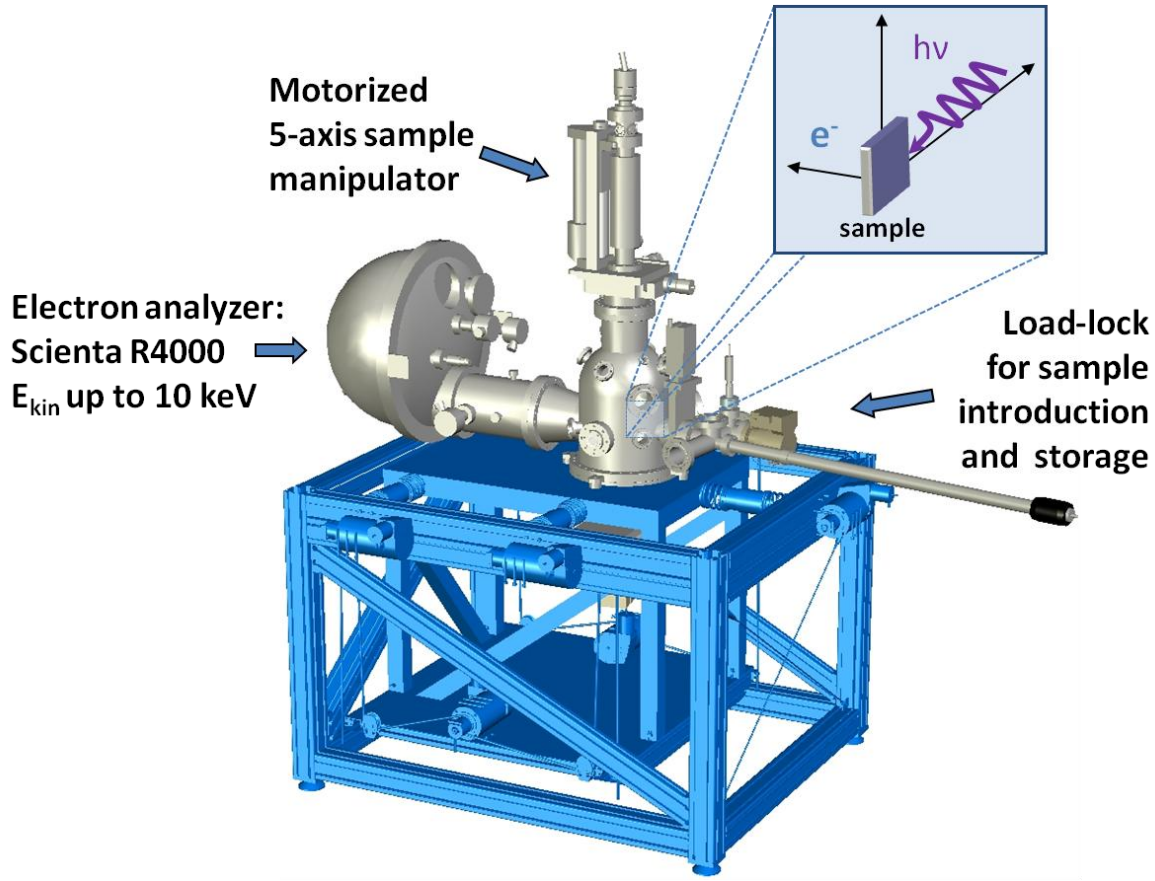

Figure 3.6: Schematic of the HIKE endstation. Magnified is the sample orientation. The direction of the hard x-ray illumination and the detected photoelectrons are indicated. (Images provided by Mihaela Gorgoi [72])

The BL15XU beamline at SPring-8 uses a helical undulator and a double-crystal monochromator (DCM) to produce intense x-rays in the range of ca. 2-36 keV. Due to the use of an undulator instead of a bending magnet and the higher storage ring electron energy of the synchrotron (SPring-8: 8 GeV; BESSY II: 1.7 GeV), higher photon intensities and energies are possible. The DCM is cooled with liquid nitrogen and can be used with a pair of Si (111) or Si (311) crystals. After the DCM, a channel cut monochromator to further increase

resolution [with Si (111), Si (200) and Si (311) crystals], total reflection mirrors and a toroidal focusing mirror is positioned [67] to adjust and focus the beam into the experimental chamber. The monochromator crystals are not interchangeable in-situ resulting in a down time when changing photon energy ranges.

The endstation uses the same type of electron analyzer as HIKE (VG SCIENTA R4000). Electrons are also detected at normal incidence. Spectra are calibrated the same way – i.e. with PES lines of a gold reference.

Due to the higher flux at BL15XU compared to KMC-1 (compare [67] and [68]), the count rate of photoemission electrons is higher and therefore the measurement time can be reduced significantly, which is essential especially for valence band measurements because the photoemission cross section decreases drastically with increasing excitation energy in the hard x-ray regime [73].

3.2.2 X-PEEM at BESSY II

X-PEEM measurements were performed at the SPEEM endstation of the BESSY II UE49-PGMa APPLE-II undulator microfocus beamline [74] which uses a commercial Elmitech PEEM II system. A schematic of this endstation is shown in Figure 3.7.

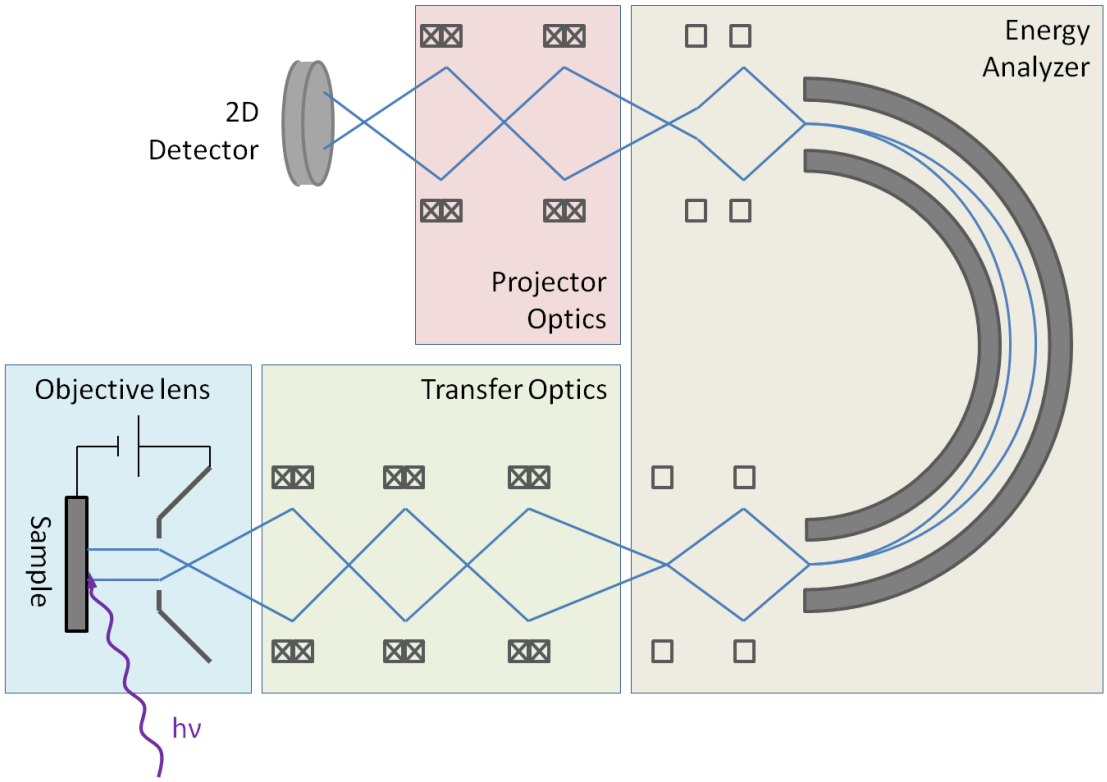

Figure 3.7: Schematic of the SPEEM setup (omitting the elements to gain spin resolution – edited from [74]). The electronic path is drawn in blue and squares indicate electronic lenses.

Soft x-ray excitation (100-1800 eV) is used for photoemission. The photoelectrons from the sample are first accelerated towards the entrance cone of the instrument, which is typically at + 10…20 kV potential relative to the sample. This objective lens passes the electrons into the transfer optics which delivers them into the hemispheric energy analyzer. After this, the projector optics magnify the electrons onto the 2D detector [74].

Using this setup, spatially resolved XPS or XAS spectra can be recorded: By keeping the excitation energy constant and changing the kinetic energy with the analyzer ("analyzer scan") [→ XPS] or by changing the excitation energy with the monochromator and keeping the analyzer at a fixed kinetic energy ("monochromator scan") [→ XAS]. The analyzer scan has the advantages that it is fast but the disadvantage that the focal points of the electron optics change with kinetic energy – resulting in a loss of spatial resolution, loss of focus and image defects if the change in kinetic energy is too high. The monochromator scan is slower due to the necessary change of monochromator and undulator but due to the constant kinetic energy, the electron optics transmission stays the same.

3.3 X-ray emission (XES) and absorption spectroscopy (XAS)

X-ray emission (sometime called x-ray fluorescence) is the competing process to the Auger transition. A core hole is generated through photoemission in the energetic level $E_{B;1}$ and a relaxing electron from $E_{B;2}$ fills the hole. The difference in binding energy is used to emit a photon with the energy $h\nu_{em}$ (as shown in Figure 3.8). In x-ray emission spectroscopy, the emitted photons are detected by an x-ray spectrometer to investigate the density of occupied states above $E_{B;1}$. For low atomic numbers, the Auger transition probability (p_{LMM}) is much higher than the probability for x-ray emission ($p_{Si,L_{2,3}}$) – i.e., Si: $p_{Si,LMM} > 99.9\%$, $p_{Si,L_{2,3}} < 0.1\%$ [59][75]. Therefore high light intensities – as found at a synchrotron – are required to generate enough fluorescence.

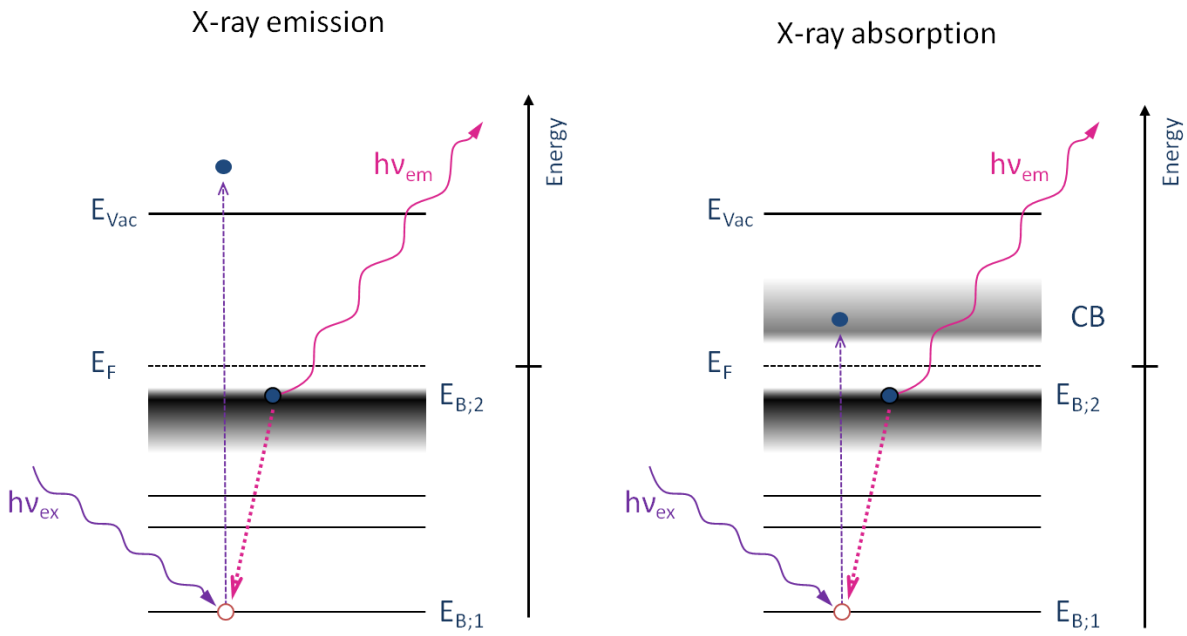

Figure 3.8: Left: Schematic of x-ray emission, where photons $h\nu_{ex}$ excite an electron from $E_{B;1}$ above the vacuum level. A second electron from $E_{B;2}$ relaxes into this core hole and emits a photon $h\nu_{em}$. Right: In x-ray absorption the electrons are excited into unoccupied states of the conduction band (CB), resulting in secondary processes of which the fluorescence decay is depicted.

In x-ray absorption (XAS), the excitation energy is varied to excite the core electron into unoccupied states (i.e. the conduction band in Figure 3.8). The absorption can be detected indirectly e.g. over secondary processes by measuring the emitted fluorescence photon, that is produced when the core hole is filled (fluorescence yield) or by monitoring the sample current

(electron yield). Electrons leaving the sample due to PES and AES have to be replaced, resulting in a current flowing into the sample. If using a dispersive element in front of the detector, the detection method can be differentiated into partial florescent yield.

The density of unoccupied states can therefore be investigated with XAS. If only the energy range close to the absorption onset (conduction band minimum) is investigated, XAS is also called near edge absorption fine structure (NEXAFS). Throughout this thesis the term XAS is used instead of NEXAFS.

XAS is complementary to XES and both techniques in combination can be used to determine band gaps by detecting the emitted photons with the highest energy, which corresponds to the valence band edge in XES and the minimal excitation energy that is required to excite electrons from the core level into the conduction band in XAS. But the presence of core excitons has to be taken into account, when interpreting this "band gap energy". Si 2p core excitons are critical for Si $L_{2,3}$ XAS spectra of amorphous silicon [76] and crystalline silicon [77] as they appear right at the absorption onset, which decreases the measured band gap significantly. The binding energy of the exciton in crystalline Si was determined to 0.2 eV [77].

As XES and XAS (for fluorescence yield) are photon-in/photon-out methods, the information depth is determined by the absorption cross section in the material and analogous to the IMFP for XPS in equation 3.16 an attenuation lengths λ_a can be defined [78]. But since the energy and thus the attenuation length of the exciting and emitted photons are different, they have to be combined into the effective attenuation length λ_a^* with following equation [79]:

$$\lambda_a^* = \frac{\lambda_a^{ex} \times \sin\alpha \times \lambda_a^{em} \times \sin\beta}{\lambda_a^{ex} \times \sin\alpha + \lambda_a^{em} \times \sin\beta} \qquad \textbf{3.17}$$

where λ_a^{ex} (λ_a^{em}) is the excitation (emission) attenuation length and α (β) the angle between the sample and of the exciting (emitted) photons. Following the definition from chapter 3.2, the information depth is therefore given as $3\times\lambda_a^*$. Values for the λ_a can be found in [80].

The effective attenuation length for the Si $L_{2,3}$ emission can be estimated to be 29 nm in silicon (resulting in an information depth of 87 nm) using an excitation (emission) energy of 145 eV (92 eV) and 45° incidence.

In this study, only partial fluorescence yield XAS is used due to the higher information depth similar to XES. The information depth of electron yield XAS is limited by the IMFP of the emitted electrons.

3.3.1 XES and XAS at the ALS

XES and XAS measurements were performed at the ALS beamline 8.0.1 which uses a U5.0 undulator with 89 magnetic poles and a period of λ_u = 5.0 cm. By changing the undulator gap, the first, third and fifth harmonic can be used to generate soft x-ray photons from 65...1409 eV [81][82]. A schematic of the beamline is shown in Figure 3.9.

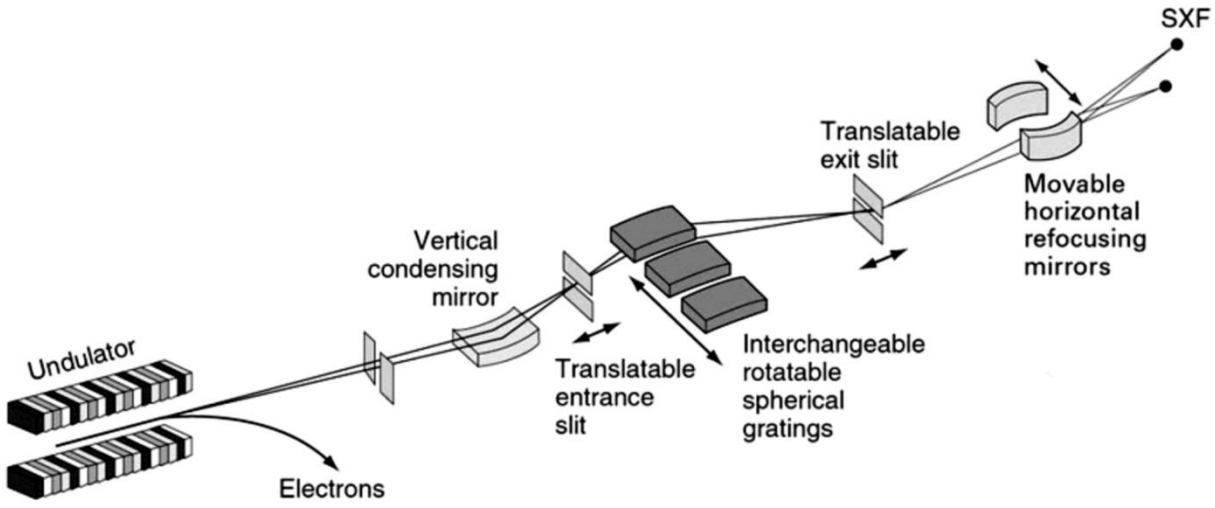

Figure 3.9: Schematic of beamline 8.0.1 at ALS taken from [82]. The main optical and dispersive elements are indicated.

After passing a focusing mirror, the photons are monochromatized by a spherical grating monochromator (SGM). The spherical grating can be changed from 150, to 380 or 925 lines/mm to allow operation in the energy range from 80 to 1400 eV. To adjust the resolution, the entrance and exit slits width can be manually adjusted. The exit slit is positioned on a moving stage to fulfill the Rowland circle configuration with the grating and the entrance slit [81][82]. A horizontal refocusing mirror is used to focus the beam into the soft x-ray

fluorescence (SXF) endstation and onto the sample resulting in a typical (for the here used slit settings) spot size of approximately 2 × 0.1 mm².

A schematic of the SXF endstation can be seen in Figure 3.10.

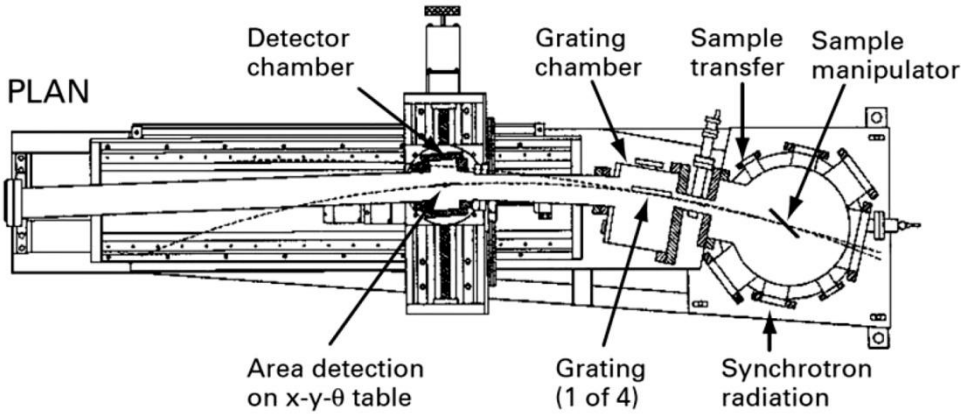

Figure 3.10: Schematic of the SXF endstation at ALS beamline 8.0.1 reproduced from [81][83].

The SXF endstation consists of a UHV chamber with an attached Rowland circle SGM, which forms the x-ray spectrometer. Synchrotron radiation illuminates the sample that is positioned on a 4-axis manipulator. Emitted photons pass a fixed entrance slit (50-100 µm width) into the spectrometer which consists of 4 interchangeable gratings (to access a range from 40 to 1000 eV) and a 2D detector that is mounted onto a movable stage [83]. By using the 2D channel plate detector, a spectrum can be recorded in "one shot" without changing monochromator parameters. The x-axis resembles the energy scale. By tilting the channel plate, the measurement window can be increased.

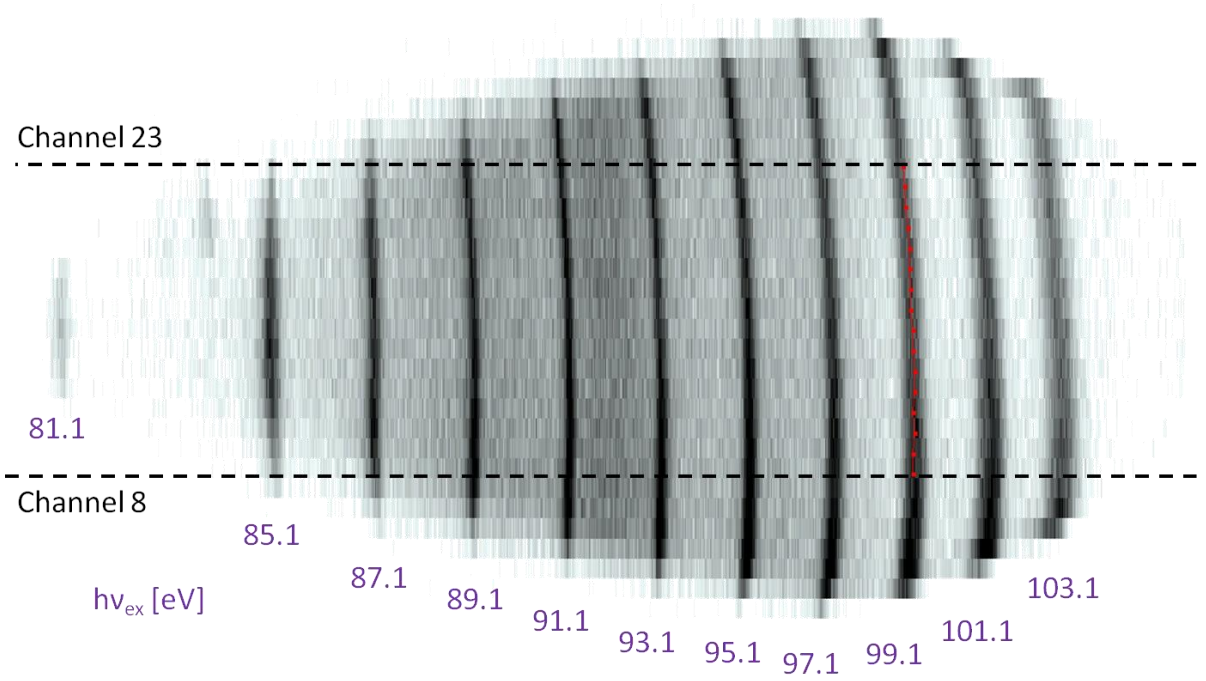

Figure 3.11: Raw data from the SXF 2D channelplate detector at an angle of 10° and a central wavelength of 88 eV. The curved lines represent elastically scattered Rayleigh lines for excitation energies between 81.1 and 103.1 eV. An oxidized Si wafer is used as the sample.

Figure 3.11 shows the raw channel plate image of the measuring range that is used for most XES spectra in this thesis. It also visualizes the calibration method used for all spectra. The SGM is set at 88 eV and the detector is tilted by 10°. While counting photons, the excitation energy is changed from 81.1 to 103.1 eV. The photons are elastically scattered on the sample surface and appear as curved lines (Rayleigh lines) on the detector. The oval shape of the image results from clipping of the spectra by UHV flanges, which becomes a problem when the detector is tilted to higher angles (and the energy window becomes larger). Lines are curved due to the spherical grating.

This raw data is processed into a two-dimensional ASCII file by adding up the intensity along these curved lines and scaling the x-axis according to the excitation energy. The numbers of usable channels which can be integrated have to be reduced due to the narrow shape at lower energies (towards the left of the image). Figure 3.11 indicates the used channels (8-23) and the curvature function that is applied to integrate intensities of the same energy (red line). For energies below 86 eV, only the central channels contribute reliable signal, intensities below 86 eV are therefore not quantified throughout the thesis. A customized version of the endstation control software (ALS sxedaq [84]) was used to process and calibrate the data raw.

Partial fluorescence yield XAS spectra are recorded with the same spectrometer settings. The spectra usually started at 99 eV excitation energy to measure the background before the conduction band onset. In order to prevent the elastic scattered peak to show up as an artifact in this background, the channel plate was gated at 98 eV, preventing photons with higher energy from being measured. XAS spectra and the beamline monochromator were calibrated with distinctive absorption features found in SiO_2 references at 105.5 eV (A), 106 eV (B) and 108 eV (C) [85], as shown in Figure 3.12.

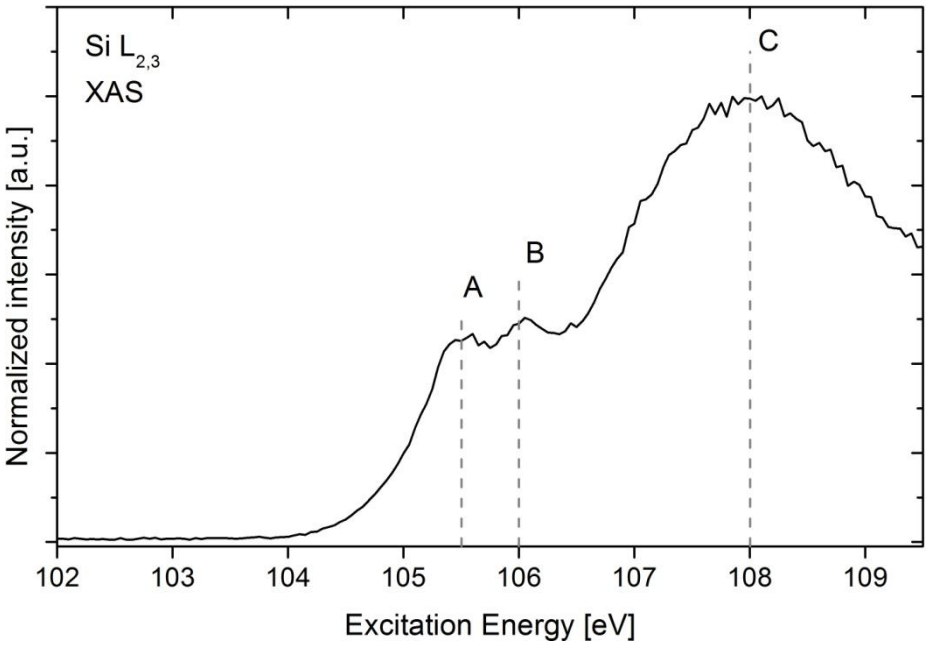

Figure 3.12: Si $L_{2,3}$ XAS spectrum of a SiO_2 reference. Indicated are the three features that were used for calibration.

3.4 Raman spectroscopy

In Raman spectroscopy the energy loss or gain of photon energy due to inelastic scattering is measured. The material is illuminated with monochromatic light and the energy shift due to the creation of a phonon (Stokes lines) or the annihilation of a phonon (anti-Stokes line) is detected [86].

Raman loss spectroscopy in the frequency range of 400...600 cm^{-1} is commonly used to evaluate the crystallinity of thin film silicon [26][87][88]. Note that crystalline grain size [89][90][91] and film stress [92] do influence the respective Raman spectra also.

Raman spectra were measured with a DILOR/ISA LabRAM 010 spectrometer and an unpolarized 632.8 nm HeNe laser.

For more details on Raman spectroscopy, refer to references cited above and the respective chapter in the text book by Abou-Ras [93].

3.5 Electron backscatter diffraction

Electron backscatter diffraction (EBSD) is a method to determine the specially-resolved crystallographic orientation. Using an electron gun, coherent electrons are sent to the specimen, where they are inelastically scattered back and analyzed with a 2D detector. If the probed sample volume is oriented in a crystallographic structure the image of the detector shows characteristic lines that form a pattern – the Kikuchi pattern [94] – resulting from backscattered electrons that fulfill the Bragg condition in the sample lattice. This pattern can be used to determine the crystal orientation. By scanning the electron beam over a sample surface, a spatial resolved determination of crystal orientation is possible, which is very useful for polycrystalline samples. EBSD is a complementary method to scanning electron microscopy (SEM) [95].

For EBSD a LEO GEMINI 1530 scanning electron microscope equipped with a NordlysII-S EBSD detector from Oxford Instruments HKL and a Thermo Fisher Scientific X-ray silicon drift detector was used.

For more details on EBSD, publications on other materials relevant to thin film solar cells by Abou-Ras might be studied [93][96][97].

4. SPC conversion of a-Si into poly-Si

In this chapter the solid phase crystallization (SPC) of thin a-Si:H films is examined. Main parameters that influence SPC are the deposition temperature, used dopants and substrates. It is revealed that the e-beam deposition temperature impacts the resulting grain size and crystallinity after SPC. Crystallization times for phosphorous doped Si are slower and for boron doped Si faster than for undoped Si layers. Finally the crystallization on ZnO:Al is found to be faster than on SiN_x.

4.1 Impact of grain size and grain boundaries

This subchapter focuses on describing and explaining observed changes in Si $L_{2,3}$ XES spectra of polycrystalline and microcrystalline Si thin film samples. Key questions are what the differences between amorphous, monocrystalline and poly- and µc-Si spectra are and how grain sizes and grain boundaries impact the spectral shape. In this context XES spectra are also compared to other characterization methods like electron back scatter diffraction (EBSD) and Raman spectroscopy.

The most common approach of evaluating the degree of crystallinity is Raman spectroscopy. Particularly its quantification is however based on simplifications and assumptions (i.e., no mechanical stress [98] as mentioned in 3.4). As a result, the Raman-derived degree of crystallinity can only be considered to be an estimation.

Although Si $L_{2,3}$ XES probes the electronic instead of the phonon band structure it will be shown that Si $L_{2,3}$ XES spectra can also be used to derive the amorphous/crystalline composition of Si thin films, which is a new and possibly more reliable approach to study the degree of crystallinity.

Si thin film samples were supplied by Christiane Becker, HZB. It was previously [26] observed that the crystallite orientation and size varies depending on the substrate temperature T_{dep} during e-beam deposition. Silicon films deposited at T_{dep} < 400 °C were amorphous and resulted in µm-sized grains upon SPC to form poly-Si. Films deposited at T_{dep} > 400 °C were already microcrystalline and SPC treatment did not impact the µc-Si samples significantly (i.e. led not to further crystal growth). Due to the observed wide variation in grain size, a similar sample series (directly on glass substrates without ZnO:Al in [26]) was used for the investigation of the influence of grain size on Si $L_{2,3}$ XES spectra.

Using e-beam evaporation 1.1 µm thick a-Si layers were deposited on Corning1737/Eagle2000TM glass substrates at a base pressure of $1 \cdot 10^{-7}$ mbar and 5 nm/s deposition rate. For different depositions the substrate temperature T_{dep} was varied between 200 °C to 600 °C. By co-evaporating boron from an effusion cell p^+ doping with a concentration of of $2 \cdot 10^{16}$ cm^{-3} [26] was achieved. One sample of each deposition was kept untreated while the other underwent SPC. In contrast to the SPC conditions in Ref. [26] (15 h 600 °C), 24 h 650 °C was used to guarantee a completed crystallization process.

For EBSD two SPC treated samples (T_{dep}: 300 °C and 500 °C) were selected. To remove the surface oxide, they were first ion milled (with Ar-Ions, ~10 min. at 5 kV, 2 mA and 2 min. at 3 kV, 1.2 mA) and then covered with a thin (4-5 nm), conductive graphite layer to avoid image drift due to charging.

The Si $L_{2,3}$ XES spectra recorded for the samples before and after SPC, together with those of a c-Si monocrystalline wafer and a a-Si reference, are shown in Figure 4.1.

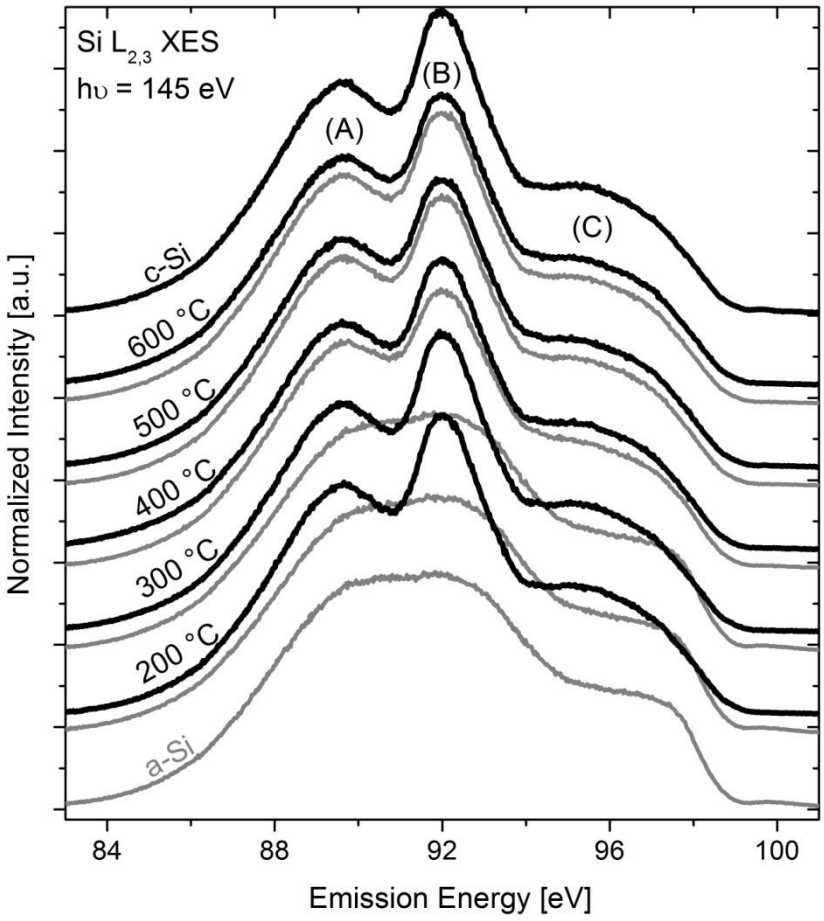

Figure 4.1: Area normalized Si $L_{2,3}$ XES spectra of a-Si:H (p^+)/glass samples, prepared using varying deposition temperatures before (gray) and after SPC (black) compared to an amorphous and crystalline Si wafer reference (bottom- and top-most spectra). Deposition temperatures are given next to the spectra.

All spectra show distinctive features for silicon which are a low-energy shoulder at 89.7 eV (A), a main peak at 92 eV (B) and a higher energy shoulder at 97 eV (C). For the as-deposited samples that are deposited at low temperatures and the a-Si reference these features are broader, while for deposition temperatures above 400 °C, all the SPC treated samples, and the Si wafer reference they are narrower and more pronounced.

According to Rubensson et al., [99] these spectral contributions can be generally attributed to electrons decaying from Si 3s derived states (A), hybridized s-p derived states (B), and 3p derived states (C) into generated Si 2p core holes. The as-deposited samples show a distinct transition from amorphous silicon to crystalline silicon with increasing deposition temperature. The Si $L_{2,3}$ XES spectra of the amorphous and monocrystalline Si references are similar to those reported in previous studies [100][101].

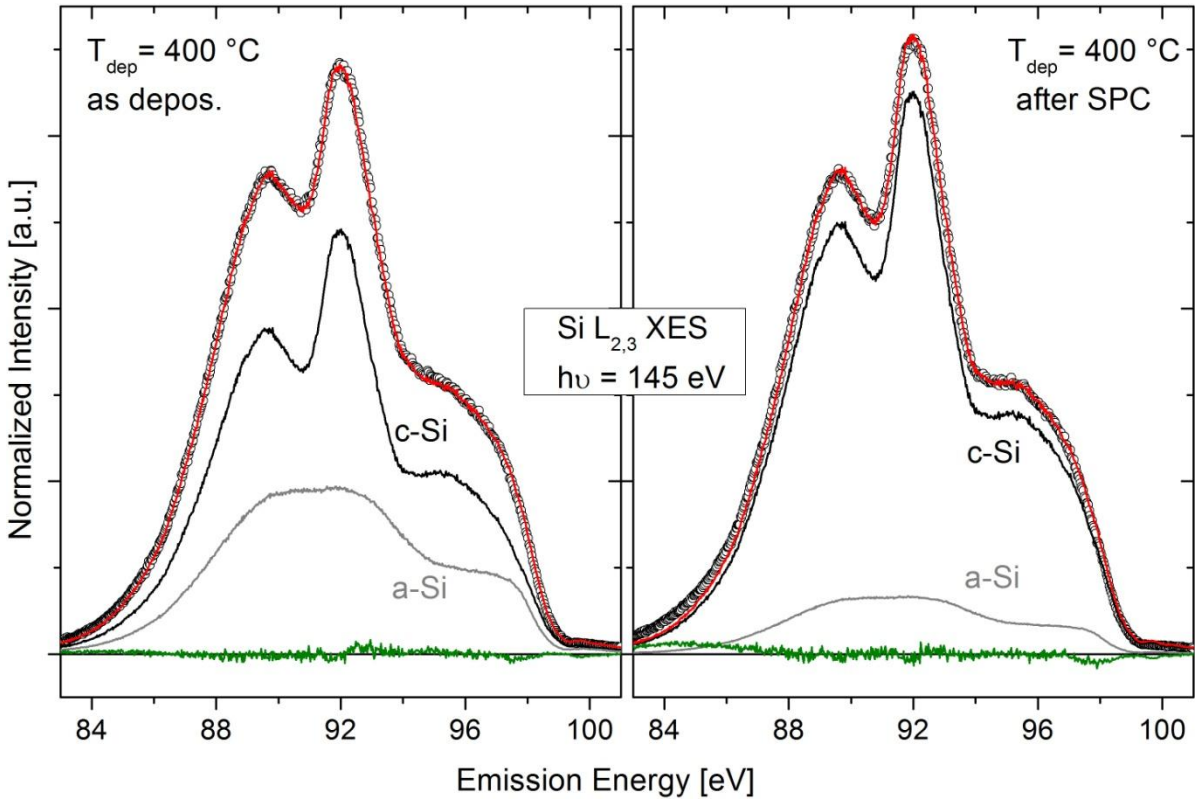

Figure 4.2: Si $L_{2,3}$ XES spectra of the T_{dep} = 400 °C sample before (left) and after SPC (right). Reference spectra of a-Si (gray) and c-Si (black) are scaled according to their respective contribution determined by the least-squares fit. The superposition (red), the measurement (○) and residuum (green) are also shown.

Each of the measured spectra can be well-represented by a superposition of a-Si and Si-wafer (c-Si) reference spectra (with the intensity I given as $I_{sample} = A \cdot I_{a\text{-}Si} + B \cdot I_{c\text{-}Si}$). Note that adding a SiO_2 reference in the superposition did not result in a better fit or a change of the coefficients A and B. Least-square fits were done with IGOR Pro [102] - examples can be seen in Figure 4.2 for the samples deposited at T_{dep} = 400 °C before and after SPC.

The fit describes the measurements well. Due to the area normalization of all Si $L_{2,3}$ XES spectra A (B) can directly be ascribed to the percentage of the respective amorphous (crystalline) spectral contribution. For the example spectrum of the as-deposited sample, an amorphous component of $A_{400°C}$ = (34 ± 1) % and a crystalline component of $B_{400°C}$ = (66 ± 1) % is found, whereas the spectrum after SPC is approximated with $A_{400°C}$ = (12 ± 1) % and $B_{400°C}$ = (88 ± 1) %.

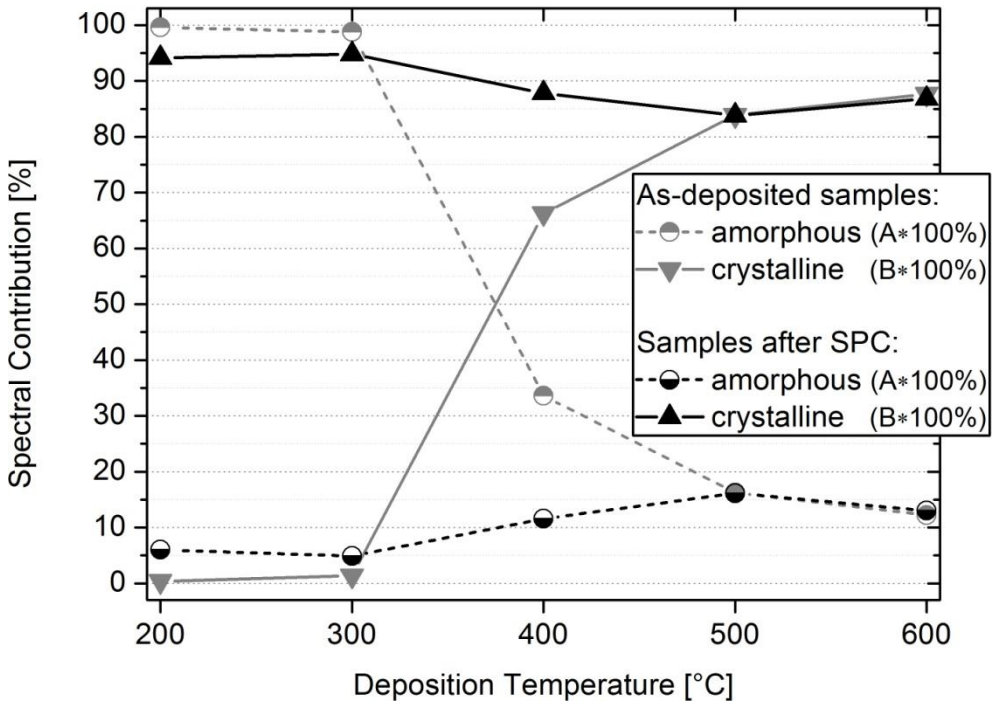

Figure 4.3: Evolution of the spectral contribution of amorphous Si (half-filled circles) and crystalline-Si (filled triangles) to the Si $L_{2,3}$ XES spectra of the Si:H (p^+)/glass samples over deposition temperature before (gray) and after SPC (black).

The accordingly determined spectral contributions for all samples are plotted in Figure 4.3. An increase of the crystalline component of the as-deposited samples with increasing deposition temperature can be observed; the biggest change happens between 300°C [B = (1 ± 1) %] and 500°C [B = (84 ± 1) %]. This is in accordance with the observation by Becker et. al. [26] who observed samples with T_{dep} > 400°C to be microcrystalline. SPC impacts the crystalline component mainly for samples deposited below 400 °C. At 500 °C and 600 °C the changes are within the error bar (± 1 %). The crystalline component decreases with increasing deposition temperature from 300 °C [(95 ± 1) %] to 500 °C [(84 ± 1) %] for samples that underwent SPC. Despite the relatively long SPC annealing time of 24 hours at 650 °C a crystalline component of 100% was not observed in any of the spectra.

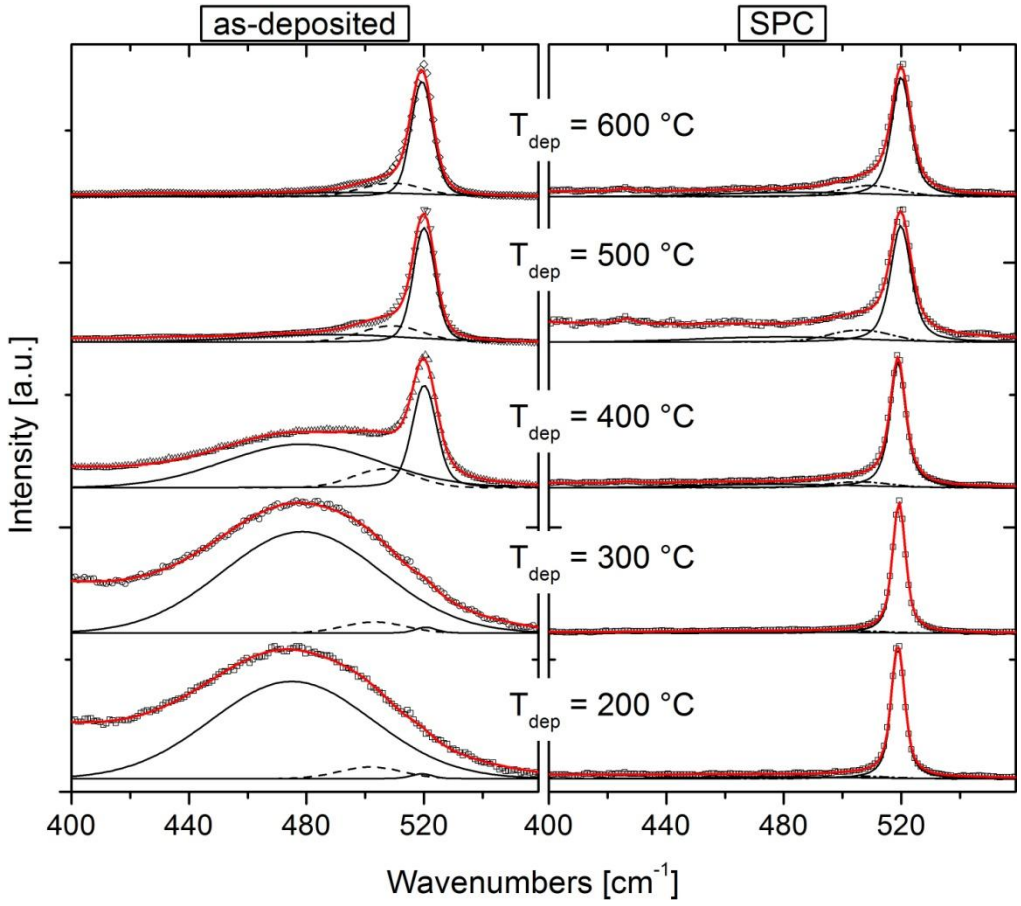

Figure 4.4: Raman spectra of the Si:H (p^+)/glass sample as-deposited (left) and after SPC (right) for different deposition temperatures T_{dep}. Symbols represent the measured spectra while lines represent the fit (red) and its individual component Voigt-profiles at 470 cm^{-1} as well as 520 cm^{-1} (solid lines) and 500 cm^{-1} (dashed line).

To verify these observations with a more classical approach, Raman spectroscopy was applied (as-deposited samples: data re-evaluation of existing data set measured for [26]; SPC: measurements were performed by Janis Jeanne Merkel, HZB). The Raman spectra shown in Figure 4.4 consist of a sharp peak at 520 cm^{-1} ascribed to crystalline silicon due to the F_{2g} symmetry resulting in a $k \approx 0$ limitation [89][103], a broad feature at 480 cm^{-1} representing the whole phonon density of states due to the broken symmetry of amorphous material [89][103] and a further contribution in between (here 507 cm^{-1}) that was previously observed in microcrystalline silicon and explained with either a hexagonal silicon phase [104] or crystallites smaller than 10 nm [105]. These spectra were fitted with fityk [106] using a linear background and three Voigt-profiles centered at wave numbers (520 ± 1) cm^{-1}, (507 ± 3) cm^{-1}, and (480 ± 1) cm^{-1} in order to derive the degree of crystallinity based on Raman spectroscopy.

To calculate the Raman-crystallinity X_c from the integral intensities I of these Voigt profiles the following relation was applied [26]:

$$X_c = \frac{I_{520}+I_{507}}{I_{520}+I_{507}+I_{480}} \qquad \textbf{4.1}$$

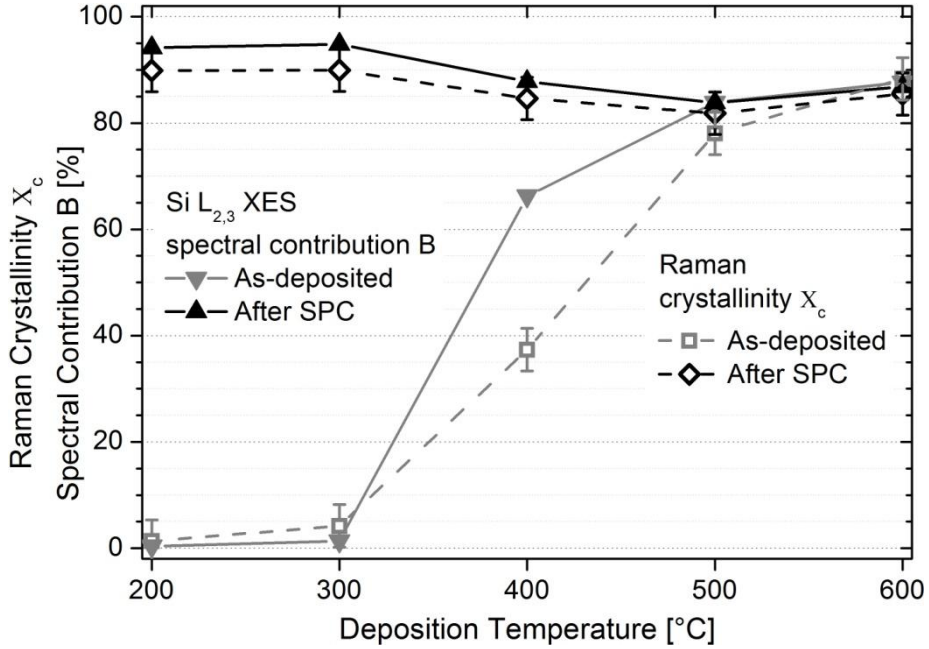

Figure 4.5: Comparison of the evolution of the spectral contribution to the Si $L_{2,3}$ XES spectra corresponding to the crystalline part B (lines and triangles) of the Si:H (p^+)/glass samples as a function of deposition temperature before (gray) and after SPC (black) with the Raman crystallinity X_c (dashes and open squares) before (grey) and after SPC (black).

The Raman crystallinity X_c plotted versus deposition temperature in Figure 4.5 follows the same trend as the crystalline component of the Si $L_{2,3}$ XES spectra (from Figure 4.3). The Raman-derived crystallinity being lower than the crystalline XES component might be explained with a higher cross section of the amorphous 480 cm^{-1} Raman line [91]. (It was not regarded in this evaluation because it is grain-size dependent [91].) The big difference in B and X_c for the T_{dep} = 400 °C as-deposited sample might be due to an inhomogenious crystallization profile over the sample depth; Si $L_{2,3}$ XES is more surface sensitive (attenuation length of 29 nm) than Raman spectroscopy (penetration depth of 2-3 µm [26]). It is also possible that the films crystallize unequally over the sample area due to small temperature gradients during deposition of this particular sample. Note that already small differences would potentially have a significant impact on the T_{dep} = 400 °C sample, as it was obviously produced at a threshold temperature between a-Si and µc-Si growth.

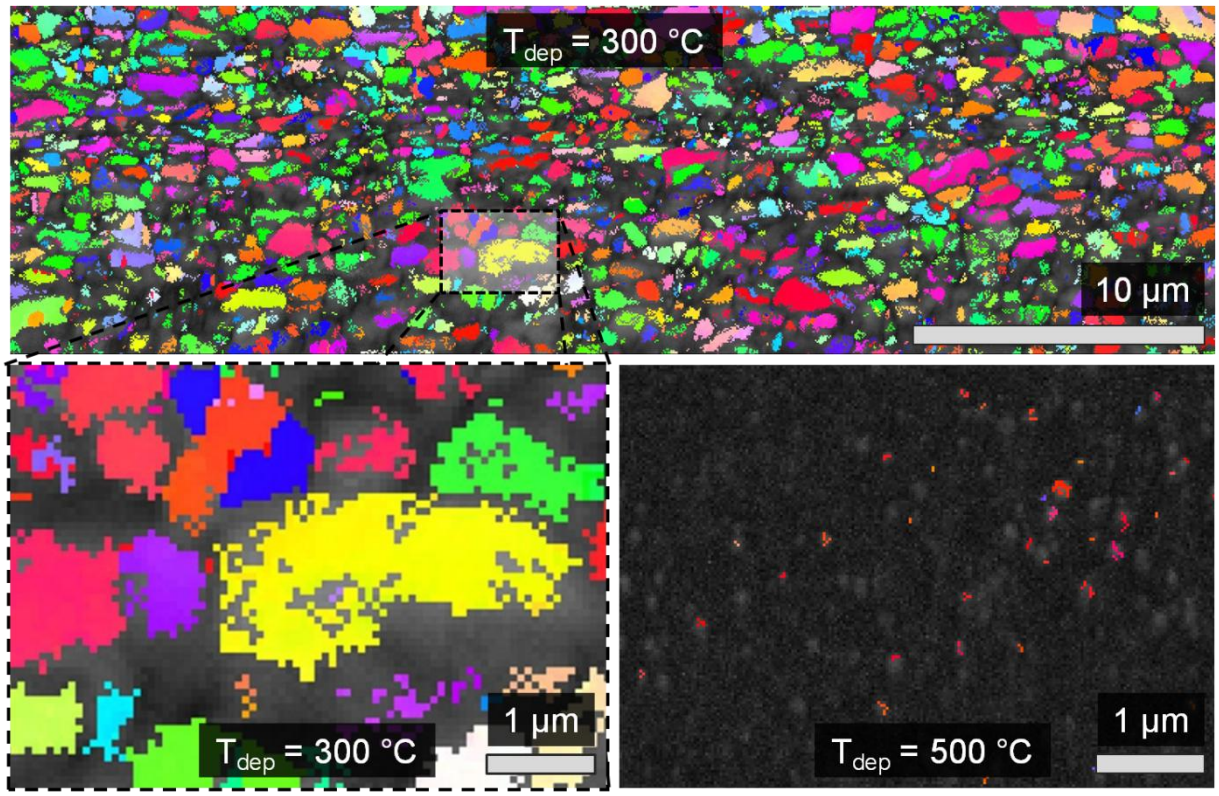

Figure 4.6: EBSD maps of the Si:H (n^+)/glass samples that were deposited at 300 °C (top) or at 500 °C (bottom right) after SPC. The images were measured with different resolutions (top: 0.05 µm/pixel; bottom: 0.02 µm/pixel). The black dotted box indicates the section that was scaled up for comparison to the 500 °C image in the bottom. White bars indicate the scale. Same-colored areas represent the same crystal orientation.

To explain the decreasing crystallinity with increasing T_{dep} for the samples after SPC, samples were additionally characterized with EBSD by Daniel Abou-Ras, HZB. Two example EBSD maps after SPC for samples deposited at of 300 °C and 600 °C are shown in Figure 4.6. Multiple crystallites of several µm can be observed via EBSD for T_{dep} = 300 °C and only a few ~ 100 nm-scale crystallites for T_{dep} = 500 °C (seen as same-colored areas in Figure 4.6). The grey areas represent either crystallites that are below the detection limit of EBSD (≈ 20 nm) or amorphous material. The observed crystallite size after SPC decreases by orders of magnitude with increasing deposition temperature from 300 °C to 500 °C.

Based on these raw data one could speculate that the significant decrease of grain size is related to the crystalline component change from $B_{300°C,\ SPC}$ = 95 % to $B_{500°C,\ SPC}$ = 84 %. In order to investigate this in detail the EBSD images were evaluated quantitatively to estimate the mean grain size, and then models are discussed that might explain this effect.

Non-epitaxially-grown microcrystalline films - and especially poly-Si grown by SPC - exhibit varying grain sizes that can be described by a log-normal grain size distribution [107][108].

Thus the number of grains $n(D_g)$ with a certain grain diameter D_g can be described with the following equation:

$$n(D_g) = \frac{C}{\sigma D_g} \exp\left(-\frac{1}{2}\left(\frac{\ln(D_g/m)}{\sigma}\right)^2\right) \qquad \textbf{4.2}$$

with the log-normal median (m), the log-normal width (σ) and a constant (C). From the EBSD maps the experimental grain size distribution was quantified via image processing, by measuring the grain diameter (i.e., differently colored areas) using the respective pixel count. Minimum grain diameter was 9 pixels - features below 0.2 µm (75 nm) for the 300 °C (500 °C) EBSD map were disregarded.

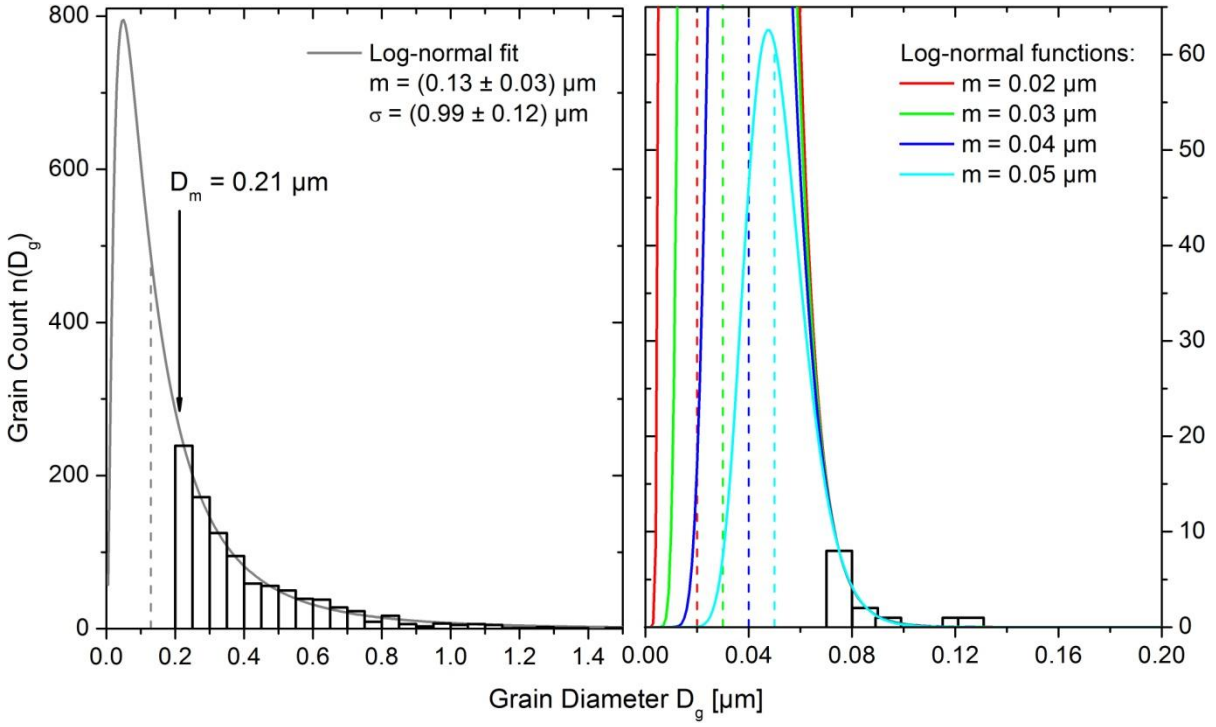

Figure 4.7: Grain size distributions obtained from EBSD maps shown in Figure 4.6 (vertical bars). A log-normal fit according to equation 4.2 is done for the T_{dep} = 300 °C sample (left) and multiple possible fits with various medians m are presented for the T_{dep} = 500 °C sample (right). The respective log-normal medians m are indicated as dashed lines and the center of mass is marked as D_m.

These grain size distributions $n(D_g)$ can be seen in Figure 4.7. As the number of grains seen in the image of the T_{dep} = 300 °C sample was high (989 grains), Equation 4.2 resulted in a good fit of the distribution. To estimate the mean grain size of this distribution function, the center of mass can be determined to D_m = (0.21 ± 0.04) µm. For the T_{dep} = 500 °C sample the

statistics from the EBSD map are far too low to do a fit; a range of curves are shown here. Based on the range of possible curves, a median m < 0.06 µm and therefore a mean grain size of (0.03 ± 0.03) µm is assumed. These values for the mean grain size are related to the XES crystalline spectral fraction B in the following step in which different models are discussed.

It is known that poly-Si [26] and µc-Si [109] thin films exhibit columnar grain structures stretching from the interface to the surface [107]. To model this, cylindrical grains are assumed and furthermore only one single grain with the grain radius R_c is considered. Additionally a surrounding amorphous grain boundary with the thickness T_{gb} is included. A scheme of this Model I is shown in Figure 4.8. The crystalline fraction ϕ_c can be deduced by the following equation, where V_c (V_a) is the crystalline (amorphous) volume:

$$\phi_{c,I} = \frac{V_c}{V_c + V_a} = \frac{R_c^2}{(R_c + T_{gb})^2} \qquad \textbf{4.3}$$

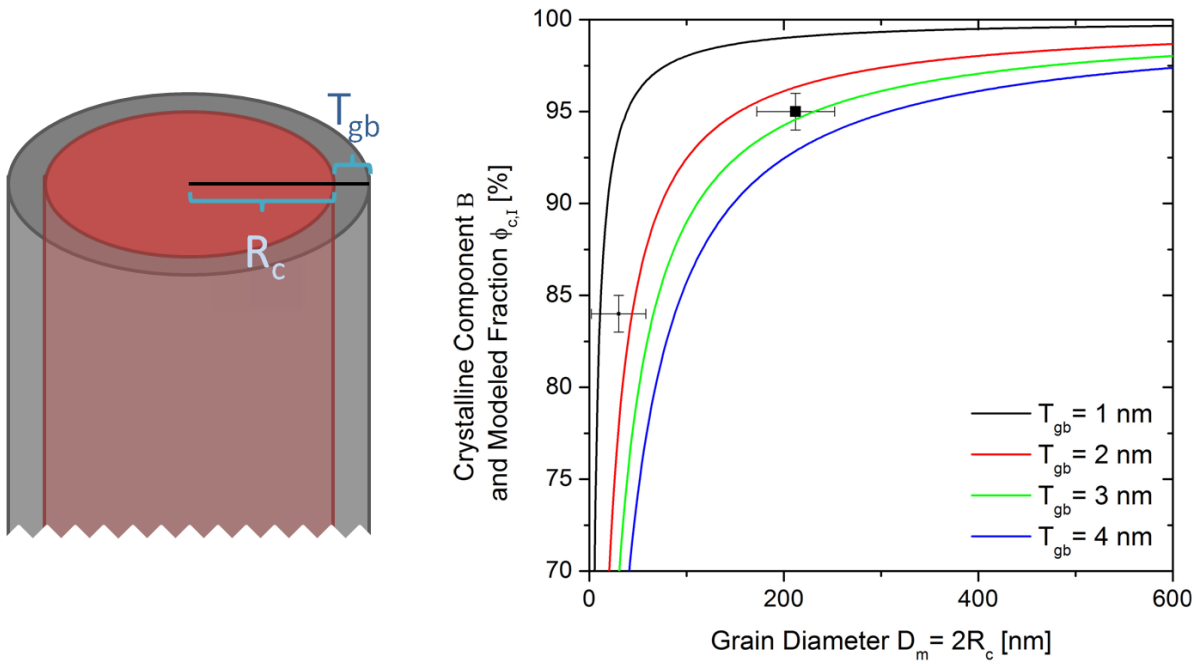

Figure 4.8: Model I: Left: Schematic presentation of a single cylindrical crystalline grain with radius R_c and an amorphous shell with thickness T_{gb}. Right: Comparison of measured Si $L_{2,3}$ XES crystalline component B and estimated EBSD medium grain size D_m compared to crystalline volume fraction $\phi_{c,I}(R_c)$ plots of Model I (equation 4.3) for different grain boundary thicknesses T_{gb}.

Comparing $\phi_{c,I}$ to the measurements of crystalline component B and the estimated mean grain diameters D_m in Figure 4.8 shows that the model agrees reasonably well with the experiment for T_{gb} values between 1 nm and 3 nm.

By adding an additional amorphous surface capping of thickness T_{gb} on top of the cylindrical grain this model is slightly varied. This breaks the depth symmetry, and so Model II has to take the attenuation of the x-ray photons with the effective attenuation length λ_a^* into account:

$$\phi_{c,II} = \frac{R_c^2 e^{-\frac{T_{gb}}{\lambda_a^*}}}{(R_c + T_{gb})^2} \qquad \textbf{4.4}$$

Although λ_a^* for c-Si and a-Si varies slightly due to the lower density of a-Si, the value for c-Si is used (29 nm [80]; see chapter 3.3). A visualization of the model and a comparison with the experimental values can be seen in Figure 4.9.

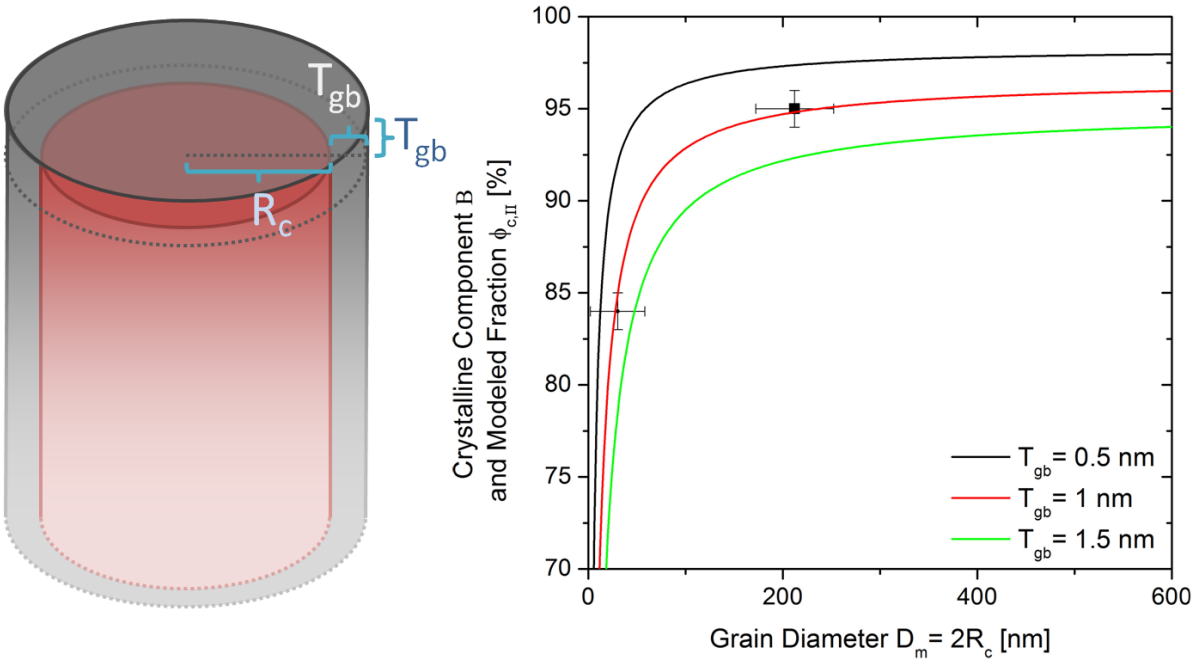

Figure 4.9: Model II: Left: Schematic presentation of a single cylindrical crystalline grain with radius R_c, an amorphous shell and an amorphous capping layer of thickness T_{gb}. Right: Comparison of measured Si $L_{2,3}$ XES crystalline component B and estimated EBSD medium grain size D_m compared to $\phi_{c,II}(R_c)$ plots of Model II (equation 4.4) for different grain boundary thicknesses T_{gb}.

A good agreement between experiment and model is possible with $T_{gb} \approx 1$ nm. As T_{gb} is the distance between two adjacent grains, it can be considered twice the surrounding amorphous area of a single grain. Thus the top cover layer can be estimated as ½ T_{gb}, which results in the Model III with the equation:

$$\phi_{c,III} = \frac{R_c^2 e^{-T_{gb}/(2\lambda_a^*)}}{(R_c + T_{gb})^2} \qquad \textbf{4.5}$$

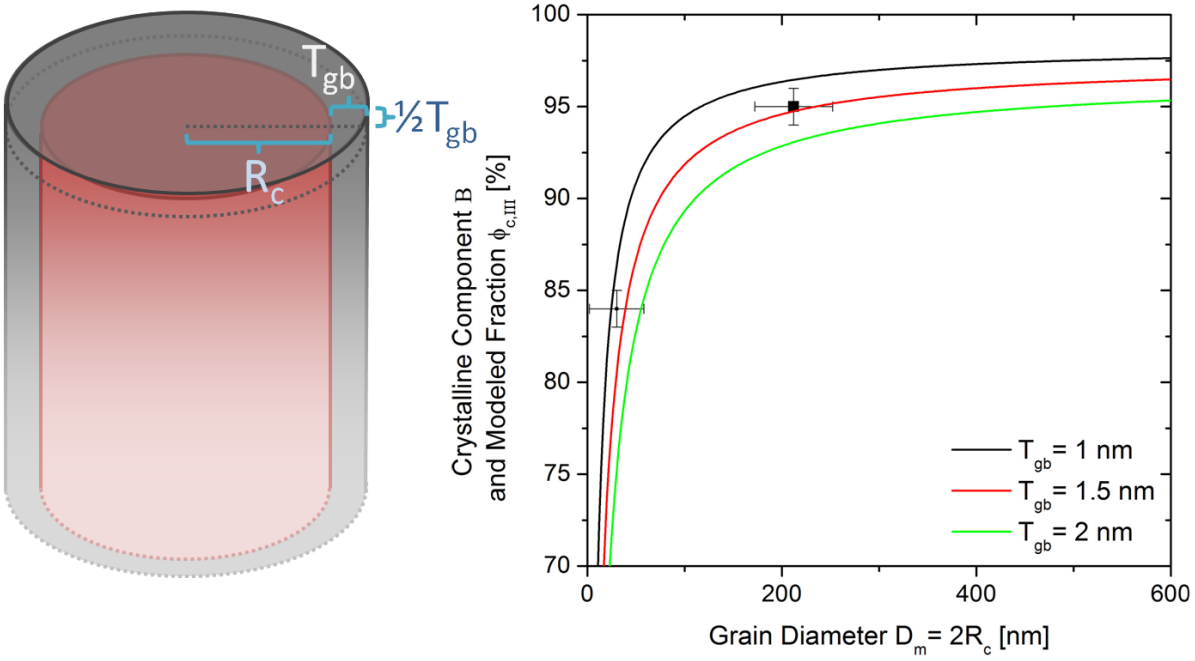

Figure 4.10: Model III: Left: Schematic presentation of a single cylindrical crystalline grain with radius R_c, an amorphous shell T_{gb} and an amorphous capping of thickness ½ T_{gb}. Right: Comparison of measured Si $L_{2,3}$ XES crystalline component B and estimated EBSD medium grain size D_m compared to $\phi_{c,III}$ plots of Model III (equation 4.5**)** for different grain boundary thicknesses T_{gb}.

In Model III T_{gb} values between 1 nm and 1.5 nm seem to agree with the experiment. The current data base is, however, not sufficient to decide on one of the presented models - additional experimental (EBSD) data is needed but Model II and III seem to describe the experiment slightly better than Model I. For a future examination, it would be worth considering models that implement multiple grains, a grain size distribution and the non-normal sample orientation during XES measurements (45° in / 45° out).

Despite the limited data base and the related shortcomings, it can however be concluded that the quantified XES data is in agreement with samples consisting of columnar grains with amorphous intergrain boundaries. The models suggest that the boundary thickness is on the nm-scale. Note that amorphous here may also mean distorted material between different grain orientations rather than a true amorphous intergrain matrix.

In conclusion the Si $L_{2,3}$ XES spectra of poly-Si and µc-Si samples were well-described by a superposition of a-Si and c-Si spectra. Even after extended SPC time, every sample showed a remaining a-Si contribution. Raman spectroscopy verified the qualitative trend of the crystalline contribution of the XES spectra and therefore verifies, that Si $L_{2,3}$ XES can be used with at least equal precision to evaluate crystallinity of µc-Si, poly-Si and a-Si samples.

Further evidence found through EBSD analysis, data evaluation and modeling strongly suggests that the remaining a-Si contribution is due to distorted material at the border of (columnar) grains. Although there remains much more work to complete this investigation, these findings enable and ease the interpretation of Si $L_{2,3}$ XES spectra in the following chapters and future investigations.

As a closing point to this analysis, one should keep in mind that even for thin film Si layers consisting of big crystallites (on the µm scale) and prolonged SPC treatment, the crystalline fraction B (determined by Si $L_{2,3}$ XES) always stays measurably below 100 % (of course due to the direct comparison of poly-Si with a monocrystalline wafer).

4.2 Influence of dopants

After presenting and discussing the Si $L_{2,3}$ XES spectra of amorphous, crystalline, microcrystalline and polycrystalline silicon and investigating the influence of different grain sizes in subchapter 4.1 and establishing a viable quantification approach, this subchapter is centered on how different dopants influence the crystallization of amorphous Si.

Samples were provided by Mark Wimmer, HZB. They were prepared by PECVD on ZnO:Al/glass substrates. A comparison to films deposited on SiN_x/glass can be seen in subchapter 4.4.

Using PECVD 50 nm thick a-Si:H layers were deposited on 900 nm ZnO:Al that was previously rf-sputtered onto Corning Eagle XG® glass substrates. For p^+ (n^+) doped samples the B_2H_6/SiH_4 (PH_3/SiH_4) mole ratio C_B (C_P) during PECVD was 1.0×10^{-2} (2.0×10^{-3}). The substrate temperature was at 130 °C (p^+ a-Si:H), 210 °C (intrinsic a-Si:H) or 190 °C (n^+ a-Si:H) during deposition, which is expected to result in mainly amorphous Si.

One sample of each series was kept as-deposited while the others underwent SPC processes using different time (from 2 to 24, 66 hours) and temperatures (600 °C, 650 °C). To minimize contact with ambient air the samples were sealed in N_2 atmosphere after deposition and SPC and underwent a HF dip (30 s in 0.5% HF in H_2O solution) right before the experiment to remove the surface oxide. HF-etched monocrystalline P-doped Si(n)-wafer [(9000…13000) Ωcm; (2.87×10^{11}...4.78×10^{11}) cm^{-3}] and a piece of Corning Eagle XG® glass (SiO_2) were used as references.

Si $L_{2,3}$ XES spectra for the three different doping series (n^+, intrinsic and p^+) are shown in Figure 4.11. Spectra of eight samples with different SPC plateau heating times at 600 °C (for 2, 4, 8, 12, 20 and 24 hours) and 650 °C (for 24 and 66 hours) as well as the as-deposited sample are plotted for each series.

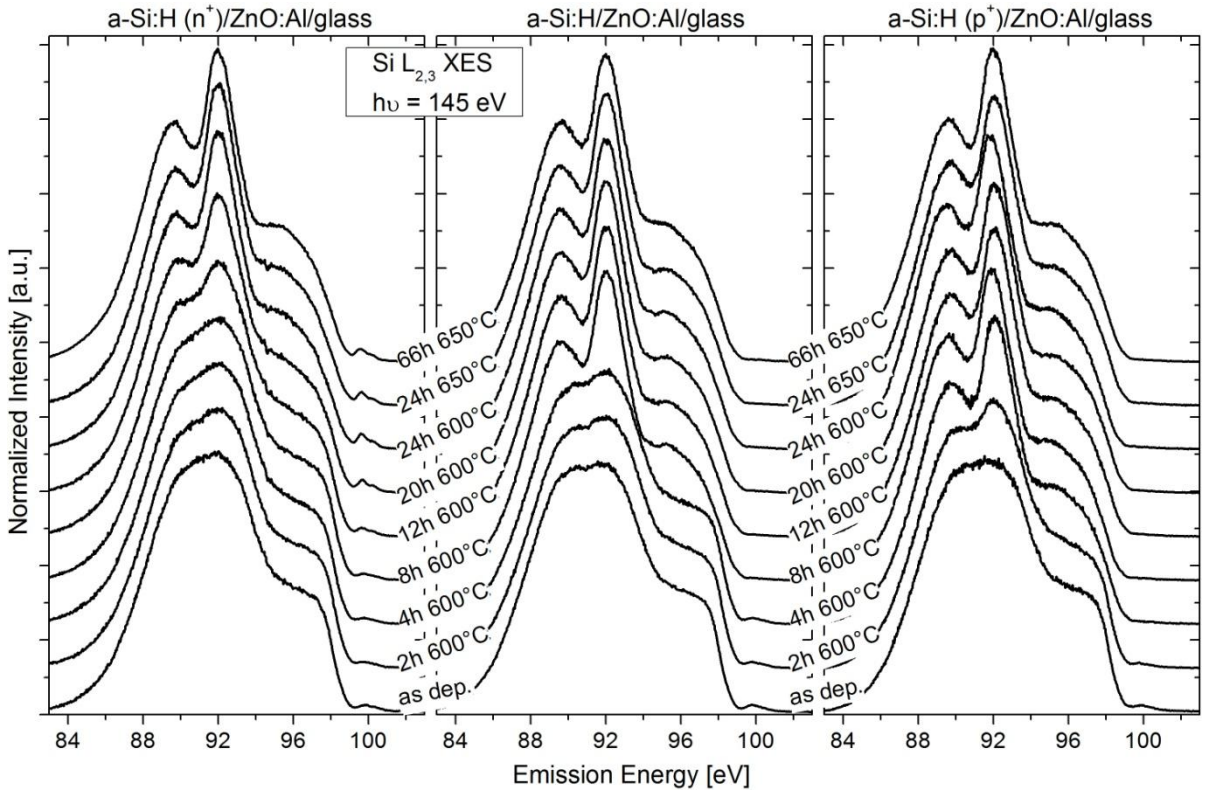

Figure 4.11: Area normalized Si $L_{2,3}$ XES spectra of a-Si:H (n^+)/ZnO:Al/glass (left), a-Si:H /ZnO:Al/glass (center) and a-Si:H (p^+)/ZnO:Al/glass (right) samples. Each series includes an as-deposited sample and samples that underwent different SPC processes (2 hours to 24 hours at 600 °C and 24 hours as well as 66 hours at 650 °C).

The Si $L_{2,3}$ XES spectra of the samples of all three series exhibit an evolution from an a-Si like to a c-Si spectrum (compare discussion in subchapter 4.1). The clearest difference between the series is the slower appearance of a distinctive c-Si shape for the n^+ series compared to the p^+ doping series. A slight energy shift in two spectra of the p^+ series can be observed (8 h 600 °C; 24 h 650 °C). This effect is likely attributed to an energy shift caused by an accidental contact of the sample with the first optical element of the spectrometer (the entrance slit).

Above the valence band edge around 100 eV a small contribution can be observed in some of the spectra. Figure 4.12 shows a close-up on these features. They disappear for the intrinsic and p^+ doping while sharpening and gaining in intensity for the n^+ series during SPC. For the untreated (i.e., a-Si) samples, the intensity of the peaks is highest in the intrinsic series and lowest in the n^+-doped series. However, a quantitative evaluation of these peaks is problematic from these spectra due to experimental broadening and the close vicinity to the

valence band edge. Later in this chapter, more detailed (i.e., higher-resolved) spectra are shown and discussed to investigate these features.

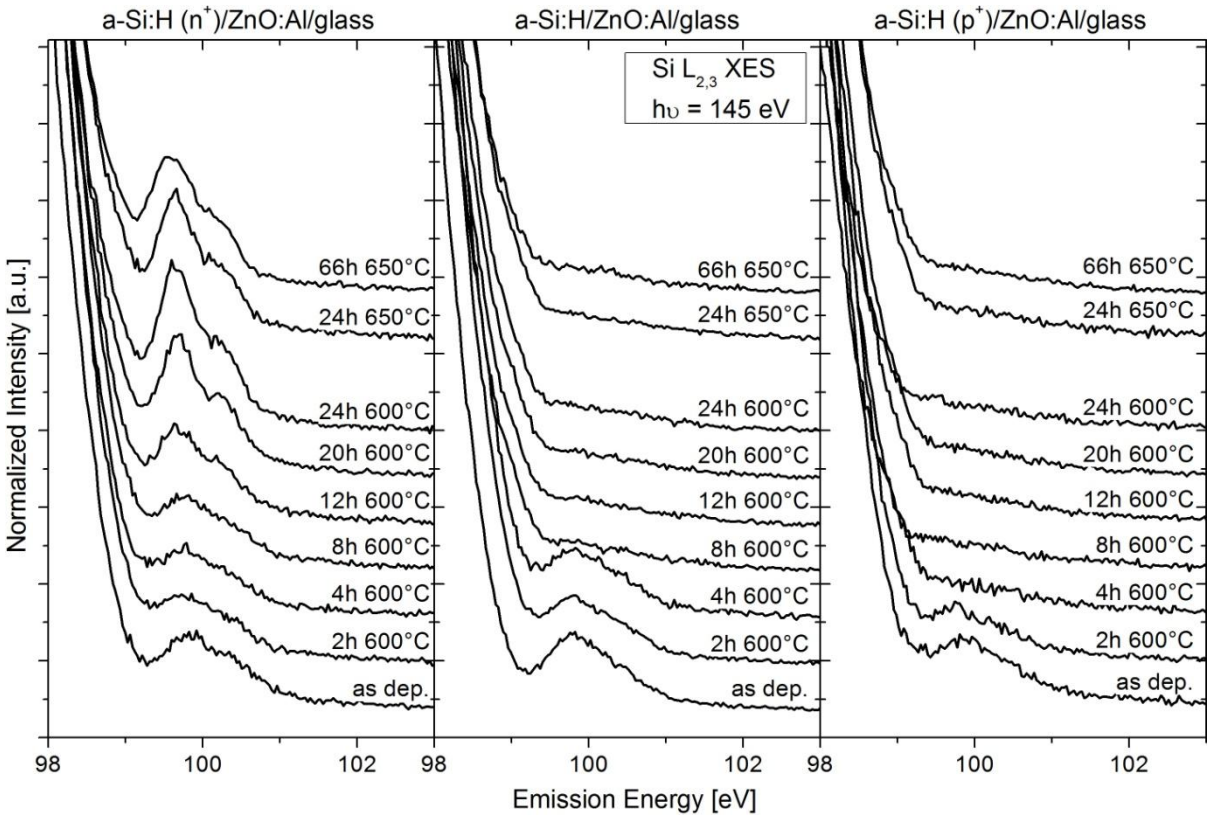

Figure 4.12: Close up on the valence band edge of the normalized Si $L_{2,3}$ XES spectra in Figure 4.11.

Similar to subchapter 4.1 the spectra from Figure 4.11 were presented as a superposition of reference spectra (i.e., $I_{sample}=A\cdot I_{a\text{-}Si}+B\cdot I_{c\text{-}Si}+C\cdot I_{SiO_2}$) to quantify the degree of crystallinity. The as-deposited sample of the respective series is used as the a-Si reference, and the monocrystaline wafer is used for the c-Si reference. In contrast to the samples studied before, the addition of a SiO_2 reference spectrum to the superposition resulted in a better fit especially for most of the samples with SPC times over 18 hours. This might be explainable with SPC-induced oxidization of the buried ZnO/Si interface discovered in previous investigations [110][111]. Example fits for all three series are shown in Figure 4.13.

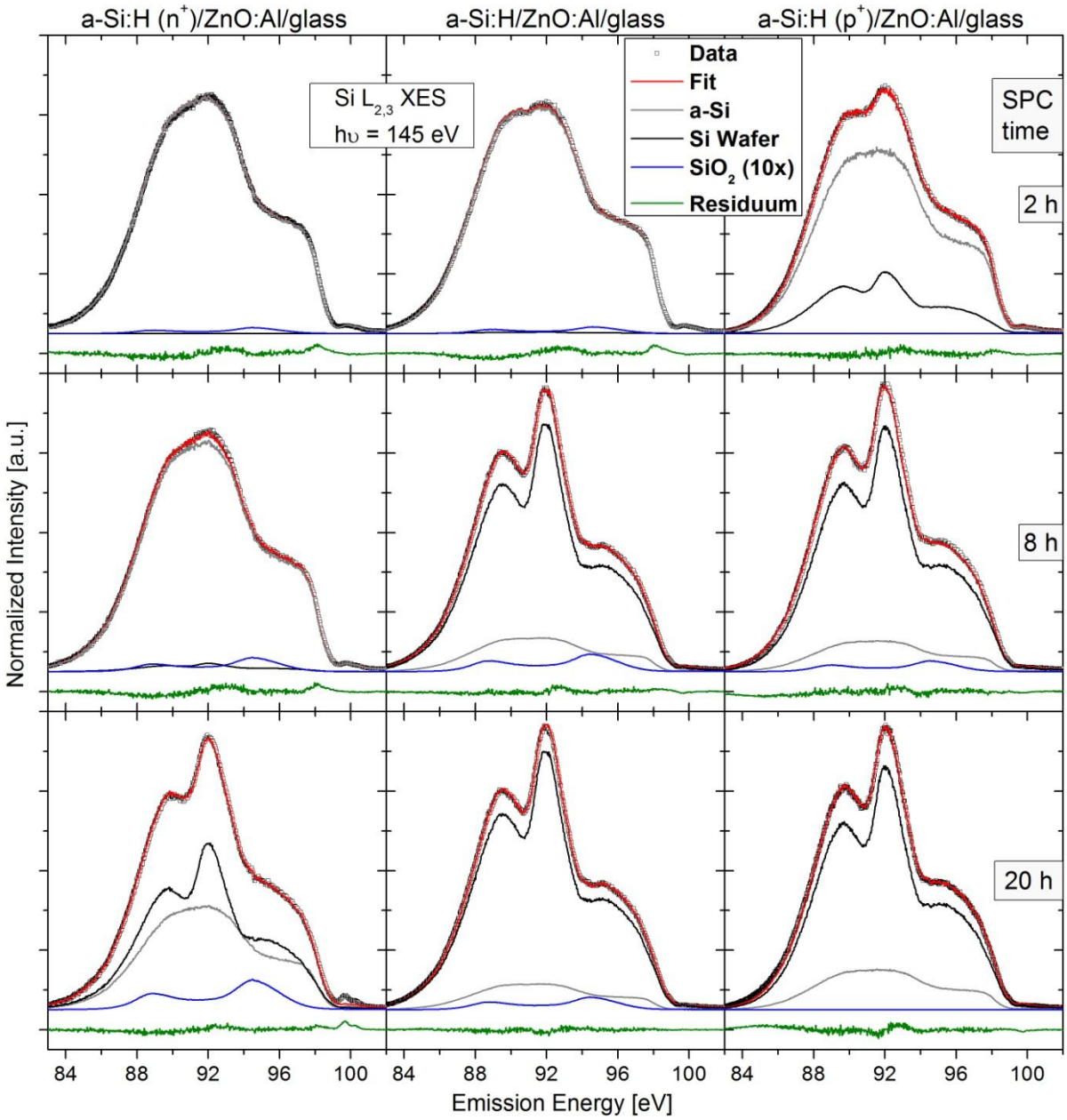

Figure 4.13: Example fits (red) of the Si $L_{2,3}$ XES spectra for the 2, 8 and 20 hours 600 °C heated samples (□) for the three sample series of n^+, intrinsic, and p^+ a-Si:H on ZnO:Al. Weighted references of a-Si:H (with or without dopant)/ZnO:Al/glass (grey), Si-Wafer (black) SiO_2 (blue, ×10) are given and the respective residua are shown in green.

According to the residua the superposition approximation works well for all samples. Minor deviations occur in the residua of the a-Si like samples at the valence band onset at 98 eV (especially visible in the 2 h data), and for n^+ doped c-Si like samples at 100 eV (feature above the valence band edge; see bottom left spectrum in Figure 4.13). Due to the mentioned energy scale issues in some of the measurements of the p^+ sample series some spectra were shifted before fitting (8 h 600 °C: +0.08 eV; 24 h 600 °C: +0.83 eV).

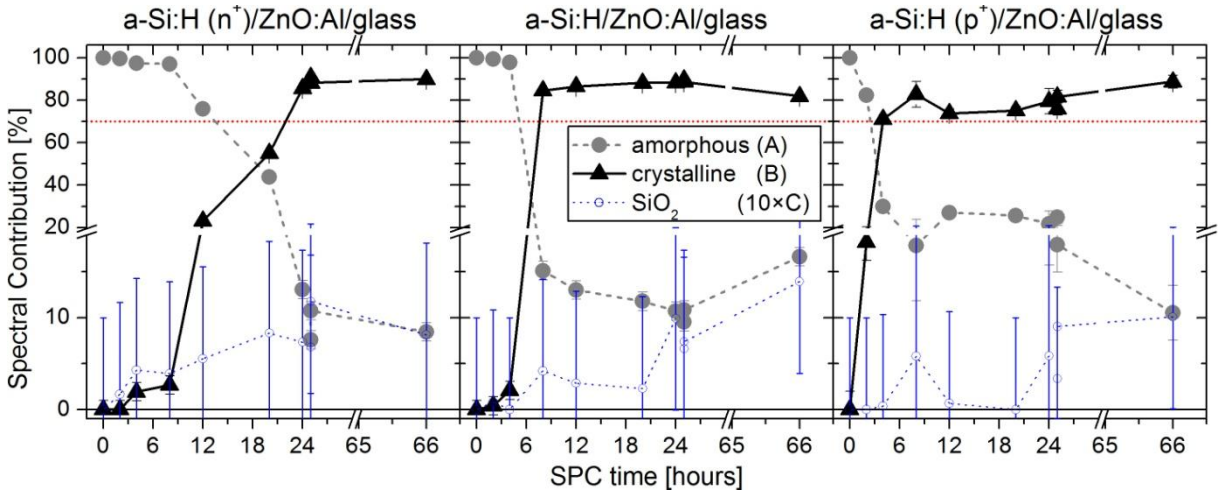

Figure 4.14: Evolution of the a-Si (●), c-Si (▲) and SiO_2 (○) spectral contribution to the Si $L_{2,3}$ XES spectra of the three series of Si:H/ZnO:Al/glass over SPC time (600 °C for 2 h – 24 h and 650 °C for the last 3 data points at 24 h and 66 h) (Absolute error: ± 1% [smaller than symbol size] or ± 5 % for energy shifted spectra). Note the scaling (×10) of the SiO_2 component, the differently scaled y-axis above / below 20 % and the break of the x-axis between 28 and 65 hours.

The respective spectral components of all fits are plotted in Figure 4.14. For the n^+ (intrinsic) series a minor increase of c-Si component to 3 % (2 %) occurs in the first 8 hours (4 hours) while the p^+ series exhibits a c-Si component of 18 % already after 2 hours. A c-Si component above 70 % is reached after 24 h for n^+, 6 h for intrinsic and 4h for p^+ doping. For all three series the maximal c-Si component is (89 ± 1) %. (The further increase or decrease (intrinsic) of the c-Si component for the 66 h 650 °C measurement might be due to the fact that these samples were additionally prepared from the existing as-deposited material and measured months after the initial measurements).

Although the SiO_2 component stays below the error bars (1%) for most measurements, a general trend of an increase with SPC time is noticeable for all three series.

An increase of crystallization speed with a-Si:H doping was previously reported by Bisaro et. al [87]. Lateral crystallization velocities V_g of up to 6 times the intrinsic speed were found for high boron doping ($C_B = 2\times10^{-3}$; V_g = 6.7 Å/s; intrinsic: V_g = 1.25 Å/s). Also for phosphorous doping an increase of V_g was observed. It was highest for a medium dopant concentration ($C_P=3\times10^{-4}$; V_g=1.9 Å/s) and slightly decreased back towards the intrinsic value for a higher dopant concentration ($C_P = 2\times10^{-3}$; V_g = 1.3 Å/s). But a decrease of V_g with n^+ doping, as seen above, was not observed. Noteworthy are the difference in deposition temperature (600 °C), method (chemical vapor deposition), substrate (fused silica) and thickness

(100 nm - 1 µm) in the study by Bisaro et. al. which might cause the different findings. The decreased crystallization velocity for n^+ doping is noteworthy and the governing process is worth investigating in further studies.

The observation that the crystalline component never exceeds 90 % should be due to the amorphous/disordered grain boundary contribution to Si $L_{2,3}$ XES spectra found in subchapter 4.1. Using Model III and estimating T_{gb} to be 1.5 nm a mean grain diameter of 50 nm could be estimated for the here studied samples. The increasing SiO_2 amount with increasing SPC time is in agreement with earlier findings of a SPC induced a-Si:H/ZnO:Al interface oxidation [110][111].

In order to investigate the fast crystallization of the p^+ Si and the behavior of the boron dopant further, B K XES and XAS spectra were taken and are shown in Figure 4.15.

The XES spectra of the B K edge are overlapped with a third order O K peak at 175 eV (ascribed to the ZnO:Al substrate [110]). As for the Si $L_{2,3}$ XES also the B K XES spectra exhibit a distinct transition from the amorphous to the crystalline shape. Features that are correlated to Si 3p derived states (**C**) and hybridized Si s-p derived states (**B**) in Si $L_{2,3}$ XES [99] (compare discussion in subchapter 4.1), can also be found for B K XES spectra with approximately the same relative distance but a different relative intensity. Contribution (**A**) which is ascribed to Si 3s derived states in the Si $L_{2,3}$ XES spectra [99] is missing in the B K spectrum. This suggests little interaction between the Si 3s and the B 2s and B 2p states.

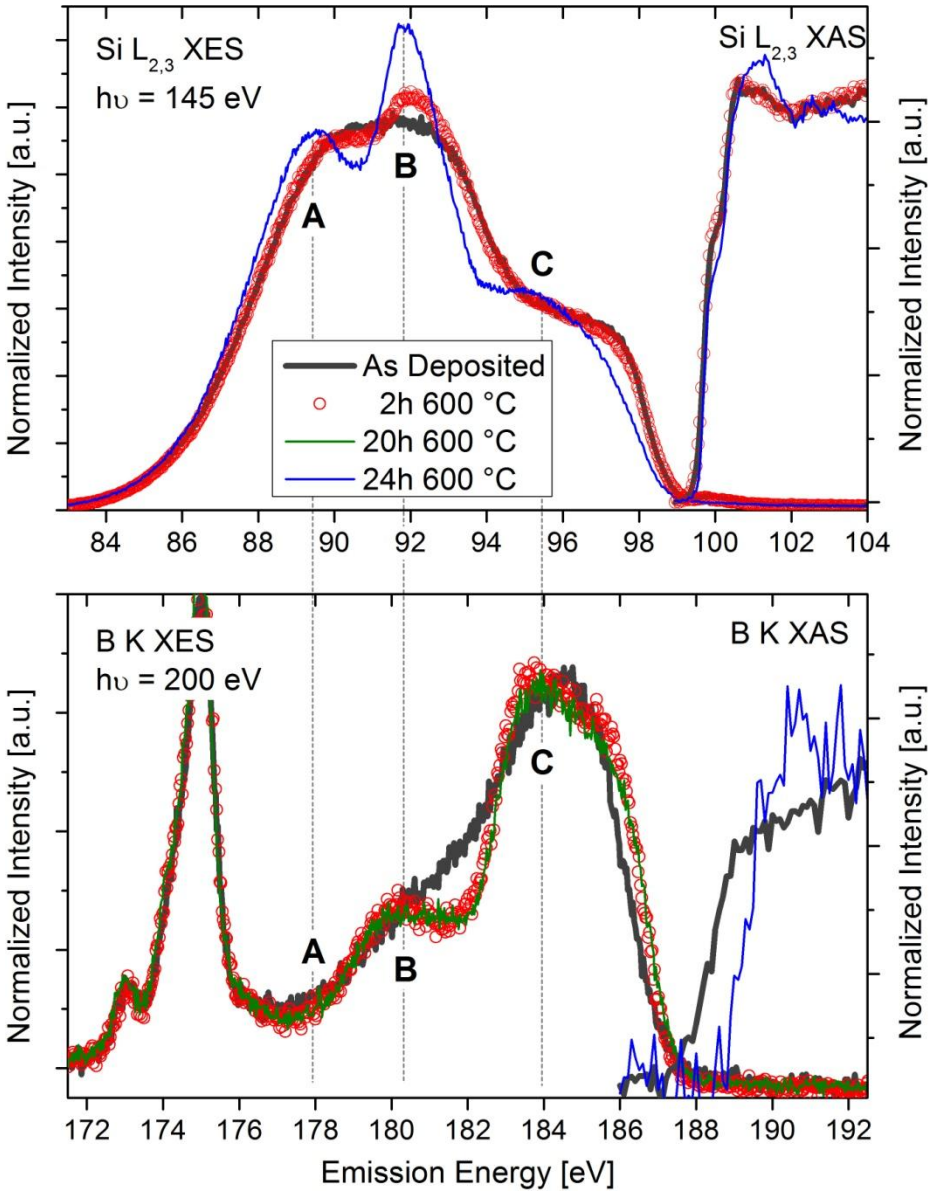

Figure 4.15: Si $L_{2,3}$ XES and XAS (top) as well as B K XES and XAS spectra (bottom) of p^+ SPC time series samples (Si $L_{2,3}$ XES spectra are the same as shown in Figure 4.12). Spectra of an as-deposited sample (dark grey lines) are compared to spectra from samples with 2h (○), 20 h (green line) and 24 h (blue line) SPC treatment at 600 °C.

The intensity of contribution (**B**) relative to (**C**) might be reversed in B K XES because the optical transition Si 3p → Si 2p in Si $L_{2,3}$ XES is forbidden due to dipole selection rules, as for B K XES the 3p → 1s transition is not dipole forbidden. Very interesting is the fact that the 2 h 600 °C B K XES spectrum resembles the Si $L_{2,3}$ XES spectrum of the crystallized 20 h 600 °C and not that of the amorphous as-deposited sample. Here, B K behaves contrary to Si $L_{2,3}$ XES. This suggests that silicon around the boron atoms may crystallize faster which is hinting towards boron acting as a crystallization seed, which would also explain the

previously discussed faster crystallization of boron doped a-Si:H (as compared to intrinsic a-Si:H).

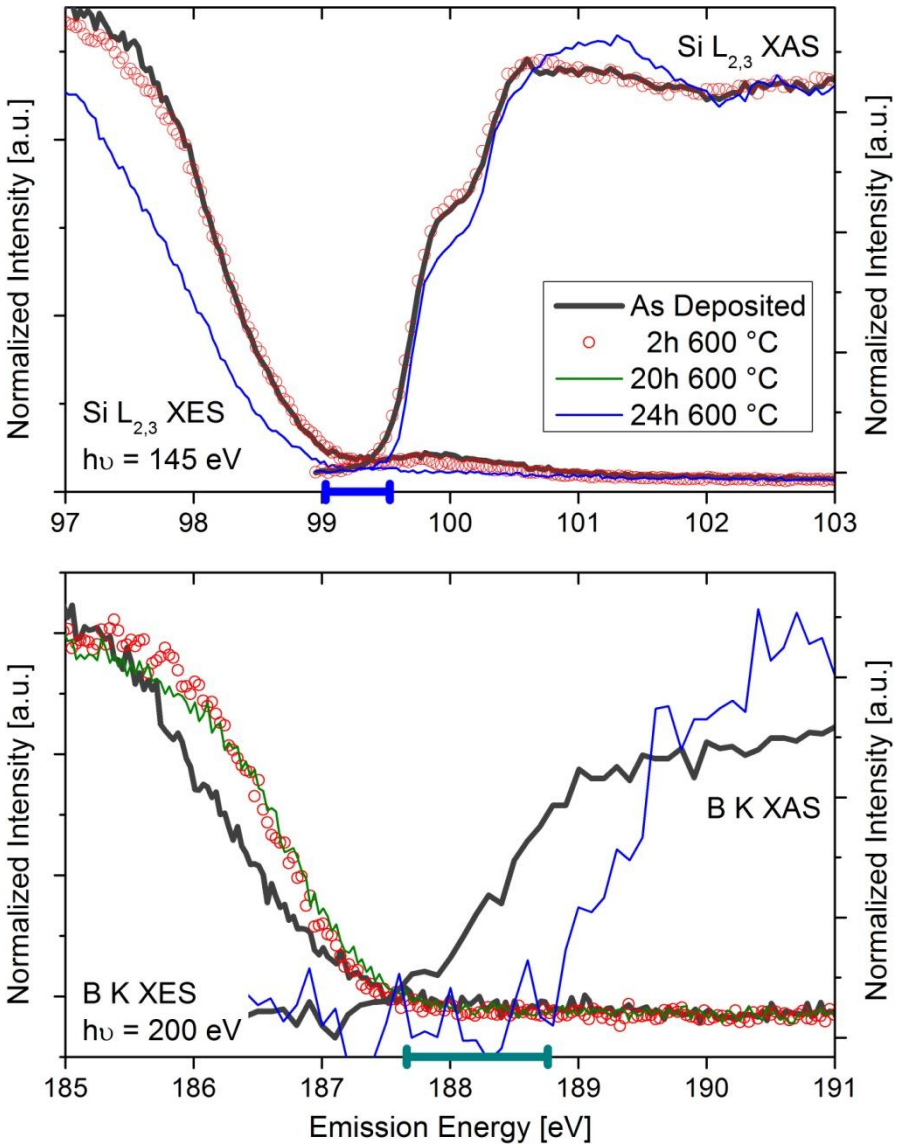

Figure 4.16: Magnification of band gap region of the same spectra shown in Figure 4.15. Bars indicate the expected band gap for c-Si (blue and cyan).

Figure 4.16 shows the magnified region of the band gap. For comparison the values of the indirect band gap of monocrystalline Si is indicated. The Si 2p spin-orbit split of approximately 0.6 eV [112] has to be taken into account for Si $L_{2,3}$ XES by reducing the value for the monocrystalline Si band gap to 0.5 eV from the expected value of 1.1 eV [113]. This is apparent because the Si $L_{2,3}$ XES valence band maximum (VBM) is determined with the L_3 transition into the Si $2p_{3/2}$ and the conduction band minimum (CBM) with the L_2 transition from the Si $2p_{1/2}$ core level. These values for the band gap compare well with the energy difference between the VBM (edge of XES spectra) and the CBM (onset of the XAS spectra)

of the samples after SPC (20 h or 24 h 600 °C) for both B K and Si $L_{2,3}$. A bigger band gap of amorphous compared to the crystalline Si can be neither observed in the Si $L_{2,3}$ nor in the B K spectra which could be due to the band tails reaching into the gap (see discussion in chapter 2.1.1), high concentration of defect states in the gap of a-Si:H [14] and core excitons (chapter 3.3).

The VB emission close to the onset of a-Si:H(B) is lower in intensity for B K XES and higher for Si $L_{2,3}$ XES when compared to that of poly-Si:H(B). Furthermore it appears, that the a-Si:H(B) CB is reaching more into the gap for B K compared to Si $L_{2,3}$ XAS.

The feature that is observed in Si $L_{2,3}$ XES at 100 eV cannot be found in the B K XES. A reason could be that the features are occupied at Si sites and unoccupied at B sites. The low-energy onset of the conduction band found in the corresponding B K XAS spectrum suggests a possible direct interaction between the B dopants and the a-Si defect states (chapter 2.1.1).

In conclusion, SPC of 50 nm thin a-Si layers with different dopants on ZnO:Al/glass substrates were investigated with Si $L_{2,3}$ soft x-ray emission spectroscopy. The change from amorphous to crystalline Si was directly visible in the measured spectra and the quantification approach based on spectral superposition of amorphous, crystalline Si, and silicon dioxide references (as introduced in chapter 4.1) allowed a good representation of the measured spectra. By comparing these spectral components the crystallization velocity could be evaluated. It is faster for p^+ (B) but much slower for n^+ (P) dopants if compared to the crystallization of undoped (intrinsic) a-Si:H on ZnO:Al. Through this evaluation a confirmation for oxidation at the Si-ZnO:Al interface was found. In Si $L_{2,3}$ XES spectra of a-Si:H and n^+ poly-Si, a small feature above the valence band edge was observed that was studied further in detail. A direct correlation between the feature intensity and the crystallinity of the n^+ poly-Si was found. Two different origins for the feature – defect states in a-Si and occupied dopant states were proposed. By measuring B K XES and XAS spectra a similarity to Si $L_{2,3}$ XES and XAS spectra was observed. Upon SPC, the B K XES specta changed in a similar fashion as the Si $L_{2,3}$ XES spectra. But the spectral changes occur at different stages of the SPC process (earlier for B K XES). Therefore one could speculate that crystallization starts earlier around the boron atoms. Boron therefore might act as a crystallization center.

4.3 Si $L_{2,3}$ XES features above the valence band maximum at 100 eV

This subchapter is dedicated to the further investigation of the feature that was observed in Si $L_{2,3}$ XES spectra of as-deposited a-Si:H and phosphorous-doped poly-Si samples above the valence band edge at 100 eV. During this study, such features were also observed in highly P-doped monocrystalline Si (P; 10^{20} cm^{-3}) [spectra not shown here]. In literature, similar features were observed in Si $L_{2,3}$ XES spectra of a-Si:H [101][114] and were speculated to be related to H 2s states. Sulfur ion-implantion into c-Si also results in a similar effect, which was shown in a different study by our group [115]. A detailed explanation of the origin is currently in preparation by our group.

To investigate them further, detail spectra of the respective spectral region with a higher energy resolution were taken for the n^+ series. These spectra can be seen in Figure 4.17. By using a narrower spectrometer entrance slit and a shallower detector angle (0° instead of 10°), the pixel/eV and the resolution was increased from 0.032 eV to 0.015 eV. Therefore the features above the VBM could be resolved better than shown in Figure 4.11. As mentioned earlier the features gain in intensity and get sharper upon SPC. Additionally a peak shift can be observed.

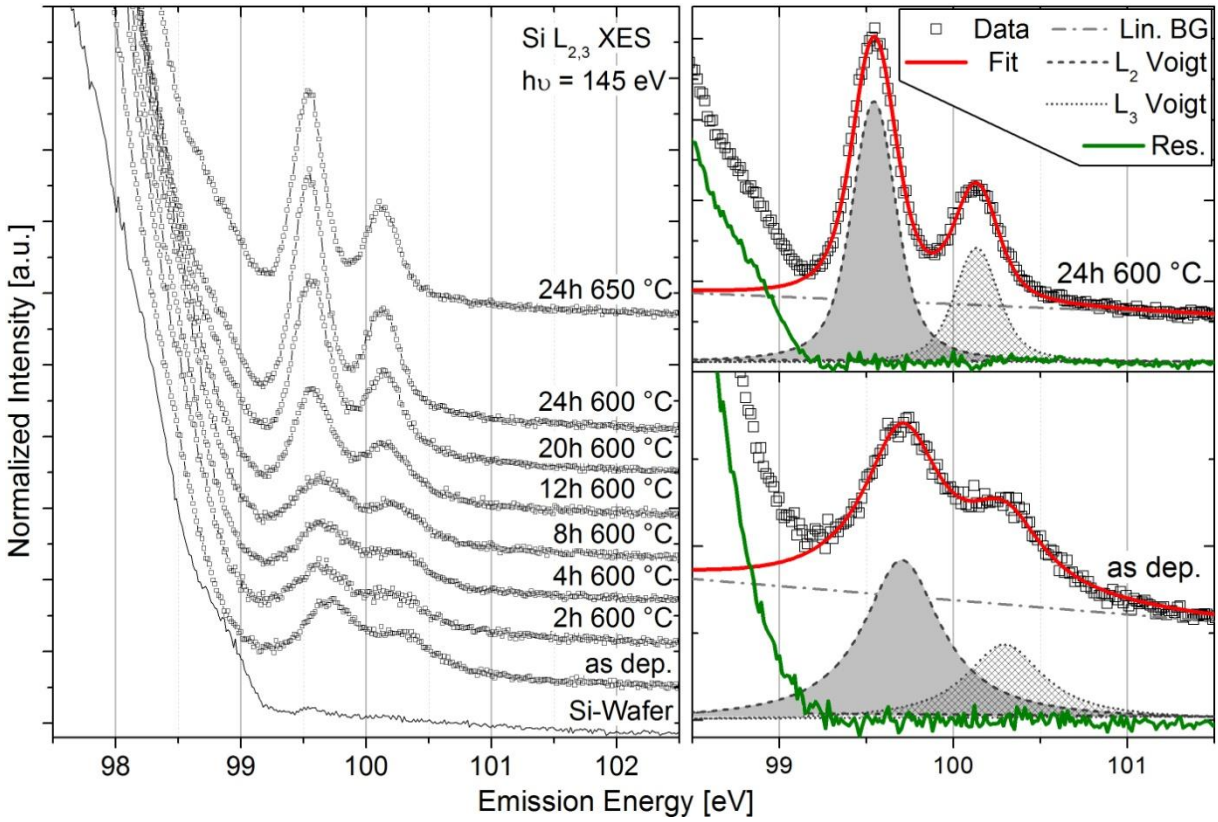

Figure 4.17: Left: Si $L_{2,3}$ XES valence band edge region high-resolution detail spectra of the n^+ SPC time series Right: The two features next to the valence band edge were fit (red line) with a linear background (dash-dotted line) and two width- and distance-coupled Voigt profiles (filled curves), which is shown for the as-deposited (top) and the 24 h 600 °C (bottom) sample.

To quantify this effect, the spectral features were fit with fityk [106] by assuming a linear background and two Voigt profiles. To constrain the fit parameters, they were linked with a separation of 0.59 eV, the same width and the same shape. This is justified due to the spin-orbit split of the Si 2p [112] core level, which results in the spectral double features L_2 and L_3. This fit procedure describes the feature well for all shown spectra, which is demonstrated for two examples in Figure 4.17. During SPC a transition of the L_2 feature from a low intensity at (99.70 ± 0.02) eV with a FWHM of (0.55± 0.03) eV for the as-deposited sample, to a higher intensity at (99.55 ± 0.02) eV with a narrower FWHM of (0.30 ± 0.03) eV for the 24h 650 °C sample can be observed.

The fact that the feature disappears for intrinsic and p^+ Si thin films and that it shifts, narrows and gains in intensity for n^+ doping suggests that it has an a-Si related and a n^+ doping related origin. Hence, it is valid to assume that it is a superposition of (at least) these two different contributions.

To test this assumption, the crystallized 24 h 600 °C spectrum is fit by using two sets of peaks: one determined from the previous fit of the as-deposited sample [L_2 at (99.70 ± 0.02) eV, FWHM of (0.55± 0.03) eV] with an intensity scaled down by the a-Si spectral contribution (13 %; see Figure 4.14) and a new additional pair of coupled Voigts. By doing so, this new "n^+ related" (a-Si free) contribution can be determined to a L_2 position of (99.54 ± 0.02) eV and width of (0.29 ± 0.03) eV. The remaining spectra are now fit with this n^+ related and the a-Si related Voigt couples – leaving the intensity as free parameters. The result of this fit procedure and the resulting intensities are shown in Figure 4.18. This model describes the changes occurring with SPC better with two separate contributions with fixed energies.

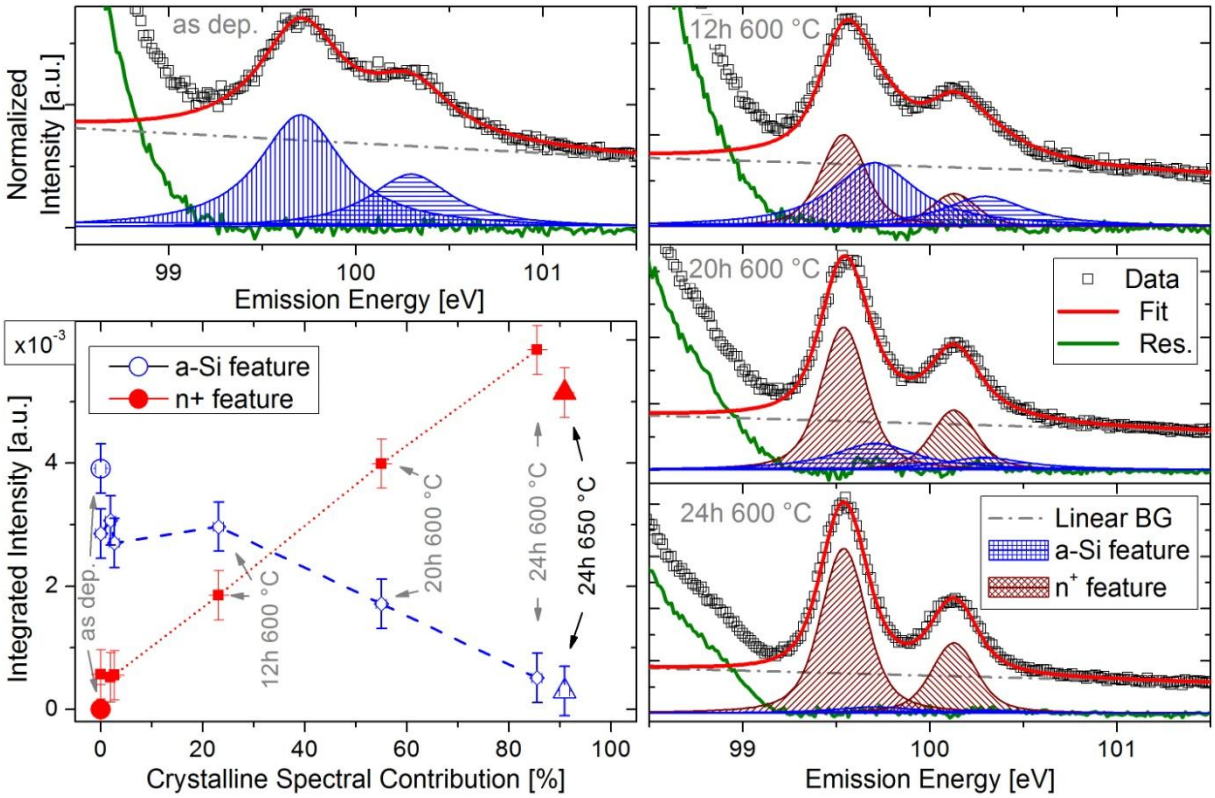

Figure 4.18: Spectra: Coupled Voigt fits of the Si $L_{2,3}$ XES above-VB feature. The as-deposited spectrum was used to determine the parameters of the a-Si related feature (top left). To determine the parameters of the n^+ related feature, the 24 h 600 °C spectrum was fit after subtracting the weighted a-Si related feature (bottom right). Two more fits that include both features with the Voigt intensities as free parameters are shown for the 12 h and 20 h 600 °C samples. Bottom Left: Plot of the integrated L_2 intensity of both features over c-Si contribution (from Figure 4.14). Connecting lines indicate the samples that were heated at 600 °C.

With this procedure, the data can be well described. By plotting the integrated intensity of the L_2 Voigt of each feature over the crystalline spectral contribution, one can observe a linear decline of the a-Si related feature and a linear increase of the n^+ related peak. The n^+ feature intensity can be directly related to crystallinity. This behavior supports the assumption of

having two different contributions: An a-Si related and a n^+ related feature at the given positions with their specific width.

Origins might be occupied defect states in the band gap of a-Si, that disappear upon crystallization and occupied P donor states in the solid-phase crystallized samples. Upon crystallization the defect states would reduce while occupied doping states remain/appear. The increase of the overall feature intensity and especially of the n^+ related feature, however suggests that most of the phosphorous atoms do not act as dopants in a-Si:H(n^+) and get "activated" upon crystallization.

As mentioned in chapter 2.1.1, phosphorous atoms in a-Si:H are incorporated mainly in an energetically favorable but chemical inert (non-doping) threefold configuration [14] and in small fractions in the doping fourfold configuration. This results in a doping efficiency (fraction of P atoms in fourfold configuration) below 1% [18]. Upon crystallization and formation of the lattice structure, P atoms, which are incorporated within the lattice, undergo a transition from threefold to fourfold. This transition would explain an increase of dopant states and might explain the observed increase in the n^+ related feature.

Acceptor states for boron doping should be unoccupied, which might explain the absence of the feature for crystallized p^+ poly-Si samples.

4.4 Impact of substrates

In subchapter 4.2 the influence of dopants on the SPC conversion of a-Si into poly-Si was investigated for films deposited on ZnO:Al/glass substrates. Since the Si/ZnO interface is known to to be the place for chemical reactions and intermixing [110][111][116], the impact of the SPC process on the Si/SiN_x interface is studied in the following. SiN_x is expected to be a barrier to limit species diffusion from the glass substrate into the Si absorber. This type of substrate structure was also used for the current poly-Si world record solar cell [12]. Note that comparable efficiencies with poly-Si on ZnO:Al are not yet reached.

During the n^+ a-Si:H deposition that was described in subchapter 4.2, samples were also deposited onto 100 nm thick SiN_x (deposited via PECVD on Schott Borofloat 33 glass). The samples underwent the identical SPC processes as the ones on ZnO:Al, ranging from 2 h - 24 h at 600 °C and 24 h + 66 h at 650 °C.

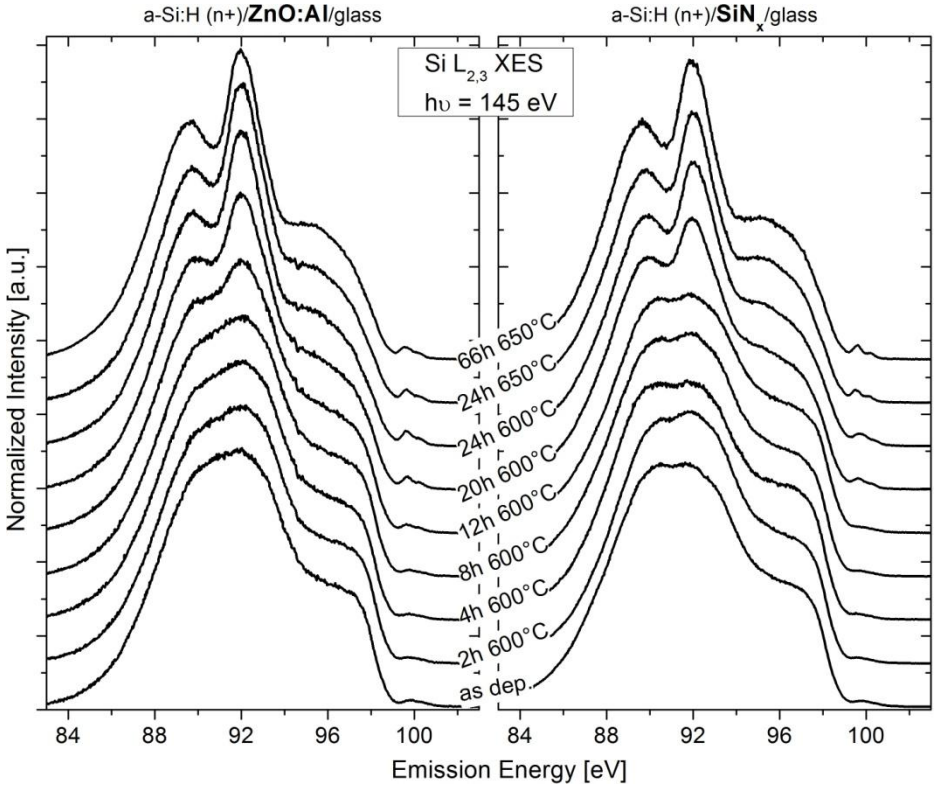

Figure 4.19: Direct comparison of area normalized Si $L_{2,3}$ XES spectra of a-Si:H (n^+)/ZnO:Al/glass (left) and a-Si:H (n^+)/SiN_x/glass (right) samples. Each series includes an as-deposited sample and samples that underwent different SPC processes (2 hours to 24 hours at 600 °C and 24 hours as well as 66 hours at 650 °C).

A direct comparison between Si $L_{2,3}$ XES spectra of a a-Si:H(n^+) SPC time series on ZnO:Al and SiN_x can be seen in Figure 4.19. The as-deposited sample on SiN_x has a higher shoulder at 90.1 eV and the spectra indicate the presence of c-Si later (24 h 600 °C) than on ZnO:Al (20 h 600°C).

Since the thickness of the Si layers (50 nm) is not much thicker than the effective attenuation length (29 nm [80]), it can be expected that the spectra also contain contribution from the SiN_x/glass substrate. Spectra of the bare SiN_x/glass substrate before and after SPC (24 h 650°C) are shown in Figure 4.20 together with spectra of relevant Si-references.

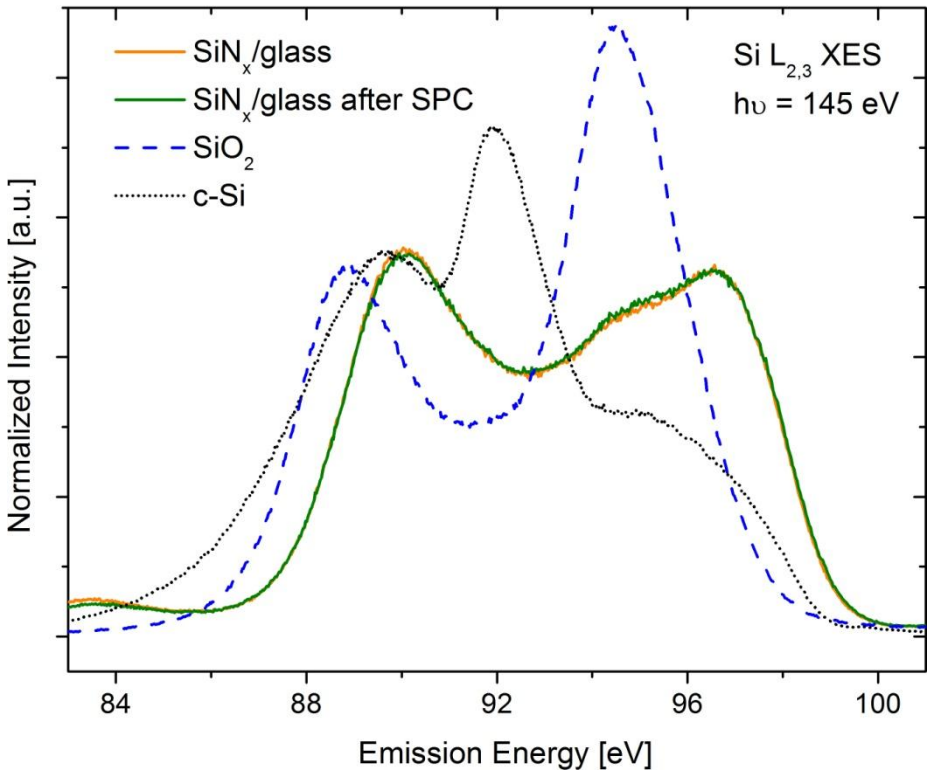

Figure 4.20: Reference Si $L_{2,3}$ XES spectra of a bare SiNx/glass substrate sample before (orange line) and after SPC (24 h 650°C) treatment (green line) compared to that of c-Si (black dotted) and SiO_2 references (blue dashed).

SiN_x Si $L_{2,3}$ XES spectra can be easily distinguished from that of monocrystalline Si and SiO_2. The most distinct feature is an intense shoulder at 97 eV that can be attributed to N 2p π states, while the maximum at 90 eV can be attributed to a mixture of N 2p σ and Si 3 s-p states [117]. A small additional feature at the edge of the measurement window at 83 eV can be observed, that can be attributed to a mixture of N 2p and Si 3s states [118], but since this spectral region is distorted due to the tilted detector (see chapter 3.3), it will not be further analyzed.

SPC thermal treatment (24 h 650 °C) has almost no effect on the spectrum. A small increase at 97 eV is most likely due to the formation of SiO_2. The observed shoulder of the as-deposited a-Si:H (n^+)/SiN_x sample in Figure 4.19 at 90.1 eV can therefore be explained with spectral contribution from the underlying substrate.

In order to quantify the degree of crystallization the approach of spectral superposition used in the previous subchapters was employed again using the spectra of the as-deposited (a-Si) sample, the monocrystalline Si-Wafer, SiO_2 and the bare SiN_x as references (i.e., $I_{sample}=A\cdot I_{a\text{-}Si}+B\cdot I_{c\text{-}Si}+C\cdot I_{SiO_2}+D\cdot I_{SiN_x}$). An example fit and the spectral contributions over SPC time can be seen in Figure 4.21 for the Si thin films on ZnO:Al/glass and SiN_x/glass substrates.

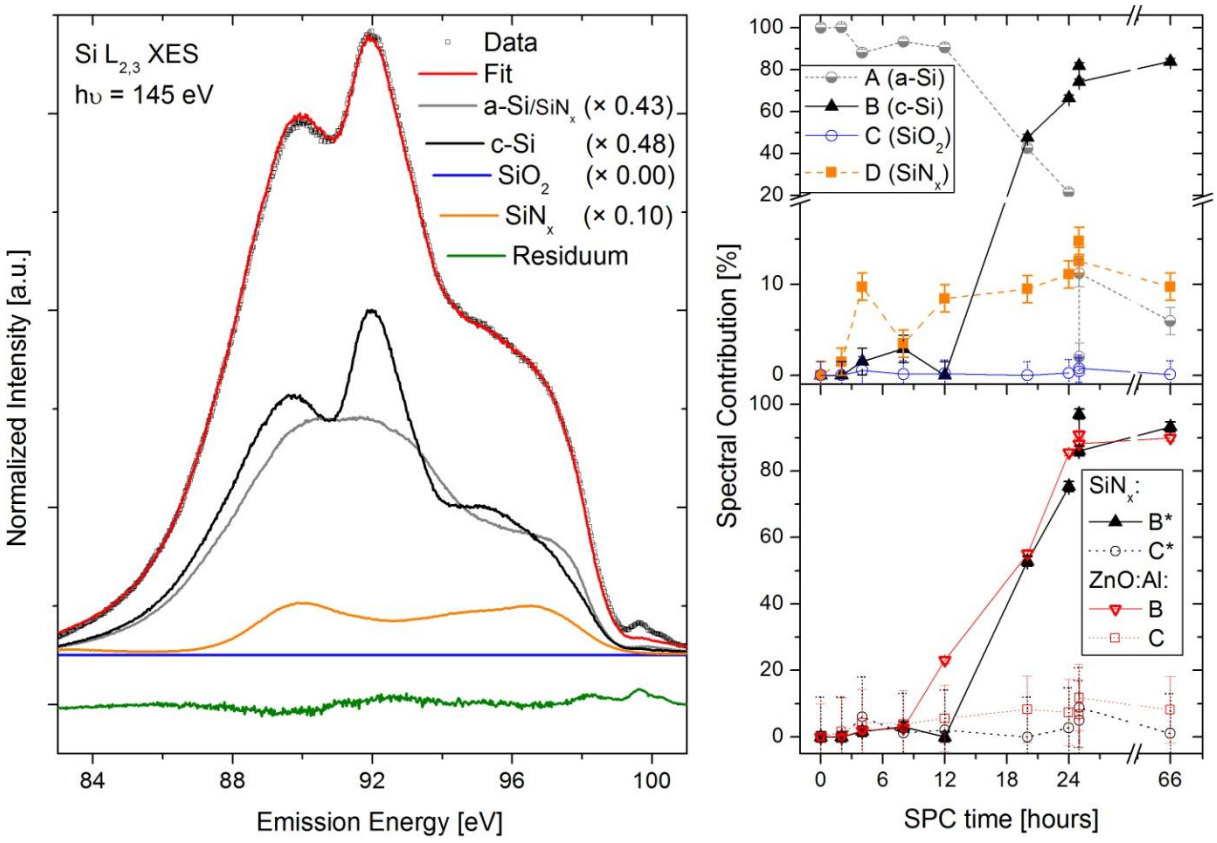

Figure 4.21: Left: Example fit for the Si:H(n^+)/SiN_x sample that underwent 20 h 600 °C heat treatment. Data points (□), the fit (red), weighted references of a-Si (as-deposited sample; gray), c-Si (Si-Wafer; black), SiO_2 (Corning glass; blue) and SiN_x (bare substrate; orange) as well as the residuum (green) are given. Top right: Evolution of the spectral contributions of each sample over SPC time. Bottom right: Comparison of modified c-Si component B* (▲) and modified SiO_2 component C* (○) with B (▼) and C (□) of the ZnO:Al substrate series.

The fit approach represents all the data well when the underlying SiN_x is taken into account (as seen in Figure 4.21). Most spectra contain a SiN_x component D around 10%. SiO_2 contributions never exceed 1% and thus stay below the error bar (±1%).

The high SiN_x contribution, especially for the amorphous-looking spectra (2 h – 12 h 600 °C), is surprising, because the as-deposited reference spectrum should contain roughly the same amount of SiN_x signal (assuming no thickness variations) and thus should lead to underestimation of SiN_x content. An increase with c-Si component is not surprising as the c-Si reference is SiN_x-free. Removing the surface oxide that formed during SPC with HF etching might have thinned the samples, leading to increased signal from the substrate.

To compare the c-Si and SiO_2 components of the a-Si:H/SiN_x series with those of the a-Si:H/ZnO:Al series, modified spectral components B^* and C^* are calculated to account for the additional SiN_x substrate signal (i.e., $B^* = \frac{B}{A+B+C}$, $C^* = \frac{C}{A+B+C}$). This is also shown in Figure 4.21. The direct comparison reveals that the crystallization starts earlier on ZnO:Al (8 h 600 °C) than on SiN_x (12 h 600 °C) and reaches over 80 % c-Si already at 24 h 600 °C. The SiO_2 component of all Si/ZnO:Al samples (except 4 h 600 °C) is higher than for Si/SiN_x, which can be interpreted as another confirmation for the oxidation at the Si/ZnO:Al interface. After 66 h SPC time a similar crystallinity of ~ 90 % is reached on both substrates.

A recent investigation of the crystallization velocities of e-beam evaporated 1 µm thick p^+ type Si:B layers with Raman spectroscopy, optical microscopy and TEM resulted in a start at 15 min (50 min) and a completed crystallization at 4 h (12 h) for samples deposited on ZnO:Al (SiN_x) [119]. The faster crystallization on ZnO:Al substrate therefore seems to be independent of doping.

The reason for the faster onset of crystallization on ZnO:Al might be diffusing Al since Al is known to decrease the time and temperature needed for SPC [120]. As being an ($n_{valence}$-1) impurity aluminum in silicon (similar to B) may cause the same effect in a-Si, i.e. increasing the crystallization rate. Evidence for SPC induced Al diffusion from the ZnO:Al substrate into silicon has been found recently as a result of our groups hard x-ray photoemission spectroscopy (HAXPES) studies [116]. The effect of chemical interactions at the buried Si/ZnO:Al interface will be discussed further in chapter 5.

5. Chemical structure of the Si/ZnO:Al interface

This chapter is dedicated to the investigation of the chemical and the electronic structure of the buried Si/ZnO:Al contact.

Post-deposition heat treatment steps of the a-Si/ZnO:Al/glass layer stack to form polycrystalline silicon are expected to result in species interdiffusion across and chemical reactions at the interface. This could limit the efficiency of the respective solar cells. Therefore these effects are investigated in subchapter 5.1.

Subchapter 5.2 discusses the effect of hydrogen on Si $L_{2,3}$ XES spectra and tries to clarify which spectral features that are observed in chapter 4.2, 4.4 and 5.1 can be related to H and which could be attributed to the buried Si/ZnO:Al interface.

5.1 Impact of solid phase crystallization on the Si/ZnO:Al interface

In order to reveal the influences of SPC on the buried Si/ZnO:Al interface, two approaches are taken in this subchapter: First Si $L_{2,3}$ XES spectra of an a-Si:H(n^+) thickness series on ZnO:Al/glass is compared to spectra of an a-Si:H(n^+) thickness series on SiN_x/glass substrates before and after SPC. From the results of this comparison, an attempt on identifying potentially formed interface species is made by measuring additional reference spectra. Second a poly-Si/ZnO:Al sample is investigated by photoelectron emission microscopy (PEEM). By mechanically removing the poly-Si cover layer in specific areas, chemical information can be gained from the interface and the poly-Si cover layer at the same time.

5.1.1 Si thickness series investigated with XES

Thickness series of phosphorous doped a-Si:H(n^+) were grown by PECVD on ZnO:Al/glass and SiN_x/glass substrates and examined via Si $L_{2,3}$ XES. Deposition parameters and substrates were the same as stated in chapter 4.2 and 4.4. By varying the a-Si:H(n^+) deposition time, layers from 5 nm to 300 nm thickness were grown. Thickness values were determined by ellipsometry measurements of reference layers deposited on Si-wafers that were positioned next to the glass substrates during deposition. To limit surface contamination and oxidization, half of the samples were sealed in nitrogen directly after deposition; the other half underwent SPC (24 hours at 650 °C). As the samples on SiN_x/glass and ZnO:Al/glass were deposited on a different PECVD run, their thicknesses differ slightly. Before performing the XES measurements, all samples were HF-etched (30 s 5% HF) to remove the surface oxide.

The recorded Si $L_{2,3}$ XES spectra for both thickness series on ZnO:Al/glass and SiN_x/glass substrate are plotted in Figure 5.1 together with the determined thicknesses.

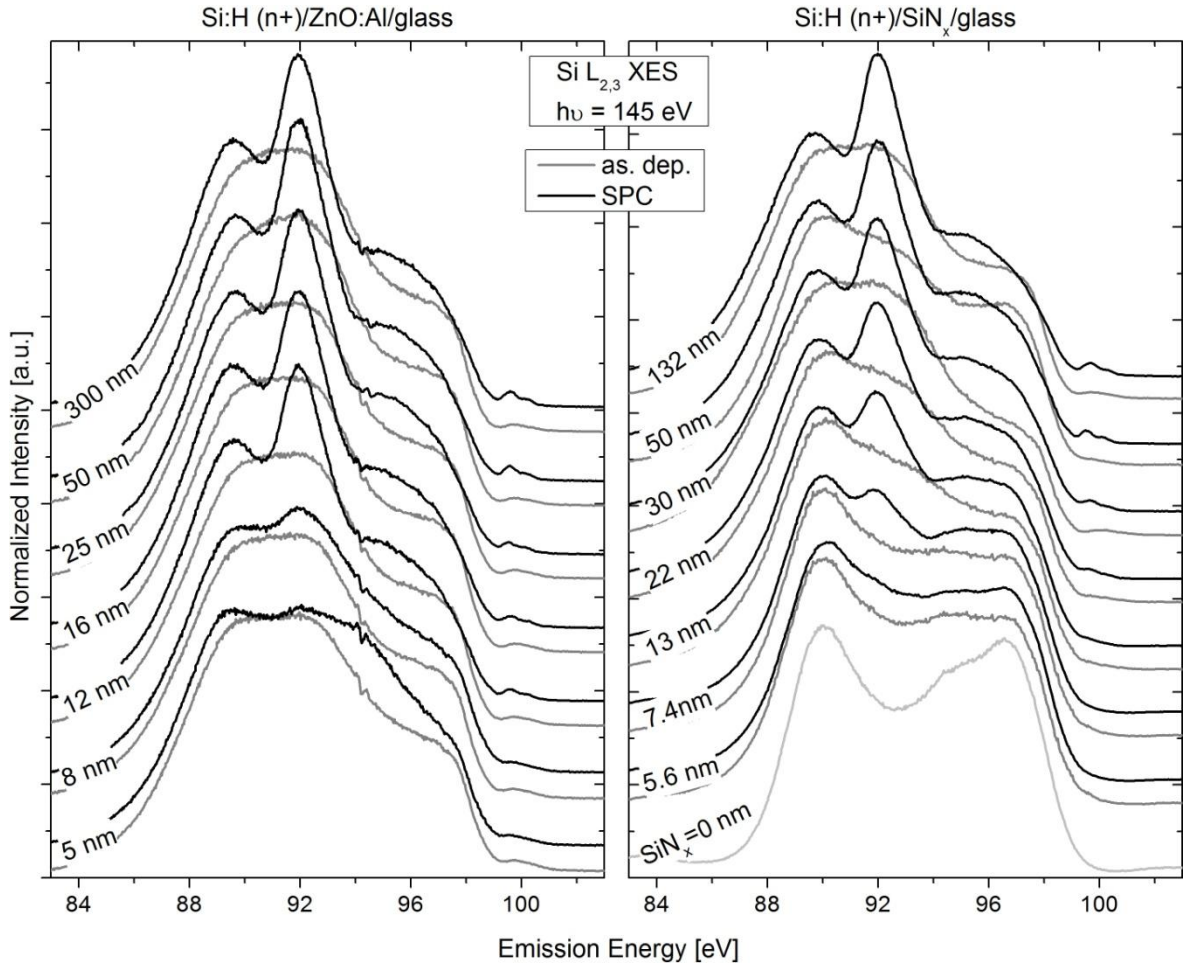

Figure 5.1: Area normalized Si $L_{2,3}$ XES spectra of a-Si:H (n^+) on ZnO:Al/glass (left) and SiN_x/glass (right) with varying thicknesses before (gray) and after SPC (black). For comparison, the bare SiN_x substrate is shown on the right side. Determined thickness values are given.

On ZnO:Al/glass substrate, the spectra of the as-deposited samples of all thicknesses look similar – like amorphous silicon. The two thinnest samples (5 nm and 8 nm) appear broader than the thicker ones; the maximum at 92 eV is less, and the shoulder at 98 eV is more intense. After SPC, the spectra of these thin samples do not change much from the a-Si shape, but develop an additional shoulder at 94 eV and only a small maximum at 92 eV. The spectra of the thin samples on SiN_x substrates are dominated by the substrate signal. Therefore only a minor impact of SPC can be observed for the thin 5.6 nm sample.

Similar to the evaluation of Si $L_{2,3}$ XES spectra in chapter 4.1, the measurements were approximated by a least-square fit with weighted reference spectra [300 nm a-Si:H(n^+)/ZnO:Al (“a-Si”), 300 nm poly-Si:H(n^+)/ZnO:Al (“poly-Si”) and Corning glass (“SiO_2”) for the spectra of the Si thin films on ZnO:Al; 132 nm a-Si:H(n^+)/SiN_x (“a-Si”),

132 nm poly-Si:H(n^+)/SiN_x (“poly-Si”), SiO_2 and the bare SiN_x substrate for the spectra of the Si thin films on SiN_x].

All spectra of the Si samples above 8 nm thickness are well represented by the superposition of these weighted references, as indicated by the fits in Figure 5.2. For thinner as-deposited and SPC treated samples on ZnO:Al the residua, however show a significant intensity at 98 eV.

The evolution of the spectral contributions (i.e., $I_{sample}=A\cdot I_{a\text{-}Si}+B\cdot I_{poli\text{-}Si}+C\cdot I_{SiO_2}+D\cdot I_{SiN_x}$) of all fits are shown in Figure 5.3. Due to the x-ray attenuation of the cover layer the SiN_x contribution D follows an exponential decay with increasing cover layer thickness. In order to compare the two different substrates, D is excluded by calculating the relative contributions for a-Si:H (A*), poly-Si (B*) and SiO_2 (C*) [i.e., $A^*=\frac{A}{A+B+C}$]. The respective error bars are computed accordingly.

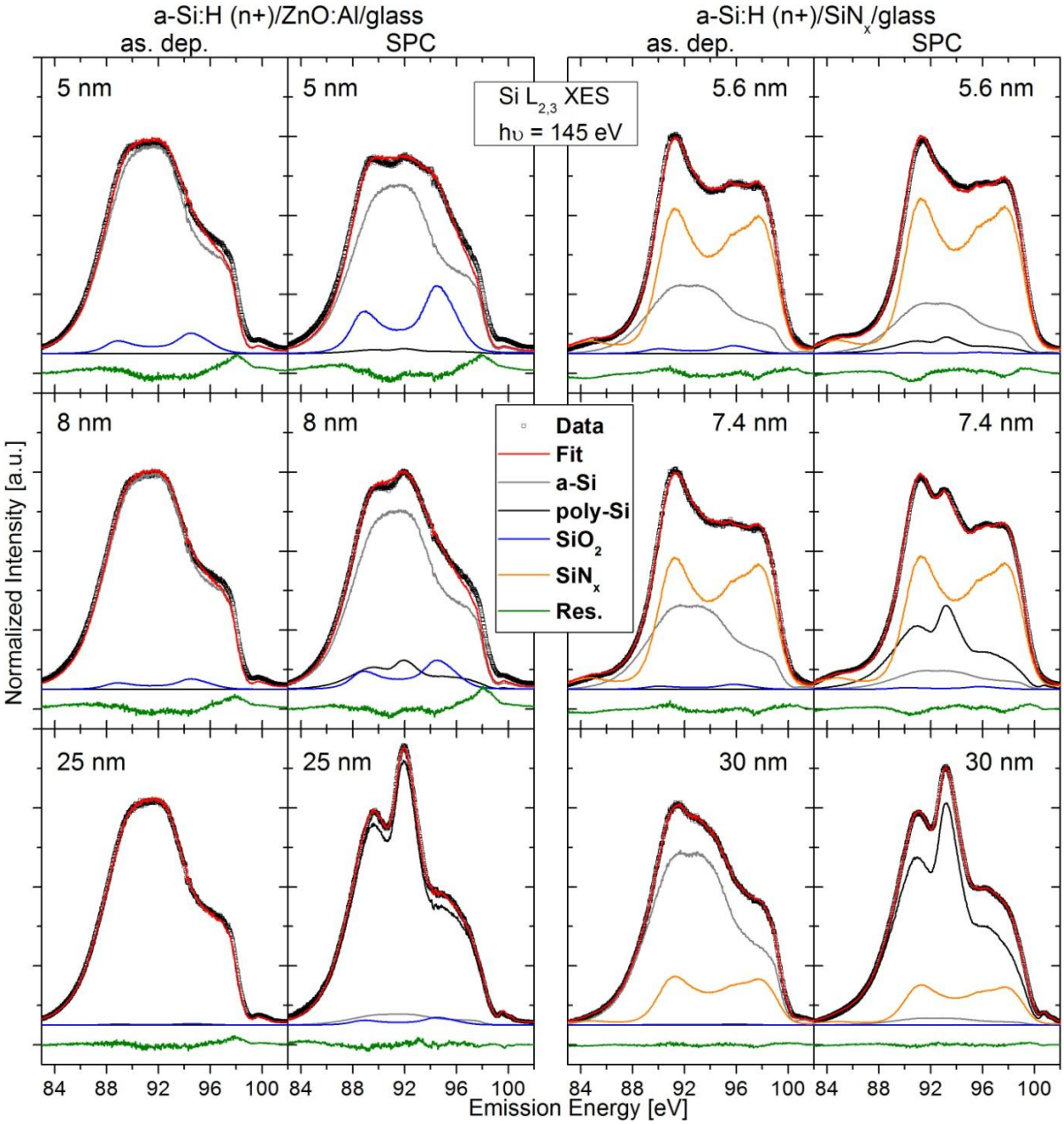

Figure 5.2: Example fits (red) of the Si $L_{2,3}$ XES spectra for selected spectra of the a-Si:H (n^+) thickness series on ZnO:Al (left) and SiN_x substrates (right) before and after SPC. Weighted references of a-Si (grey), poly-Si (black), SiO_2 (blue) and SiN_x (orange) are given and the respective residua are shown in green.

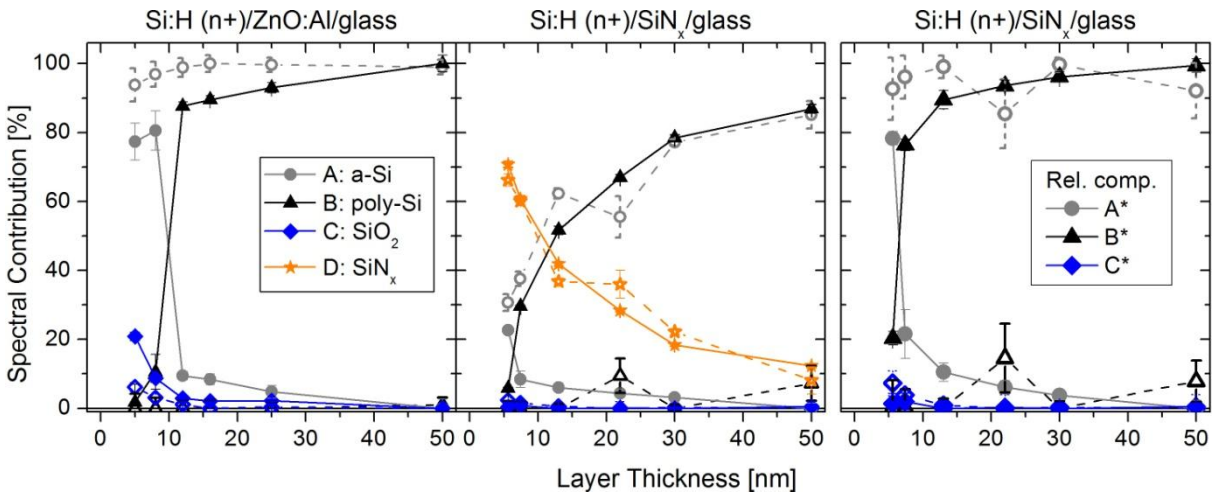

Figure 5.3: Evolution of the a-Si (●), poly-Si (▲), SiO_2 (◆) and SiN_x (★) spectral contributions to the Si $L_{2,3}$ XES spectra of the two thickness series on ZnO:Al (left) and SiN_x substrate before (hollow symbols, dashed lines) and after SPC (filled symbols, solid lines). For the SiN_x substrate the absolute contribution (center) and the relative contributions - without SiN_x contribution - (right) are shown.

Significant SiO_2 contributions are found for the thin as-deposited samples (5 nm and 5.6 nm) on both substrates of C = C* = 7 % declining with increasing Si layer thickness. Upon SPC, C increases to 20 % for the 5 nm ZnO:Al sample but C* remains within the error bar at the same value as the as-deposited sample. This again confirms the oxidation at the Si/ZnO:Al interface upon SPC. In both series, the spectra of the thinnest samples after SPC are still dominated by an a-Si contribution [(78 ± 4) %]. Please note that there are two outliers for the as-deposited samples on SiN_x [22 nm and 50 nm]. They were measured at a different date without the a-Si and poly-Si reference – resulting in a slightly different spectral shape and therefore an unsatisfying fit.

The high a-Si contribution of the samples below 10 nm might be due to the fact that the small layer thickness hinders the evolution of larger grains. Additionally, the previously suggested a-Si signal from the distorted lattice on top of the grains would contribute more to the spectrum for thin layers in this size range as compared to thick films (see discussion in chapter 4.1). SPC induced interface oxidization is further confirmed due to the increase in the SiO_2 contribution upon SPC of thin samples which only occurs on ZnO:Al and not on SiN_x.

The residuum intensity at 98 eV observed for the thin samples on ZnO:Al may indicate an additional interface species. Therefore, several possible candidates were measured and compared. Most readily available were zinc silicate (Zn_2SiO_4) and aluminum silicate

($Al_2(SiO_3)_3$). But the spectral shapes looks very similar to SiO_2 and thus do not explain the additional spectral weight at 98 eV, as shown in Figure 5.4 .

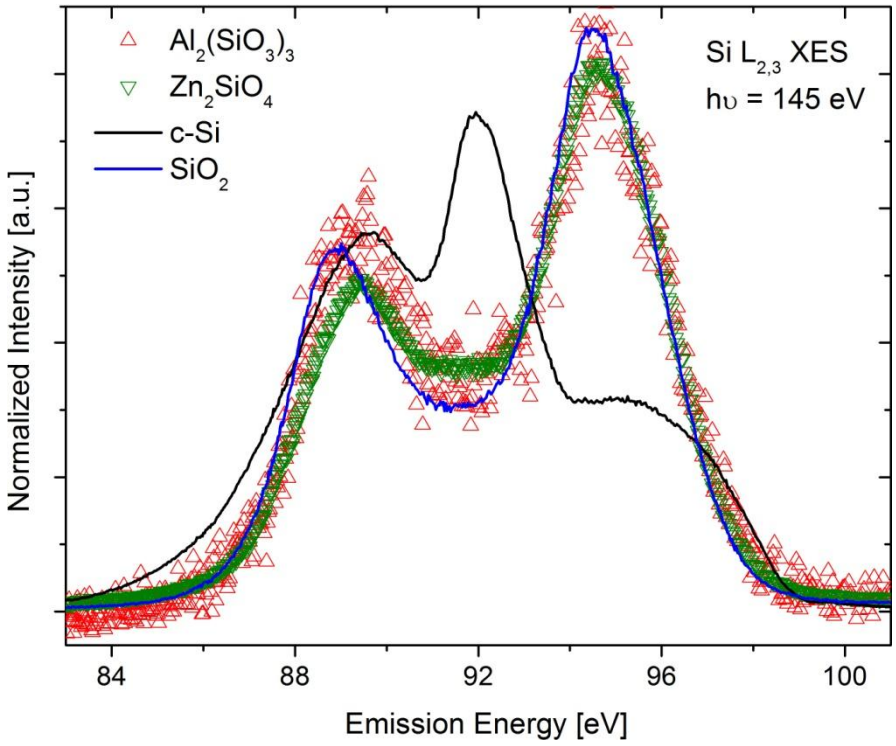

Figure 5.4: Reference Si $L_{2,3}$ XES spectra of silicate powders [$Al_2(SiO_3)_3$ (△) and Zn_2SiO_4 (△)] compared to spectra of c-Si (black line) and SiO_2 (blue line).

Using Zn_2SiO_4 as an additional reference for fitting, together with the other references stated above, does not result in a better fit and the spectral component of Zn_2SiO_4 is far below the error bar. Silicides as another possibly formed material class containing Zn or Al were not available or do not exist.

[In the course to indentify the surface species with reference spectra, non stoichiometric SiO_x compounds were also investigated. These were fabricated by PECVD of SiH_4/N_2O precursors with varying gas ratios. Samples were provided by Maurizio Roczen of HZB. Si $L_{2,3}$ XES spectra looked very similar to these of thin a-Si and poly-Si layers on ZnO:Al and showed a high intensity at 98 eV. But by doing the above described fitting procedure, it was found out that 98 eV contributions in these samples is most likely due to an SiN_x component from the N_2O precursor (not shown).]

In conclusion, the examination of the thickness series with Si $L_{2,3}$ XES confirms the oxidization at the buried Si/ZnO:Al interface. Reference Si $L_{2,3}$ XES spectra of possible interface species like zinc silicate and aluminum silicate resemble those of SiO_2, so the

formation of these species cannot be excluded. A superposition approach of the thin Si samples on ZnO:Al/glass substrates resulted in a significant residuum at 98 eV that could not be explained in this context. A more detailed discussion on the origin of this spectral feature will be given in subchapter 5.2, where the influence of hydrogen passivation will also be considered.

5.1.2 Investigation with X-PEEM

The impact of crystallization on the buried interface was investigated further with x-ray photoemission spectroscopy (X-PEEM). Because of the higher surface sensitivity of this method (compared to x-ray emission spectroscopy (XES) and hard x-ray photoelectron spectroscopy HAXPES), a thin 5 nm poly-Si:H (n^+)/ZnO:Al/glass sample was used and further modified by mechanically removing (carving lines into) the poly-Si cover layer to expose the substrate. After that the samples were HF etched (10 s 0.5 % HF) to remove the surface oxide.

After introduction into the X-PEEM system, a sample area was chosen that contained both the exposed ZnO:Al bottom and an intact poly-Si cover layer. This region is shown in the secondary electron image shown in Figure 5.5. The size of the shown area is limited by the electron optics, resulting in a image size or field of view (FOV) of 10 µm.

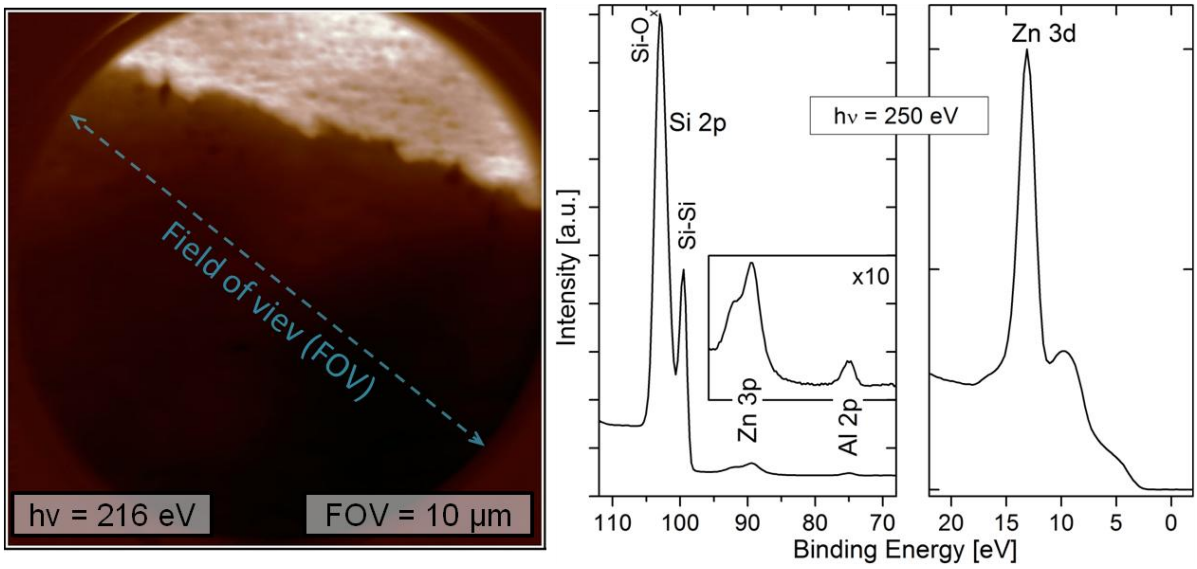

Figure 5.5: Left: Secondary electron image of the 5 nm poli-Si (n^+)/ZnO:Al sample. The field of view (FOV) is 10 µm and the excitation energy is 216 eV. Right: XPS spectra of this sample taken at 250 eV excitation energy (with an inset magnifying on the Zn 3p and Al 2p peaks).

The exposed area on the top right of the image appears bright and the rest dark, which is due to the lower work function of ZnO:Al compared to poly-Si. (High Al doping: 3.5 eV [121]; Si-Wafer: 4.5…4.9 eV [113]). Integrating XPS spectra (recorded in dispersive plane mode) reveals two Si species that can be ascribed to Si-Si and Si-O_x bonds for Si 2p [122], a Zn 3p peak with a shoulder due to the spin-orbit split: 2.9 eV for ZnO between Zn $3p_{1/2}$ and Zn $3p_{3/2}$ [123] (the 0.6 eV spin orbit split for Si 2p [112] cannot be resolved in this mode), a Zn 3d and a Al 2p photoemission line. Note that the later is due to the Al dopant of the ZnO:Al.

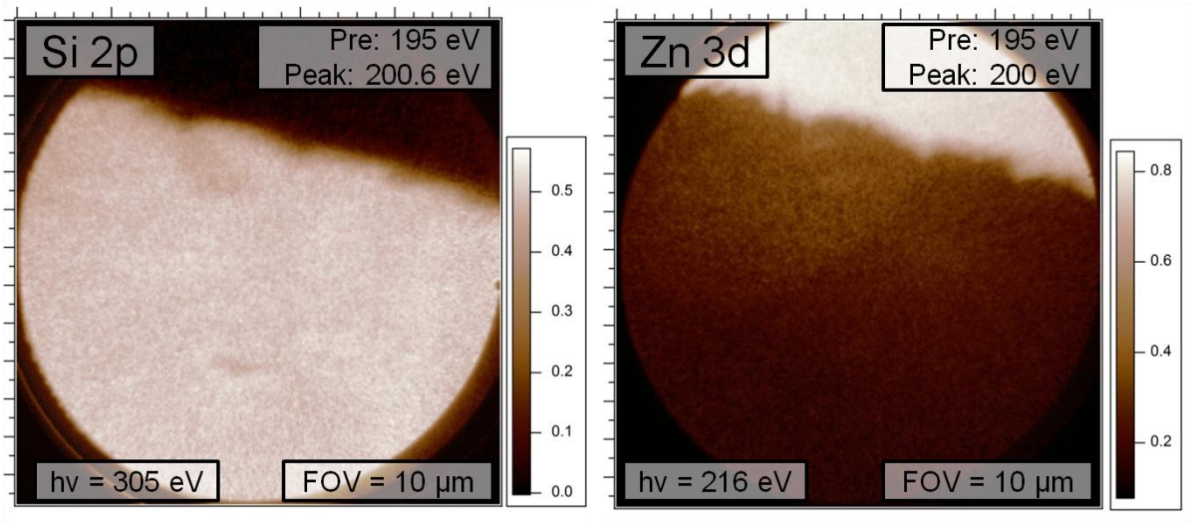

Figure 5.6: X-PEEM Si2p images measured at 200.6 eV for Si 2p (left) and at 200 eV for Zn 3d (right) using excitation energies of 305 eV (left) and 216 eV (right).

By taking multiple images with the energy filter set to a kinetic energy corresponsive to a photoemission line (peak), chemical sensitive maps are recorded. To account for the secondary emission background, these images are subtracted by images recorded at a slightly lower kinetic energy (pre). Such X-PEEM maps are shown in Figure 5.6 for Si 2p and Zn 3d. They appear inverted and in both images a distinctive edge divides bright and dark areas. Except from the top area of the map, a mostly uniform Si cover layer can be observed in the Si 2p map. Darker specks are most likely due to contamination on the surface or topography as they do not show up as bright spots in the Zn 3d map. Although the noise-level is high, a non-vanishing Si 2p (Zn 3d) signal can be observed in the exposed areas (in the Si-covered area) adjacent to the edge. This is surprising because the 5 nm thick poly-Si layer should be thick enough to attenuate most (99.8 %) of the Zn 3d signal due to the low IMFP at the excitation energy used here (0.8 nm [65]).

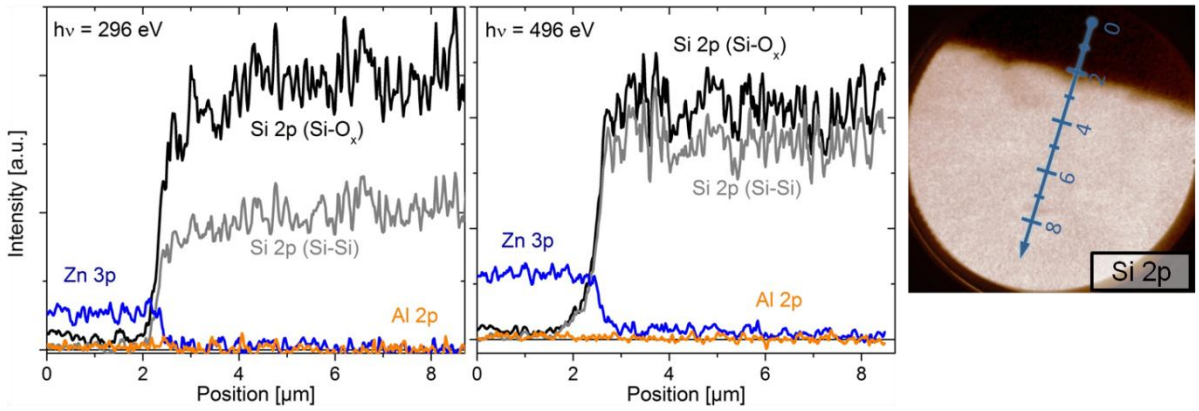

Figure 5.7: X-PEEM line scans: Intensity of the Si 2p (Si-Si), Si 2p (Si-O_x), Zn 3p and Al 2p photoemission lines along the arrow that is indicated in the Si 2p X-PEEM image (right). Excitation energies were 296 eV (left) and 496 eV (center).

Shown in Figure 5.7 is the peak intensity of the Si 2p (Si-Si), Si 2p (Si-O_x), Zn 3p and Al 2p line along the direction that is indicated in the Si 2p X-PEEM image, measured at two different excitation energies. As indicated by the arrow, the 0 µm position is directly in the exposed (bare ZnO:Al) area and the edge is roughly positioned at 2 µm. The peak intensities were integrated over a width of about 2 µm. When comparing the intensities of the 296 eV and the 496 eV line scans, a decrease in Si 2p (Si-O_x) to Si 2p (Si-Si) ratio and an increase in overall Zn 3p is noticeable. The Si 2p ratio change is indicative of Si surface oxidation due to the higher information depth at 496 eV [65] and the relative Zn 3p gain is most likely due to an increase in the respective photoionization cross sections relative to that of Si 2p with increasing excitation energy (i.e., $\frac{\sigma_{\text{Zn 3p, 300 eV}}}{\sigma_{\text{Si 2p, 300 eV}}} = \frac{0.65}{1.13} \approx 0.58$ and $\frac{\sigma_{\text{Zn 3p, 600 eV}}}{\sigma_{\text{Si 2p, 600 eV}}} = \frac{0.25}{0.18} \approx 1.39$ [124]).

The intensity of Al 2p is close to the noise level. Note that low intensities of Si 2p are detected in the exposed areas and small amounts of Zn are present in the covered area – which, besides the trivial explanation of material residues/cross contamination due to mechanical scribing, might indicate chemical interaction or diffusion.

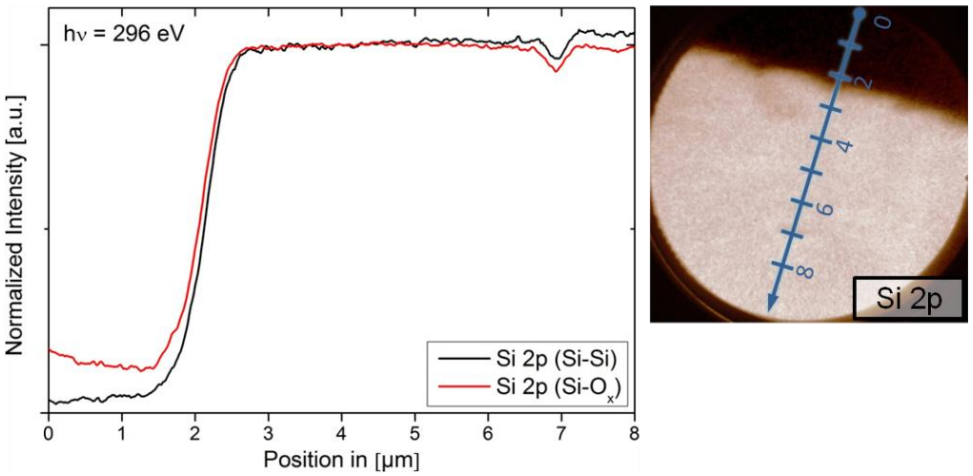

Figure 5.8: Line scans of Si 2p (Si-Si) and Si 2p (Si-O_x) along the arrow that is indicated in the Si 2p X-PEEM map. For direct comparison, the intensity is normalized to 1 at the 4 µm position.

To investigate this in more detail, longer X-PEEM measurements of the Si 2p lines were performed. Resulting Si 2p line scans with better statistics are shown in figure Figure 5.8. They reveal a comparatively high Si-O_x signal intensity in the exposed ZnO:Al area. The decrease at position 7 µm correlates with a small spot with less brightness in the Si 2p image (also seen in Figure 5.7 between 7 and 8 µm), which is most likely localized surface contamination.

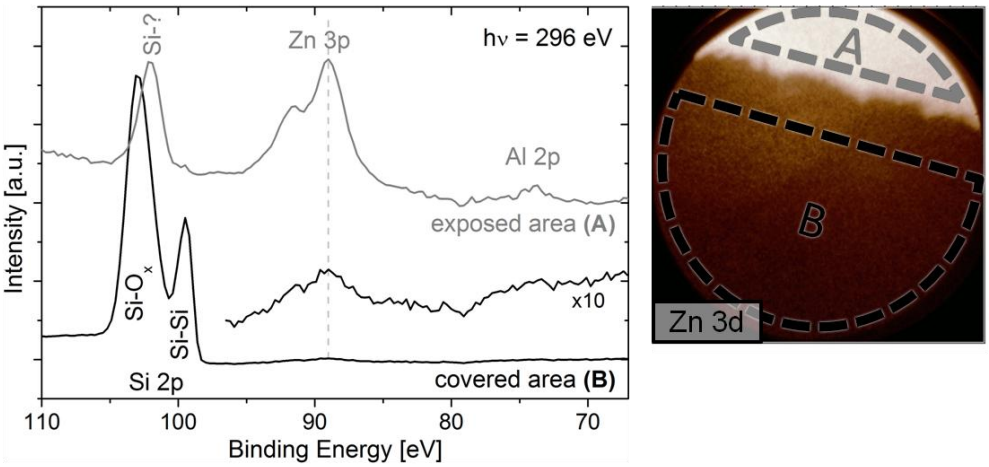

Figure 5.9: Right: Local XPS spectra of the Si-covered (A) and the exposed regions (B). The Zn 3p and Al 2p region of the covered area is additionally magnified. Left: Areas A and B that were used for the integration of the local XPS spectra are indicated in the Zn 3d X-PEEM image.

Local XPS spectra of the exposed and the covered area are illustrated in Figure 5.9. As expected, the spectra of the covered area (B) mainly consist of the Si 2p (Si-Si) and (Si-O_x) peaks, with a minor (attenuated) contribution of Zn 3p, while the exposed area (A) shows a higher Zn 3p intensity.

The Si 2p intensity is not only higher than expected from the line scans in Figure 5.8 but consists only of a single peak at (102.1 ± 0.3) eV instead of the two peaks at (99.5 ± 0.3) eV [Si-Si] and (102.8 ± 0.3) eV [Si-O_x] for (B) (Literature values of Si 2p: Si-Wafer: 99.3 eV; SiO_2: 103.3 eV [125]). The Si 2p intensities of the line scans in the exposed ZnO:Al area were therefore underestimated because they were measured at fixed energies at the Si-O_x and the Si-Si position.

The chemical shift of the Si 2p line to (102.1 ± 0.3) eV, that is measured at the exposed area is in agreement with multiple species according to the NIST XPS database: SiO_x (102 eV), Zn_2SiO_4 (102.4 eV), Si_3N_4 (102 eV) and SiC (102.4 eV) [122]. The formation of carbides and nitrides especially at the interface is very unlikely – N_2 gas is present during SPC but inert. Prior PECVD deposition the samples were chemically cleaned – so a C source should also be absent.

A shift of the Si-O_x line might be induced by band bending but in this case, the Zn 3p line is supposed to shift, too. This cannot be observed in Figure 5.9.

Judging from the results of the thickness series investigated with Si $L_{2,3}$ XES and the X-PEEM results, silicon sub-oxides and zinc silicate are both candidates for a possible interface species. But zinc silicate does not explain the feature in the residuum at 98 eV and the influence of sub-oxides onto Si $L_{2,3}$ XES spectra is currently unclear and needs further investigation.

In conclusion both XES and PEEM investigations indicate a formation of silicon oxides at the interface of poly-Si/ZnO:Al upon SPC. Studies by our group with XES [110] and HAXPES [111] have also shown interface oxidization. In this context it was recently discovered that Zn and Al diffuses into poly-Si during SPC [116], which might coincide with the oxidation process.

5.2 Relation of the 98 eV Si$L_{2,3}$ XES feature to hydrogen

The discussed residua when presenting the Si $L_{2,3}$ XES spectra of thin Si layers on ZnO:Al as a superposition of a-Si, poly-Si, and SiO_2 in previous chapters exhibited a common peak at 98 eV. This subchapter tries to uncover the underlying reason by evaluating the intensity of this feature and comparing this to a different amount of H present in the silicon film by annealing a-Si:H below the crystallization temperature and after poly-Si hydrogen passivation.

In a first experiment, a 50 nm a-Si:H/ZnO:Al/glass sample was annealed 4 hours at 400 °C in air to reduce the amount of hydrogen [126]. After HF etching (30 s in 0.5 % HF in H_2O solution) Si $L_{2,3}$ XES spectra of the as-deposited and the annealed sample were measured. The spectra were measured with normal resolution (10° detector angle) and higher resolution (0° angle, VB onset only) and are shown together with their difference ("annealed" - "as-deposited") in Figure 5.10.

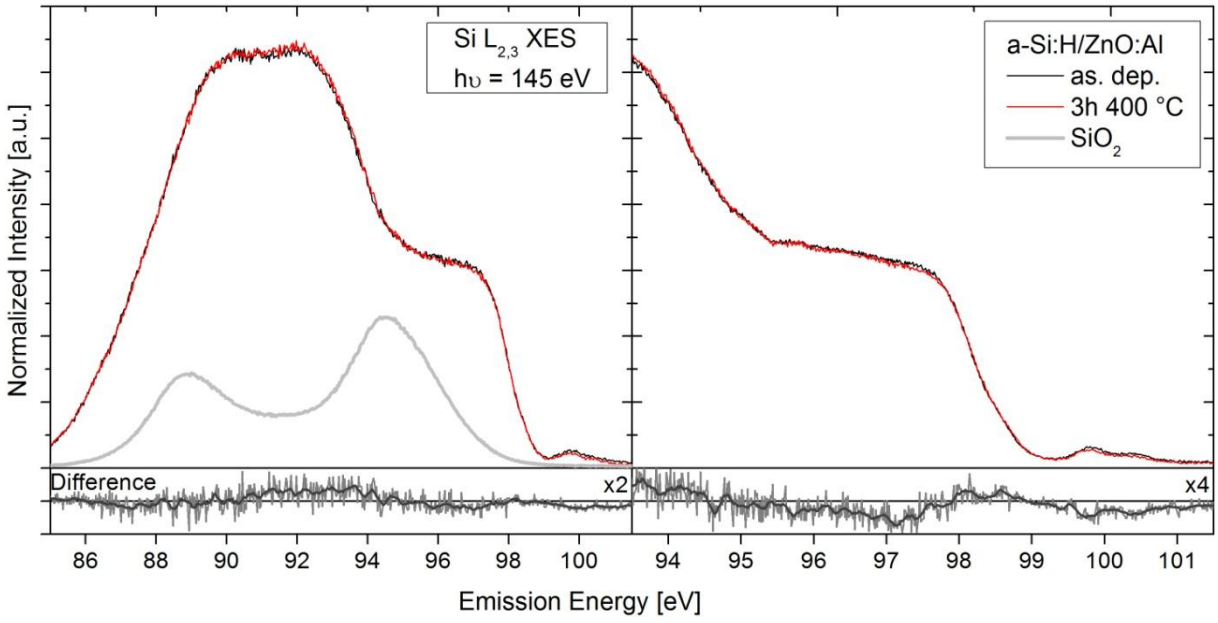

Figure 5.10: Si $L_{2,3}$ XES spectra (regular [left] and high resolution [right]) of a 50 nm a-Si:H sample on ZnO:Al/glass before (black) and after annealing at 400 °C for 4 hours (red). Magnified difference spectra (annealed – as deposited) are shown in the bottom part in grey (thick: 20 point smooth). For comparison a scaled down SiO_2 reference is shown (not measured at the same run – hence the energy might be shifted).

The spectra look almost identical before and after annealing. However, a detailed analysis by (smoothed) difference spectra (annealed - as-deposited) reveals changes upon annealing. The difference shows a decrease at 89 eV, 96 eV and 100 eV, as well as an increase around 92 eV and 98 eV. The changes at 89 eV, 92 eV and 96 eV may be due to a slightly different SiO_2 content. The intensity decrease of the a-Si related feature above the valence band maximum at 100 eV (compare chapter 4.2) was also observed in the SPC time series after the first heating step (see Figure 4.17 and Figure 4.18).

In a second experiment, poly-Si samples before and after hydrogen passivation (HP) were measured. 50 nm thick intrinsic and n^+ doped poly-Si layers on ZnO:Al substrate (the same deposition as described in chapter 4.2) that underwent SPC (24 h 650°C) and rapid thermal annealing (RTP) are compared before and after hydrogen passivation (HP). Si $L_{2,3}$ XES spectra are shown in Figure 5.11 together with a magnified difference (before HP – after HP).

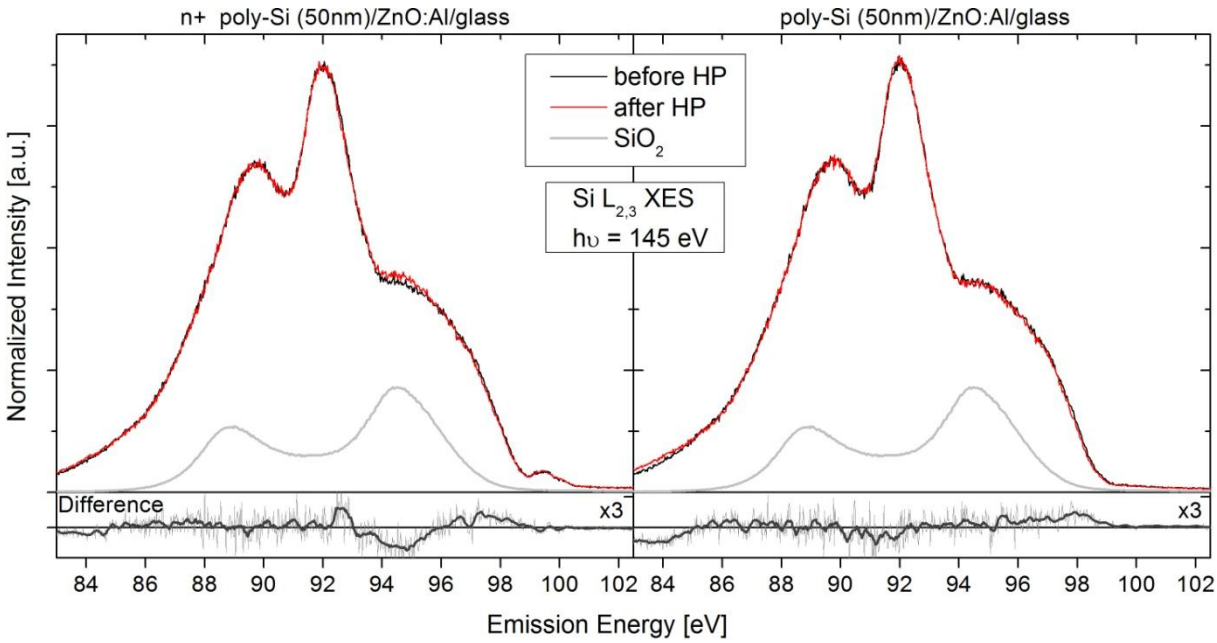

Figure 5.11: Si $L_{2,3}$ XES spectra of 50 nm thick poly-Si samples on ZnO:Al/glass (left: n^+; right: intrinsic) that underwent SPC and RTP treatment before (black) and after hydrogen passivation (HP, red). Magnified difference spectra (before HP – after HP) are shown underneath in grey (thick: 20 point smooth).). For comparison a scaled down SiO_2 reference is shown (not measured at the same run).

The spectral difference of the poly-Si n^+ spectra exhibits the lowest intensity at 95 eV, which could again be ascribed to differing SiO_2 content. In a similar way the minimal difference for the intrinsic samples at 92 eV could be explained with more SiO_2 after HP. These small fluctuations in the SiO_2 are not necessarily related to HP but are more likely due to slightly a different HF etching efficiency.

The dominant remaining difference is located at 98 eV and although it is small, the fact that it is observable for both (intrinsic and n^+) might indicate that it is significant and further can be related to the HP process. The increase of the contribution at 98 eV upon heating of hydrogenated a-Si and the decrease upon hydrogen passivation of poly-Si could mean that the 98 eV contributions could be related to defect states in silicon that can be passivated with hydrogen.

In order to determine if the residual feature at 98 eV from the fits in chapter 4.2 and 5.1 could be attributed to the same origin, the intensity of these features is plotted in Figure 5.12 for the SPC time series and in Figure 5.13 for the thickness series on ZnO:Al as a function of a-Si contribution. A respective evaluation of a sample series deposited on SiN_x is problematic as the substrate reference adds a Si-N contribution at 98 eV (see Figure 4.20).

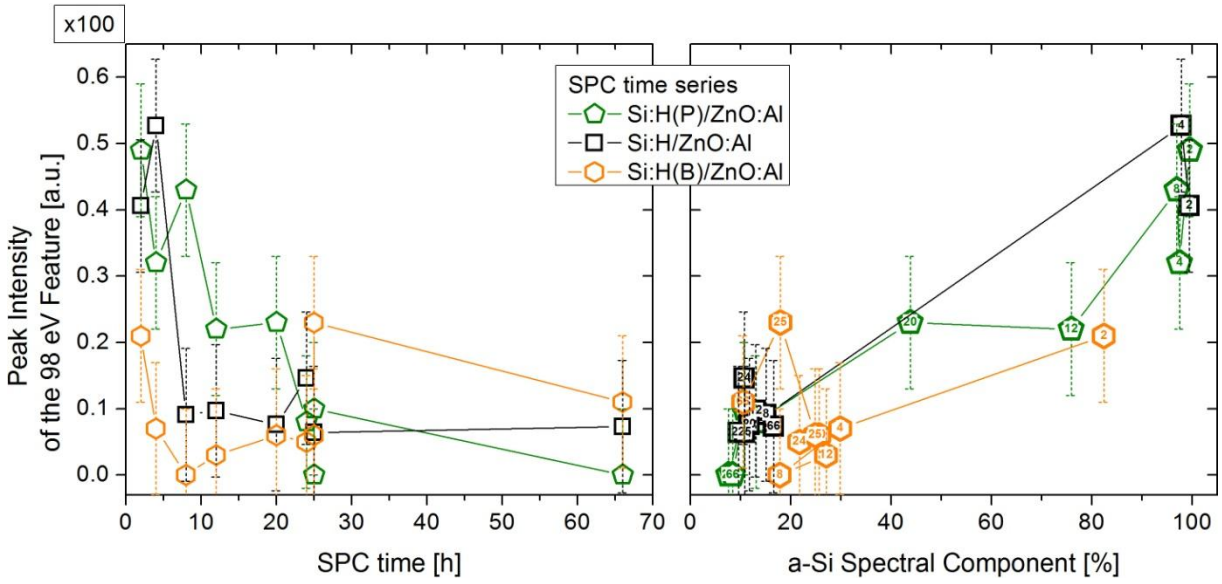

Figure 5.12: Peak intensity of the 98 eV feature in the residuum of the fits for the SPC time series on ZnO:Al over SPC time (left) and as a function of a-Si spectral component (right) shown for Intrinsic (■), n^+ (⬟) and p^+ (⬢) doping. Numbers in the data points indicate the respective SPC time.

Despite quite some scatter for all three SPC time series (n^+, intrinsic and p^+) a decrease of the 98 eV feature with SPC time is noticeable. Plotting the feature intensity over the a-Si spectral component even suggests a linear dependence. Please note that the reference for the a-Si component is the as-deposited 50 nm thick a-Si:H/ZnO:Al sample with the respective doping. Therefore the 98 eV feature appears during the initial heating step (2 h 650 °C) and then gradually disappears as the samples crystallizes. This indicates that the feature is indeed related to defects states in amorphous silicon – which are "healed" as the samples crystallize. The nature of the defect states may change between the as-deposited sample (used as the a-Si reference in all fits) and the a-Si still present in the annealed samples (i.e., the defects are modified at a temperature below the SPC temperature).

A further plot of the 98 eV feature intensity over thickness and as a function of a-Si spectral component for the thickness series of n^+ a-Si:H/ZnO:Al samples as-deposited and after SPC is shown in Figure 5.13.

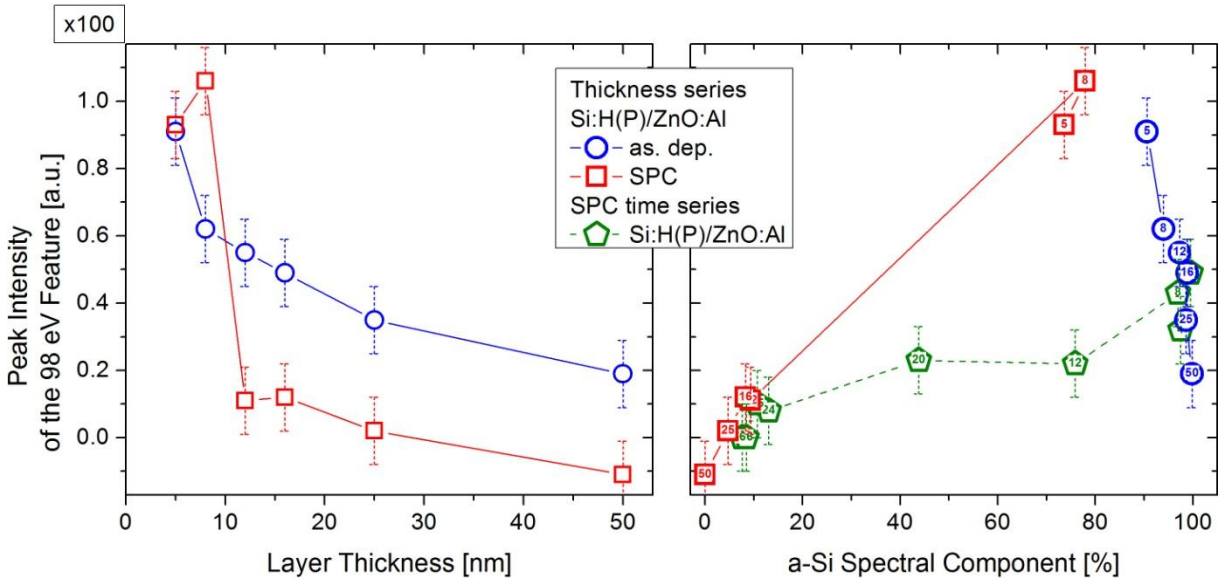

Figure 5.13: Peak intensity of the 98 eV feature in the residuum of the fits for the thickness series on ZnO:Al over thickness (left) and as a function of a-Si spectral component (right) shown before (○) and after SPC (□). Numbers in the data points indicate the respective thickness. For comparison the values of the n^+ SPC series (⬟, from Figure 5.12) is also plotted.

A decrease of the intensity with the layer thickness for the as-deposited samples and thick samples after SPC can be observed. Upon SPC the intensity decreases drastically except for the 5 nm and the 8 nm thin samples, where it even increases. When plotting the intensity over a-Si spectral component similar intensities are found for the samples thicker than 8nm and the respective samples from the SPC series ($I^{98\,eV}_{a.d.;\,thick} \approx I^{98\,eV}_{2..8\,h;SPC}$; $I^{98\,eV}_{SPC;\,thick} \approx I^{98\,eV}_{24..66\,h;SPC}$).

But much higher intensities are observed for the two thin as-deposited samples which even increase upon SPC while the a-Si component decreases. This is in contrast to the trend of all the other presented data where SPC results in a decrease of the features intensity while the a-Si component decreases.

The behavior of these thin samples of the thickness series suggests that the 98 eV feature can not only be explained with Si defect states that can by passivated with hydrogen. Therefore an additional component that is related to the interface can be suggested as discussed in chapter 5.1.1.

6. Electronic structure of the a-SiO_x and µc-Si/ZnO:Al heterocontact

Like introduced in subchapter 2.3 the p-i-n a-Si (H) based solar cell structure uses ZnO:Al as the front contact of the device. However, previous investigations [13] have shown that a double p-layer design consisting of the combination of a microcrystalline and an amorphous p-layer results in a fill factor gain, which is illustrated in Figure 6.1. To further improve device performance (by an increase of transmission through the emitter) the p-type a-Si layer is often substituted by an oxygenated a-Si:H (a-SiO_x:H(B)). This chapter thus focuses on the characterization of the electronic properties of the a-SiO_x:H(B)/ZnO:Al structure compared to that of the µc-Si:H(B)/ZnO:Al stack in order to understand the empirically found cell improvement.

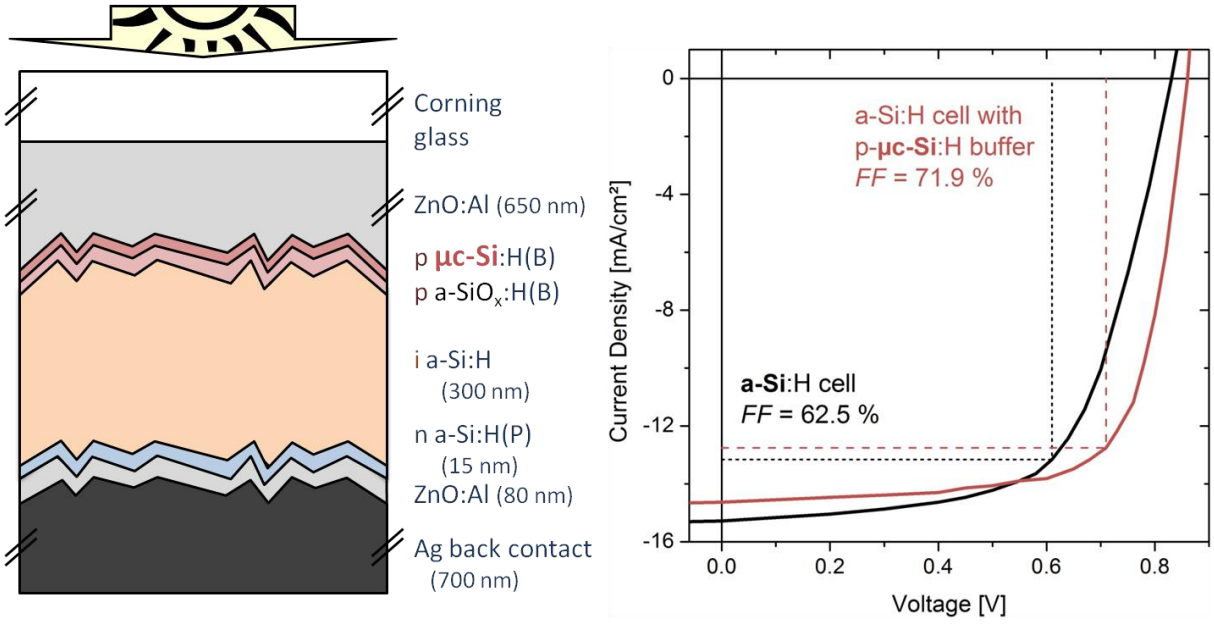

Figure 6.1: Left: Schematic presentation of a glass/ZnO:Al/a-SiO_x:H(B)/a-Si:H/a-Si:H(P) a-Si p-i-n solar cell with a µc-Si:H(B) buffer between ZnO:Al front contact and the emitter. Right: J-V curve of a cell without (black) compared to one with (red) µc-Si buffer **[13]**.

Samples were supplied by David Wippler, Forschungszentrum Jülich. Using plasma enhanced chemical vapor deposition (PECVD), boron doped hydrogenated oxygenated amorphous [a-SiO_x:H(B)] or microcrystalline Si [µc-Si:H(B)] were deposited onto a 800 nm thick

ZnO:Al film that was previously magnetron sputtered on a Corning Eagle glass substrate. PECVD precursor gases were silane, trimethyl borate (TMB), hydrogen and exclusively for the a-SiO_x:H deposition CO_2 (to further increase the a-Si band gap by introduction of oxygen into the film – see chapter 2.3). Varying the PECVD process time resulted in different sample thicknesses.

These Si/ZnO:Al samples were investigated by hard x-ray photoelectron spectroscopy (HAXPES). Using excitation energies (hν) ranging from 2 keV to 6 keV, core level (CL) and valence band (VB) photoemission spectra of the different thin-film Si/ZnO samples and a bare (i.e., uncovered) ZnO:Al reference layer were measured. As mentioned in chapter 3.2, the probing depth, x, is largely limited by the material- and energy-specific inelastic mean free path (IMFP) of the photoelectrons; the photoemission signal, I_0, is attenuated according to the exponential function:

$$I = I_0 \cdot e^{\frac{-x}{\cos\theta \cdot IMFP}} \qquad \textbf{6.1}$$

Hence, 95% of the signal stems from a region which corresponds to 3×IMFP, which is used as a measure for the information depth (ID) in the following. Hence, the ID of the core level spectra in this experiment ranges from below 12 nm (for 2 keV kinetic energy) up to 31 nm (for 6 keV kinetic energy) in crystalline silicon [65]. Because of the dominance of the IMFP on the measurement ID compared to the much longer attenuation length of the x-rays, the measurements were performed in nearly grazing incidence geometry, with the electron oriented nearly perpendicular to the sample surface, an orientation which maximizes the signal intensity of the HAXPES measurements.

The manner in which variations in (oxygenated amorphous or microcrystalline) Si:H(B) capping layer thickness, excitation energy, and thus photoelectron kinetic energy (and therefore IMFP and ID) can be combined to allow a “depth-resolved” characterization of the chemical and electronic structure of the silicon capping layer and of the buried interface can be inferred from the schematic in Figure 6.2. For all combinations of excitation energy and capping layer thickness, the contributions to the recorded spectra attributable to the sample surface, Si bulk, interface, and ZnO:Al substrate will differ, as indicated by the differences in the indigo area in each vicinity. The shape of the indigo cone is reflective of the exponential

attenuation of the photoelectron signals. Note that the kinetic energy of Auger electrons and thus the ID of Auger features is independent of excitation energy.

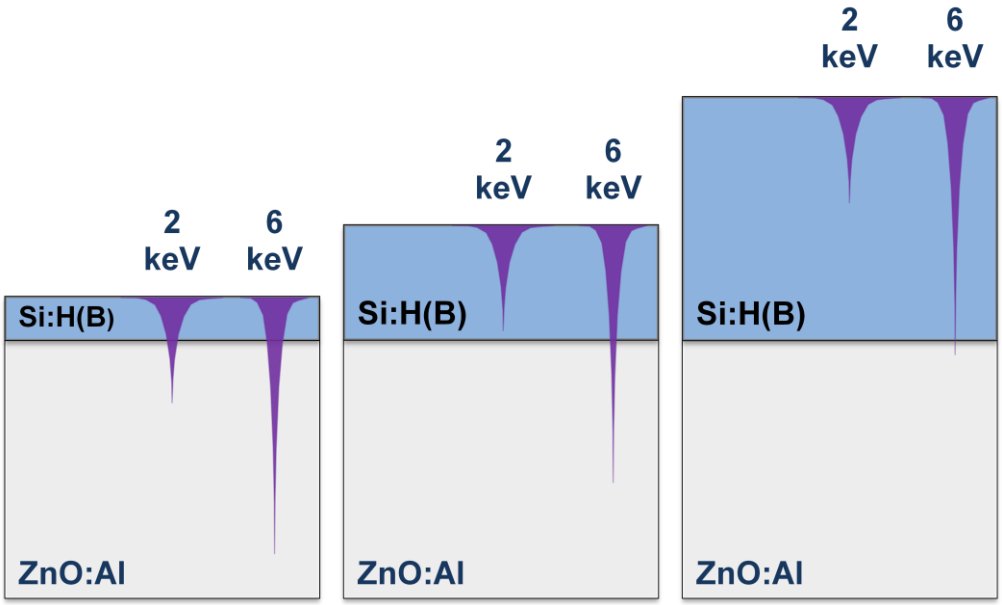

Figure 6.2: Visualization of the HAXPES probing depth profiles (indigo) for different photoelectron kinetic energies (2 and 6 keV) and capping layer thicknesses of the investigated (oxygenated amorphous or microcrystalline) Si:H(B)/ZnO:Al layer stacks. The areas of the probing depth cones are scaled according to the variation in information depth of a particular core level with given kinetic energies.

In Figure 6.2 a representation of the probed area in scale with the different Si thicknesses is shown. This variation of probing depth and capping layer thickness allows for a quasi "depth-profiling" of the buried interface structure.

Survey spectra of the samples show photoemission lines of silicon (Si 1s, Si 2s, Si 2p), oxygen (O 1s), carbon (C 1s) and for thin layers or high excitation energies zinc (Zn 2s, Zn 2p, Zn 3s, Zn 3p, Zn 3d). Two example survey spectra of the a-SiO_x:H(B) sample with 70 s deposition time can be seen in Figure 6.3 (Si 1s at 1616 eV is not shown).

Here the Zn photoemission line intensities are much higher for 5.9 keV excitation and almost vanish for 3.2 keV excitation showing that the silicon cover layer homogeniously covers the ZnO:Al and thus interface information is only obtainable for higher excitation energies.

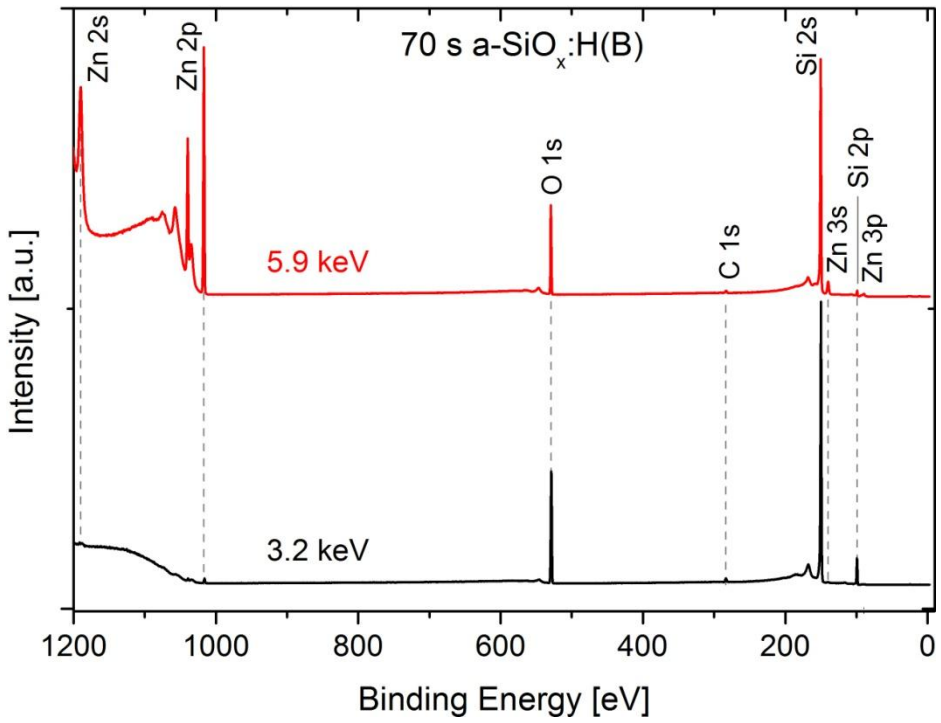

Figure 6.3: HAXPES survey spectra of the 70 s a-SiO_x:H(B)/ZnO:Al sample measured with 3.2 keV and 5.9 keV excitation energy.

The carbon content at the surface was calculated from the C 1s / Si 2s intensity ratio (taking cross sections into account [73]) in the survey spectra of the thickest samples with 6 keV excitation energy (not shown here). For both a-SiO_x:H(B) and µc-Si:H(B) a C/Si ratio of 21 ± 5 % was found. Thinner samples and lower excitation energies resulted in higher C/Si ratios. Due to the lower Si signal from thin films and the higher surface sensitivity of low excitation energies, this can be explained by an increasing influence of C-containing surface contaminations. Si $L_{2,3}$ XES spectra of these samples showed no SiC related spectral features (not shown). The unusually high content observed in the HAXPES survey spectra may thus be due to C contamination before (environmental exposure) or during measurements (adsorption of contaminants enhanced by ionization of the surface).

The samples were not treated by hydrofluoric acid prior introducing into the UHV system, so surface oxidation can be expected and was identified for all samples. The O 1s photoemission lines, which were found in every survey spectrum, were, however, not further analyzed. Instead the focus was on the Si 2s and Si 1s photoemission lines. As these also contain information on the oxidization state of the formed silicon oxide and relative quantity they are discussed in detail in the following.

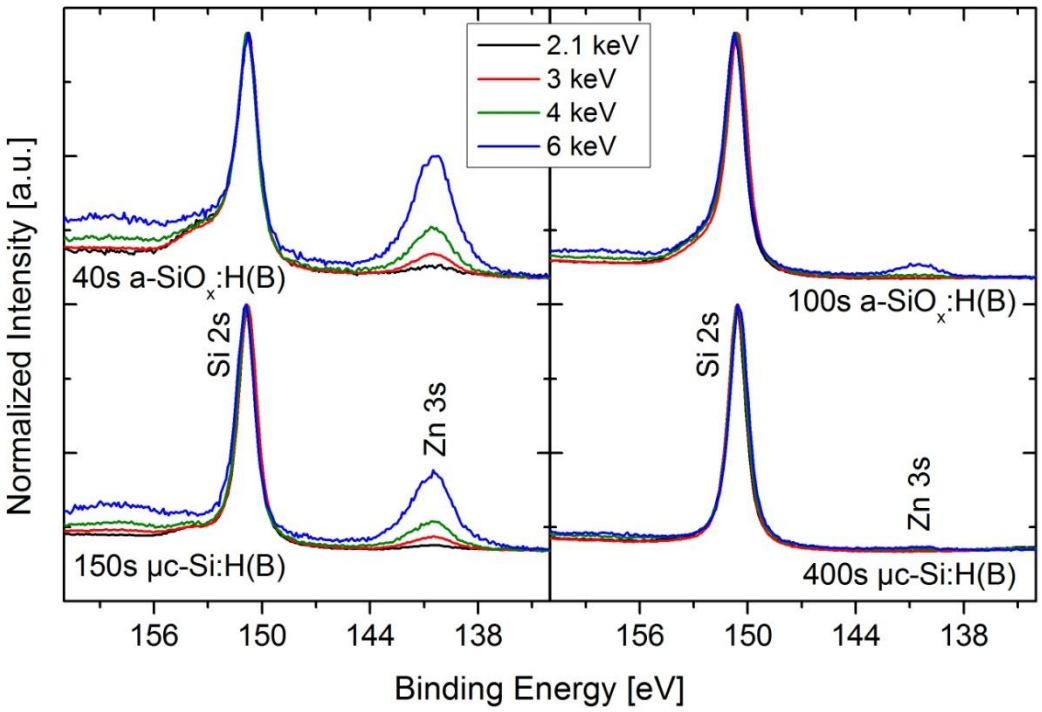

Figure 6.4: Si 2s and Zn 3s HAXPES spectra of the thinnest (left) and thickest (right) samples measured at different excitation energies (2.1 – 6 keV). The top and bottom groups of spectra correspond to the a-SiO_x:H(B)/ZnO:Al and µc-Si:H(B)/ZnO:Al thin-film solar cell structures, respectively. The spectra are normalized to the maximum height of the Si 2s photoemission line.

Detail spectra of the Si 2s line of the thinnest and thickest a-SiO_x:H(B) (40 s, 100 s) and µc-Si:H(B) (150 s, 400 s) layers measured at different excitation energies are shown in Figure 6.4. The binding energies of the Si 2s photoemission lines range from 150.6 to 150.8 eV, which is in agreement with literature values (150.5 – 150.7 eV) for Si-Si bonds [122]. As kinetic energy increases, the Zn 3s peak emerges from the background and increases in intensity for both pairs of samples. For the thin samples the Zn 3s is always detectable, while for the thick ones, it is only seen with the highest excitation energies confirming that both the excitation energy and the thickness of the silicon capping layer control the probed sample volume.

No systematic energy shift of the Si 2s peak (for a given sample) is observable with different excitation energies (i.e., different probing depths). Furthermore, the Si 2s lines of the amorphous silicon layers are broader than those of the microcrystalline silicon samples [e.g., 100 s a-SiO_x:H(B), hν = 6 keV: FWHM = (1.29 ± 0.02) eV; 400 s µc-Si:H(B), hν = 6 keV: FWHM = (1.23 ± 0.02) eV], which can be interpreted as being indicative of the higher degree of crystallinity [111] and thus electronic order.

For both types of samples (but more pronounced for the a-SiO_x:H(B)/ZnO:Al sample –due to oxidization from the CO_2 precursor) a shoulder at 154 eV and a broad feature at 158 eV (in particular for high excitation energies and the thin silicon layer sample) become more distinct. While the first can be ascribed to Si-O_x bonds [122][127], the latter is due to a normalization effect caused by the reduced intensity of the Si 2s line (which is normalized at the peak maximum) resulting in an increasing influence of the spectral background with increasing excitation energy and thus information depth.

In the case of µc-Si:H(B), the presence of Si-O_x bonds can mainly be attributed to surface oxidization. For the a-SiO_x:H(B) layer a significantly higher Si-O_x contribution is present due to the deliberate material oxygenation. From a two-component Voigt fit (accounting for a Si-Si and Si-O_x contribution) of the Si 2s spectra of the a-SiO_x:H(B) samples a Si-O_x/Si-Si intensity fraction of (26±2) % can be derived. However, this fraction must be considered a higher-bound approximation of the "true" Si-O_x bulk contribution because of the impact of surface oxides on the intensity ratio. Note that both thin Si samples exhibit a higher Si-O_x contribution, presumably due to the higher surface/bulk ratio and, potentially, the previously observed oxidation at the Si/ZnO:Al interface.

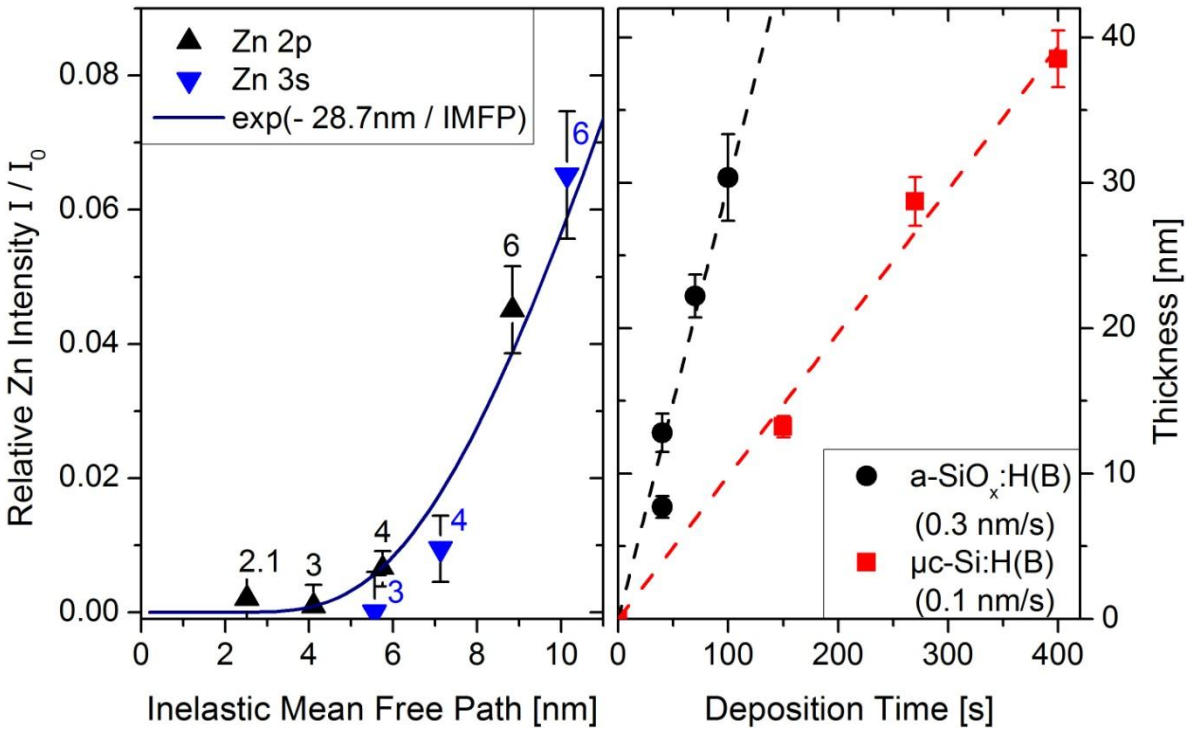

Figure 6.5: Left: Relative Zn 2p (▲) and Zn 3s (▼) line intensities plotted over the inelastic mean free path [65] for the 270 s µc-Si:H(B) sample. The exponential fit used to derive the layer thickness (see equation 3.16 in chapter 3.2) is shown as a dark blue solid line. The excitation energies (in keV) are indicated by the numbers next to the data points. Right: The resulting thicknesses of the a-SiO_x:H(B) (●) and µc-Si:H(B) (■) capping layers are plotted over the deposition time. Dashed lines represent linear fits with the slopes given in the legend.

The thicknesses of the silicon capping layers were determined by analyzing the Zn 2p and Zn 3s signal attenuation. The intensities of the Zn photoemission lines (I) were divided by those of the bare ZnO:Al reference (I_0) and plotted over the inelastic mean free path [65]. As an example, the resulting I/I_0 ratios for the 270 s µc-Si:H(B)/ZnO:Al sample are shown in Figure 6.5 (left panel). Exponential fits are made, and equation 3.16 of chapter 3.2 is used to derive the layer thicknesses - resulting in (28.7 ± 1.7) nm for the example. The determined thicknesses of all a-SiO_x:H(B) and µc-Si:H(B) layers are plotted in Figure 6.5 (right panel) versus deposition time and listed (together with the respective deposition times) in Table 1. Linear fits of the data in Figure 6.5 (right panel) give estimates for the deposition rates: (0.30 ± 0.02) nm/s for a-SiO_x:H(B) and (0.10 ± 0.01) nm/s for µc-Si:H(B).

Table 1: List of the investigated samples together with deposition time and determined layer thickness.

Type	Deposition time [s]	Thickness determined by HAXPES [nm]	Thickness determined by ellipsometry [nm]
a-SiO$_x$:H(B)	40	7.7 ± 0.7	9.2 ± 0.9
a-SiO$_x$:H(B)	40	12.8 ± 1.3	---
a-SiO$_x$:H(B)	70	22.2 ± 1.5	16.9 ± 1.7
a-SiO$_x$:H(B)	100	30.4 ± 3.0	---
µc-Si:H(B)	150	13.2 ± 0.7	---
µc-Si:H(B)	270	28.7 ± 1.7	---
µc-Si:H(B)	400	38.5 ± 1.9	---

Discrepancies between the thickness values estimates on our HAXPES measurements and the available thicknesses values determined by ellipsometry measurements (externally - also in Table 1) may reflect thickness variations across the deposition area. Note that two separate 40 s a-SiO$_x$:H(B) samples, deposited in two separate runs, are included in the analysis and show different thicknesses, which may again be due to thickness inhomogeneities or represent the degree of process reproducibility; the average thickness, of the two samples (10.3 ± 1.5 nm) is – within the error bar – in agreement with the ellipsometry derived value (9.2 ± 0.9 nm), though.

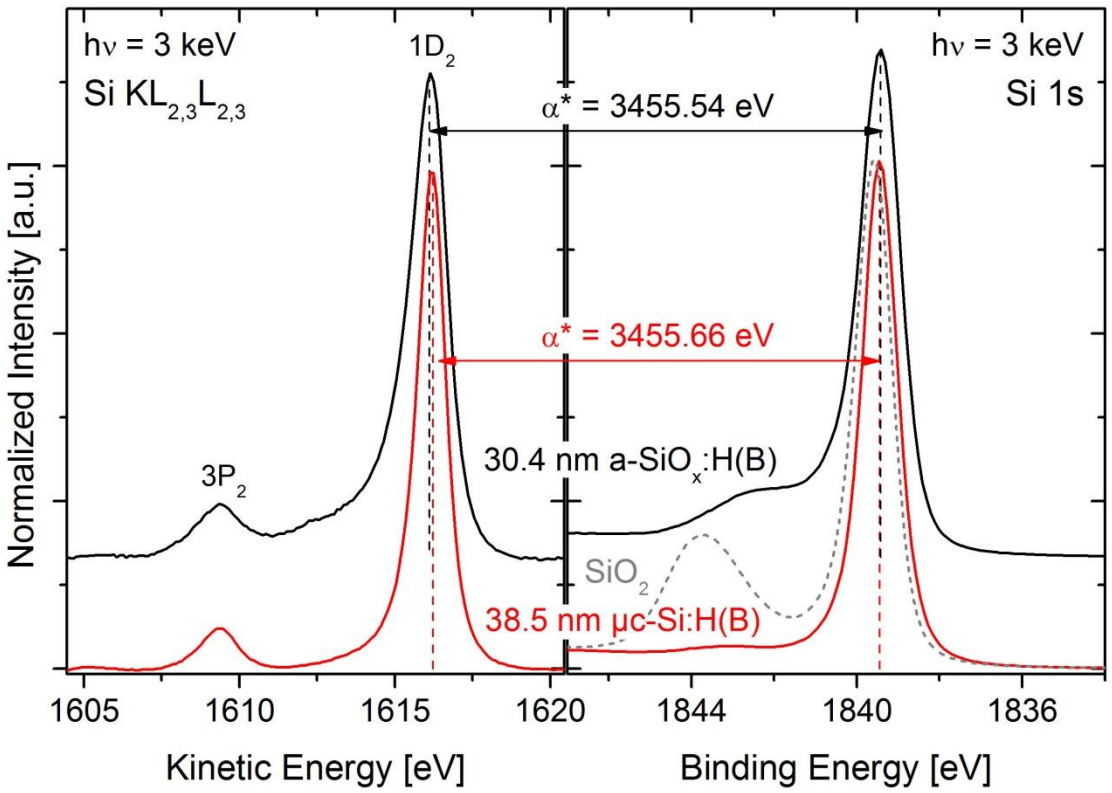

Figure 6.6: Si $KL_{2,3}L_{2,3}$ Auger electron (left) and Si 1s core level (right) spectra for the thickest a-SiO_x:H(B) (30.3 nm, black) and µc-Si:H(B) (38.4 nm, red) samples recorded using 3 keV excitation energy. The calculated modified Auger parameters (± 0.14 eV), α*, are also shown. For comparison, an oxidized Si-Wafer Si 1s spectrum is plotted (dashed grey line).

In Figure 6.6 the Si $KL_{2,3}L_{2,3}$ Auger and Si 1s photoelectron spectra (hν = 3 keV) of the thickest (30.4 nm) a-Si:H(B) sample are compared to corresponding spectra of the thickest (38.5 nm) µc-Si:H(B) sample. The Auger spectra are dominated by the Si $KL_{2,3}L_{2,3}$ ($1D_2$) transition at (1616.11 ± 0.05) eV kinetic energy for a-SiO_x:H(B) [(1616.22 ± 0.05) eV for µc-Si:(B)], which can be assigned to Si-Si bonds [122]. The feature at approximately 1609 eV can be attributed to the accompanying $3P_2$ Auger transition [128].

The Si 1s photoelectron spectra are dominated by the peak at a binding energy of (1839.43 ± 0.1) eV for a-SiO_x:H(B) [(1839.44 ± 0.1) eV for µc-Si:(B)], which is also characteristic of Si-Si bonds [122]. The broad, high-energy shoulder between 1842 and 1844 eV (more pronounced for the amorphous sample) is attributable to Si-O_x bonds [122], in agreement with the interpretation of the previously shown Si 2s spectra. The energy split between Si-O_x and Si-Si contribution excludes SiO_2 and rather suggests the presence of a silicon suboxide (SiO_x, with $x<2$) [127], which is obvious when comparing both spectra to that of an oxidized Si-Wafer reference (as seen in Figure 6.6).

Furthermore, the Si 1s photoemission line [a-SiO_x:H(B), hν = 6 keV: FWHM = (1.01 ± 0.02) eV; µc-Si:H(B), hν = 6 keV: FWHM = (0.91 ± 0.02) eV] as well as the $KL_{2,3}L_{2,3}$ Auger feature are narrower for the µc-Si:H(B) than for the a-SiO_x:H(B) layer, again indicating a higher degree of crystallinity.

In order to further evaluate the chemical structure the modified silicon Auger parameter, α^*, was calculated using the kinetic energy (E_{kin}) of the Si $KL_{2,3}L_{2,3}$ ($1D_2$) Auger and the binding energy (E_B) of the Si 1s photoemission lines. For the data presented in Figure 6.6, the Auger parameters are (3455.54 ± 0.14) eV and (3455.66 ± 0.14) eV for the a-SiO_x:H(B) and µc-Si:H(B) films, respectively. The derived α^* (Si) values are in good agreement with the reported modified Auger parameter of silicon (3455.5 eV or 3456.3 eV) [62]. Note the significant difference for the modified Auger parameters of SiC (3453.7 eV) and SiO_2 (3451.5 eV) [62]. The small (but, on a relative scale, significant) α^* (Si) difference between a-SiO_x:H(B) and µc-Si:H(B) is most likely indicative for the different amount of oxygenation.

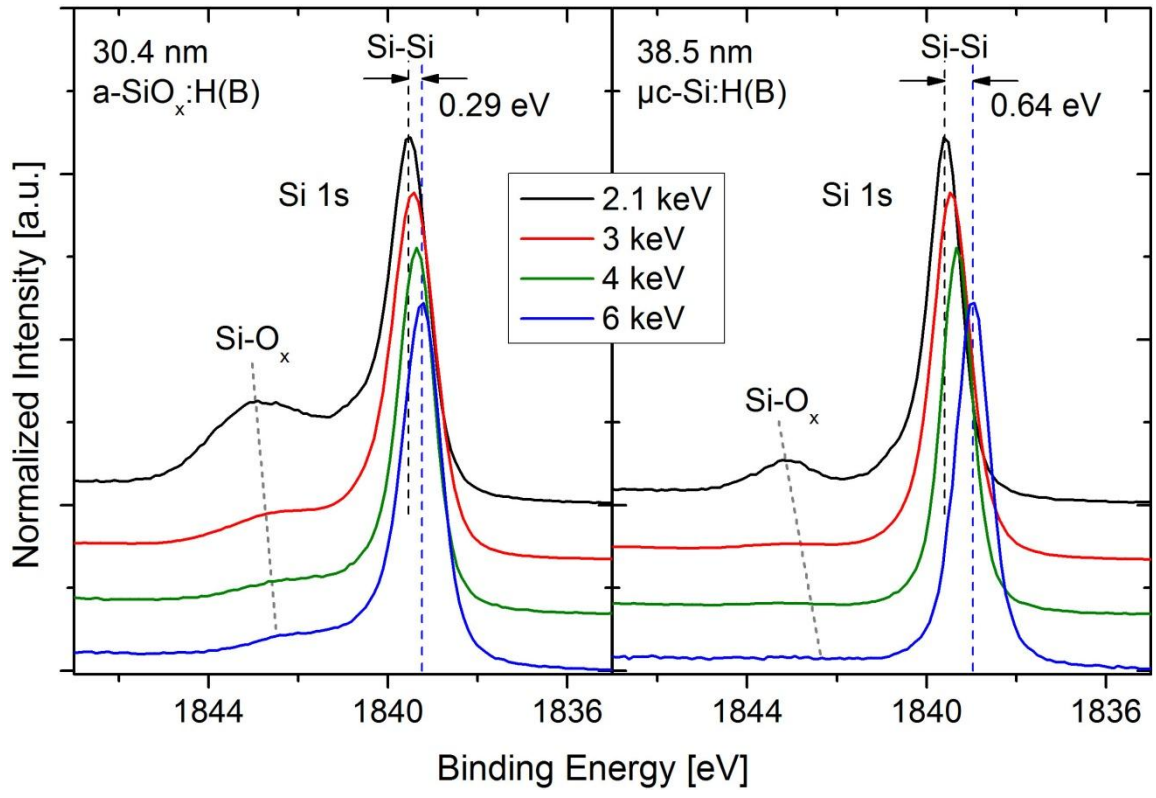

Figure 6.7: Si 1s spectra of the thickest (30.4 nm) a-SiO_x:H(B) (left) and (38.5 nm) µc-Si:H(B) (right) samples measured at various excitation energies. Excitation energy dependent shifts are indicated by the dashed vertical lines, and a vertical offset is added for clarity. The maximum shift is given for both cases (within an uncertainty of ± 0.14 eV).

Figure 6.7 shows Si 1s photoemission spectra measured for the thickest a-SiO_x:H(B) (left panel) and µc-Si:H(B) (right panel) samples using several excitation energies. The intensity of the peak at approximately 1843 eV – ascribed to SiO_x (with x<2, see discussion above and [122] [127] – decreases with increasing excitation energy, indicating that the silicon suboxide is mainly present at the sample surface. However, it was shown in chapter 5.1 and was previously reported ([47][111]) that Si oxidation also occurs at the Si/ZnO interface of solid-phase crystallized polycrystalline silicon on ZnO:Al; thus interface oxidation can also not be excluded as an additional explanation in this case. The more pronounced silicon oxidation of the a-SiO_x:H(B) thin layers, compared to that observed for the µc-Si:H(B) samples, should be due to the CO_2 precursor used for a-SiO_x:H(B) deposition.

Furthermore, the Si 1s spectra of the a-SiO_x:H(B)/ZnO:Al and µc-Si:H(B)/ZnO:Al samples shift (0.29 ± 0.14) eV and (0.64 ± 0.14) eV, respectively, to lower binding energies as the excitation energy increases from 2.1 keV to 6 keV. The fact that no similar shift occurs in the Si 2s lines – for which effectively constant binding energies are observed (see Figure 6.4) – suggests, initially, that this shift cannot be explained in a classical band bending picture, because the same shifts would be expected for all photoemission lines in that case. However, the signals in question (i.e., the Si 1s and Si 2s lines) have greatly different kinetic energies, and therefore significantly different information depths [$ID_{Si\ 1s}$ (2.1 keV) = 2.7 nm and $ID_{Si\ 2s}$ (2.1 keV) = 12.2 nm for Si 1s and Si 2s, respectively]. Hence, the more surface sensitive Si 1s photoemission line would be significantly more influenced by the presence of a surface band bending. As a consequence, it can be speculated that the observed deviation in the shifts of the Si 1s and Si 2s lines could therefore be indicative of a pronounced downward band bending limited to the very surface of the a-SiO_x:H(B) and µc-Si:H(B) layers. The less pronounced Si 1s shift (and presumably smaller surface band bending) observed for the amorphous silicon layer could then be explained by a surface Fermi level pinning caused by the higher defect-concentration. But an a-Si cover layer on top of the crystals (as described in chapter 4.1) might as well be the cause of the bigger shift of Si 1s observed for µc-Si:H(B). In this case the Si 1s peak of µc-Si:H(B) would be influenced by a-Si:H(B) for low excitation energies. For increasing excitation energies – and thus information depth – a shift towards the higher binding energy of the bulk µc-Si:H(B) would occur, increasing the total effect.

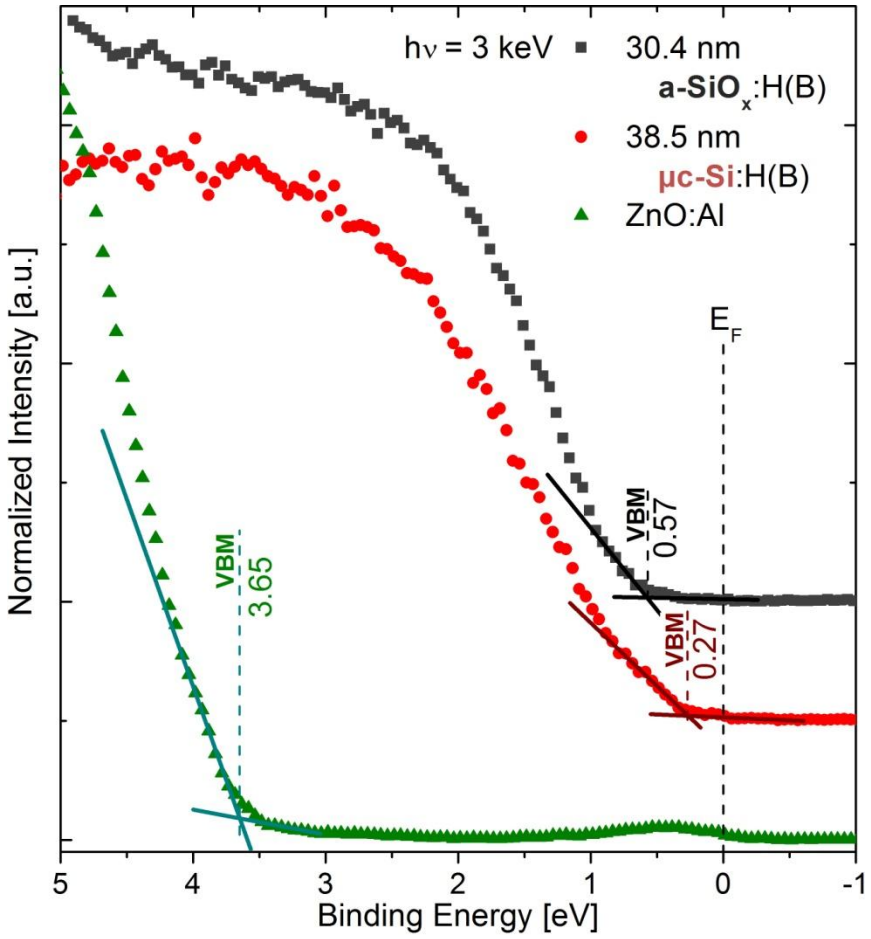

Figure 6.8: HAXPES spectra of the valence band region for the thick a-SiO_x:H(B) layer (■), the thick µc-Si:H(B) (●) and the ZnO:Al (▲) reference using an excitation energy of 3 keV. The VBM are determined by linear approximation of the leading edge error bars are given in the text.

Figure 6.8 shows the HAXPES valence band spectrum of the bare ZnO:Al reference compared to the spectrum of the thick a-SiO_x:H(B) (30.3 nm) and thick µc-Si:H(B) (38.4 nm) layer measured with 3 keV excitation energy. These two thick samples were investigated by using elevated excitation energy to minimize the impact of surface contamination for the determination of the valence band maximum (VBM) of the Si:H(B).

The locations of the VBM are determined by linear approximation of the leading VB edge averaging over possible line approaches. The VBM of the ZnO:Al reference is found to be (3.65 ± 0.20) eV, which is significantly higher than the band gap (E_g) commonly reported for ZnO (3.3 eV, [37][38]). For highly-doped ZnO a Burstein-Moss shift (explained in chapter 2.2) of E_g is well-known; in highly Al-doped ZnO E_g values of up to 3.8 eV are reported in literature [40]. The spectrum of the ZnO:Al layer reveals an increase in intensity close to the Fermi level (E_F) indicating the presence of significant density of occupied states. This feature was observed before in HAXPES spectra of highly Al-doped ZnO and ascribed to deep defect

levels [129]. Based on the large band gap and the observed intensity around 0 eV binding energy, it can be expected that E_F of the here studied ZnO:Al lies well within the conduction band (CB). Hence, the investigated ZnO:Al material can be considered to be a degenerated semiconductor.

The determination of the Si VBM is less straight forward than for the ZnO:Al due to the downwards band bending towards the surface that was found in the Si 1s spectra (see Figure 6.7). Major contributions of the VB spectrum would be affected by this band bending due to the surface-sensitivity of XPS so that the VBM appears to be at higher binding energies – it curves away from E_F towards the surface. To account for that only the most leading edge (foot of the VB) is considered in the line approach assuming that it represents the more deeply buried VBM. Resulting VBMs are (0.57 ± 0.10) eV for a-SiO_x:H(B) and (0.27 ± 0.10) eV for µc-Si:H(B).

In a first (approximate) step towards the determination of the VB offsets (VBO) at the ZnO:Al/a-SiO_x:H(B) and ZnO:Al/µc-Si:H(B) interfaces, the observed VBM values for the Si capping layers and ZnO:Al are compared. The VBM value of the capping layers is closer to E_F than that of the ZnO:Al; this suggests a positive VBO. In the second step, the binding energy of substrate and cover layer core levels is used to monitor and correct for interface-induced band bending (IIBB) as demonstrated by Bär et. al. [130].

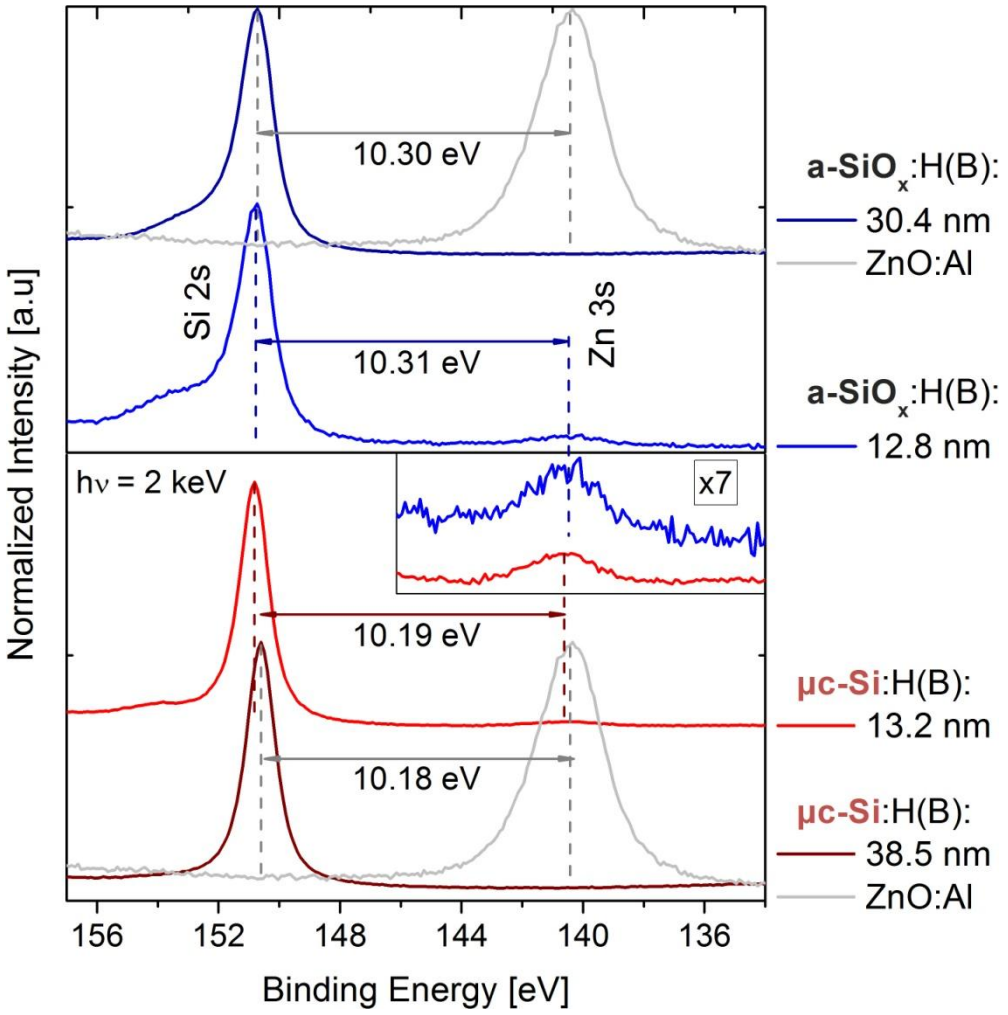

Figure 6.9: Si 2s and Zn 3s HAXPES spectra measured at 2 keV excitation energy. Top (bottom): The thinnest and thickest a-SiO_x:H(B) (µc-Si:H(B)) samples are compared to the bare ZnO:Al substrate. The inset shows a magnification of the Zn 3s area for the thin Si samples. Line positions that were obtained by Voigt fits are indicated and Si 2s – Zn 3s split values - that are relevant for calculating the IIBB - are given (± 0.14 eV).

Figure 6.9 shows the Si 2s and Zn 3s core level spectra that are used to calculate the IIBB. This is done by subtracting the split (energy difference) between the core levels of the capping layer and the substrate of a thin sample [e.g. $E_{\text{Si 2s, 12.8nm a-SiOx:H(B)}} - E_{\text{Zn 3s, 12.8nm a-SiOx:H(B)}} = (10.31 \pm 0.14)$ eV] from the split of the cover layer core level of a thick cover layer reference and the substrate core level of the bare substrate reference [e.g. $E_{\text{Si 2s, 30.4nm a-SiOx:H(B)}} - E_{\text{Zn 3s, ZnO:Al}} = (10.30 \pm 0.14)$ eV]. This results in a IIBB for a-SiO_x:H(B) of (0.01 ± 0.20) eV and for µc-Si:H(B) of (0.01 ± 0.20) eV. Subtracting the IIBB from the difference of the VBM values of Si and ZnO:Al results in the VBO which is therefore (3.07 ± 0.25) eV for a-SiO_x:H(B)/ZnO:Al and (3.37 ± 0.25) eV for µc-Si:H(B)/ZnO:Al.

In addition to this classical approach to determine the VBO, an attempt to use HAXPES to directly measure the VBO was undertaken.

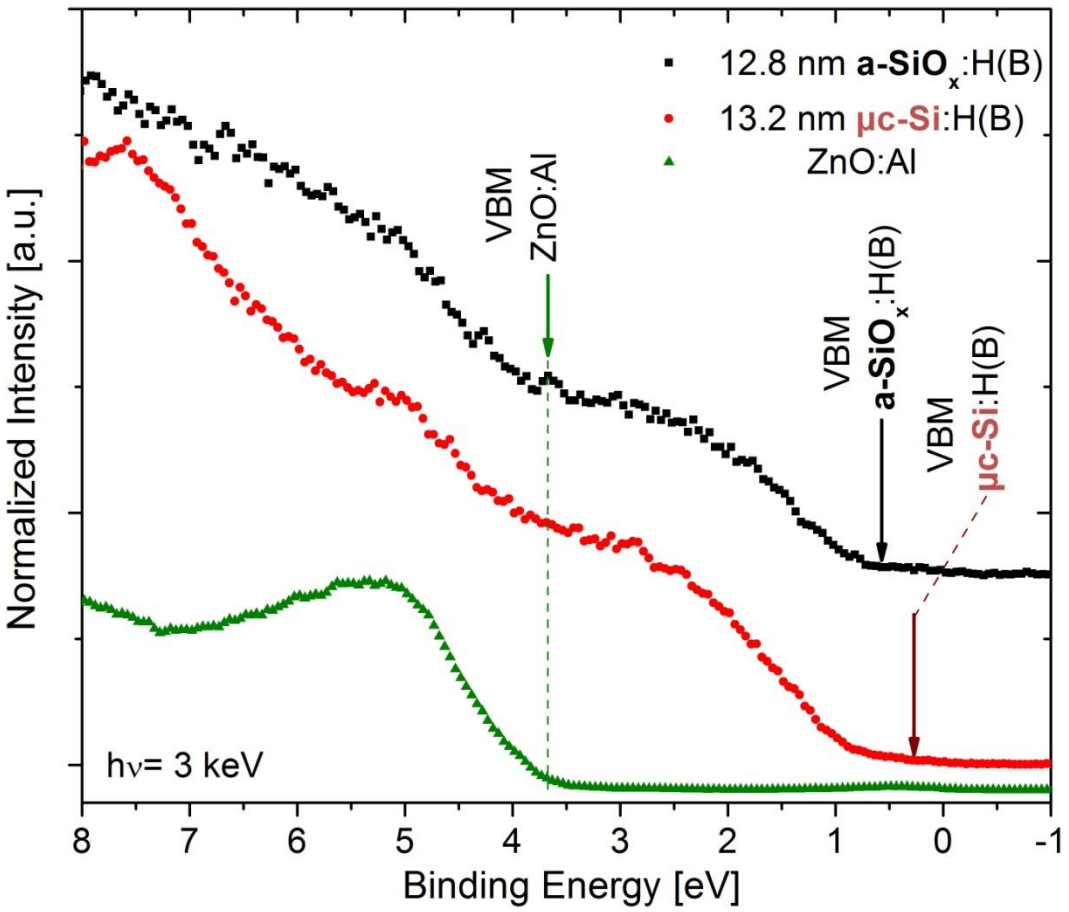

Figure 6.10: HAXPES valence band region spectra of the thin a-SiO_x:H(B) (■) and thin µc-Si:H(B) (●) on ZnO:Al compared to the bare ZnO:Al substrate (▲). Arrows indicate the VBM positions from Figure 6.1.

Shown in Figure 6.10 are HAXPES spectra of the VB region of thin Si layers on ZnO:Al compared with the bare ZnO:Al substrate. Here the combination of Si thickness and information depth was chosen in such a way that both the VB of the Si cover layer as well as that of the ZnO:Al substrate can be clearly observed in the same spectrum (as indicated by the arrows) – in 'one shot'.

To determine the values of the VBM the respective regions of the same spectra are magnified in Figure 6.11.

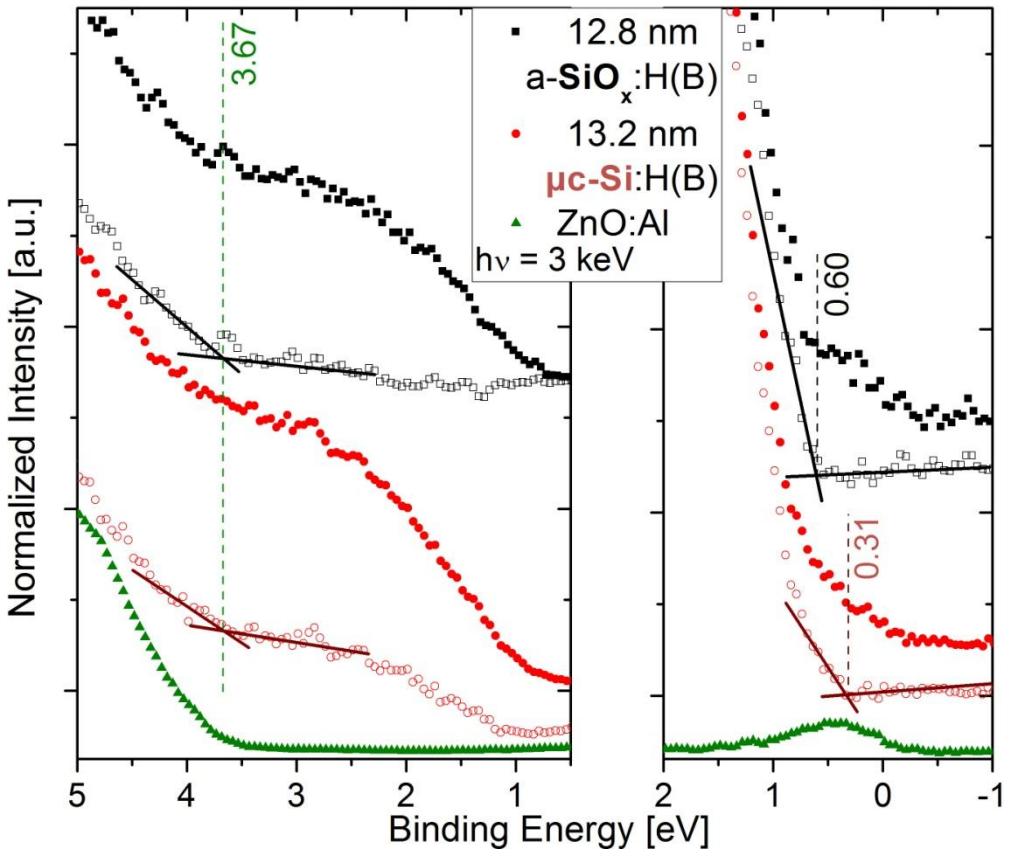

Figure 6.11: HAXPES valence band region spectra of the thin a-SiO_x:H(B) (■) and thin µc-Si:H(B) (●) on ZnO:Al compared to the bare ZnO:Al substrate (▲). Left: Open symbols represent difference spectra where the thick a-SiO_x:H(B) (□) or µc-Si:H(B) (○) reference are subtracted (for the references spectra see Figure 6.8). Right: Open symbols represent difference spectra from the ZnO:Al. Linear approximations of the leading edge are done at these difference spectra.

Here the determination of the VB leading edges is more challenging, as these overlap with the Si VB for the ZnO:Al VBM region and the deep defect levels of ZnO:Al for the Si VBM region. Therefore these spectra had weighted reference spectra subtracted before the leading edge was aproximated. Reference spectra of the same excitation energy were taken from the 30.4 nm thick a-SiO_x:H(B), the 38.5 nm thick µc-Si:H(B) (both shown in Figure 6.8) and the bare ZnO:Al.

Linear approximation of the leading edges of the difference spectra result in VBM values for ZnO:Al of (3.67 ± 0.22) eV for both thin Si samples, (0.60 ± 0.22) eV for 12.8 nm a-SiO_x:H(B) and (0.31 ± 0.22) eV for 13.2 nm µc-Si:H(B). Any effect of an IIBB would be included in these measurements directly. The resulting VBOs are therefore directly given by the difference of the Si and ZnO:Al VBMs which is - (3.07 ± 0.31) eV for a-SiO_x:H(B)/ZnO:Al and - (3.36 ± 0.31) eV for µc-Si:H(B)/ZnO:Al. This is in the same range

as the VBO values resulting from the 'classical' approach - (3.07 ± 0.25) eV for a-SiO_x:H(B)/ZnO:Al and - (3.37 ± 0.25) eV for µc-Si:H(B)/ZnO:Al.

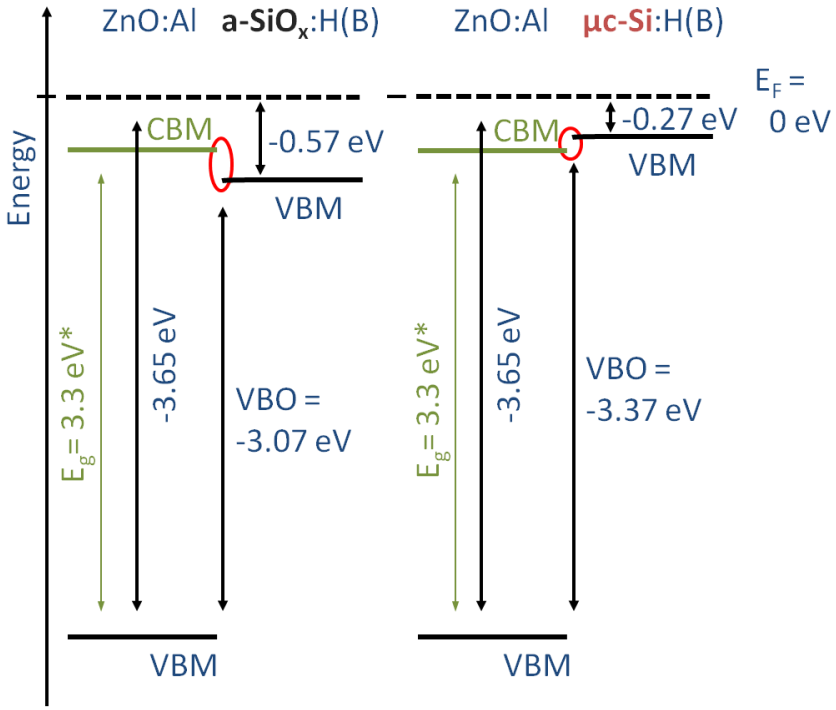

Figure 6.12: Electronic structure of the a-SiO_x:H(B)/ZnO:Al and µc-Si:H(B)/ZnO:Al interface based on HAXPES measurements. Error bars are given in the text. (* To estimate the relative position of the ZnO:Al CBM, the band gap value of undoped ZnO is included [37][38]).

Figure 6.12 shows the electronic structure obtained using the 'classical' method. To estimate the position of this CBM, the optical band gap of the undoped ZnO (E_g = 3.3 eV) [37][38] was used and added to the VBM values in Figure 6.12. The relevant energy barriers are marked with red circles. The energetic height of the tunnel barrier can therefore be calculated by subtracting the VBO from E_g. For the µc-Si:H(B)/ZnO:Al interface the height of this barrier height is lower [(-0.08 ± 0.31) eV] than for the a-SiO_x:H(B)/ZnO:Al interface [(0.22 ± 0.31) eV], so the tunnel junction contact is more preferred for the µc-Si:H(B)/ZnO:Al than for the a-SiO_x:H(B)/ZnO:Al interface. This means that the photo-generated holes are much more likely to tunnel into the TCO front contact and contribute to the current if p-type µc-Si is used as a buffer for the p-i-n a-Si:H cell, and this could be the cause of the better performance of that cell.

Another beneficial effect of using the p-type µc-Si at the ZnO:Al interface is related not to the tunnel barrier height but to its width. The expected higher doping efficiency in µc-Si compared to a-Si results in a smaller space charge region width at the interface and therefore

reduces the “tunnel distance”. Thus, altogether charge transport across the Si/ZnO tunnel junction is energetically more favorable for the µc-Si:H(B)/ZnO:Al than for the a-SiO_x:H(B)/ZnO:Al interface.

To summarize, by performing a “depth resolved” HAXPES investigation of a-SiO_x:H(B) and µc-Si:H(B) on ZnO:Al, the thickness and deposition rate of the Si cover layer could be determined. By evaluating surface sensitive Si 1s core hole spectra, a surface band bending was revealed, that was taken into account when further investigating the electronic structure of the buried Si/ZnO:Al interface. The study of valence band spectra revealed that the ZnO:Al layer is degenerated and the Fermi level lies inside the conduction band. The interface-induced band bending (IIBB) and band offset between Si and ZnO:Al were determined by two different methods, which revealed the absence of IIBB and a valence band offset of - (3.07 ± 0.25) eV at the a-SiO_x:H(B)/ZnO:Al interface and - (3.37 ± 0.25) eV at the µc-Si:H(B)/ZnO:Al interface.

With this band offset and the energy gap of an undoped ZnO, the position of the conduction band minimum of ZnO:Al could be estimated. From this and the measured valence band maxima of the Si cover layers, the tunnel barrier was determined for a-SiO_x:H(B)/ZnO:Al (0.22 ± 0.31) eV and µc-Si:H(B)/ZnO:Al: (-0.08 ± 0.31) eV. The lower tunnel barrier for µc-Si:H(B) explains the empirically [13] found solar cell efficiency increase when using an µc-Si(B) buffer for a p-i-n a-Si:H solar cell on ZnO:Al.

7. Conclusion and outlook

It was revealed that Si $L_{2,3}$ x-ray emission spectra (XES) of silicon thin films are very sensitive to the layer crystallinity. It was shown that the spectra can be well-described by a superposition of reference spectra of amorphous Si (a-Si) and monocrystalline (wafer) Si (c-Si). The crystalline spectral component determined from corresponding fits was proven to be a valid measure for the degree of crystallinity. This was confirmed by comparison with crystallinity values conventionally determined by Raman spectroscopy. According to the presented XES quantification model, no spectrum of any measured thin-film Si sample showed complete crystallization – a measurable a-Si component of 5-20 % remained, even for extended solid phase crystallization (SPC) times.

This observation was further analyzed with electron backscatter diffraction (EBSD) measurements. Through determining the grain size distribution and correlating the median grain size with the Si $L_{2,3}$ XES-determined crystalline component, different models based on columnar grains were developed. Based on these models, the remaining a-Si content after SPC is attributed to distorted material at the grain boundaries, estimated to be approximately (1.5 ± 0.5) nm on average. The models that include amorphous/distorted material also on top of the grains at the sample surface exhibited best agreement with the measured XES data, suggesting that such a surface layer needs to be considered especially in surface-sensitive photoemission studies. Also the impact of potentially present a-Si surface layers on the interfaces formed in resulting devices may influence the device performance.

With the acquired quantification approach, Si $L_{2,3}$ XES was further used to investigate the impact of dopants on the SPC-induced crystallization process. By evaluating the influence of SPC annealing time the crystallization velocity was estimated. It was found that a-Si:H thin films on ZnO:Al/glass substrate crystallize – compared to the crystallization of undoped (intrinsic) a-Si:H – faster if p- (boron) but much slower if n- (phosphorous) dopants are present. By including a SiO_2 reference in the superposition quantification approach, an

increase of SiO_2 with SPC time was observed, indicative for an oxidation at the Si/ZnO:Al interface. In B K XES and x-ray absorption spectra (XAS) of boron-doped samples similar amorphous-crystalline transitions as in Si $L_{2,3}$ XES and XAS were observed upon SPC, but they occurred at earlier times which hints towards boron being a nucleation center for crystallization – in-line with the above-mentioned finding.

For all Si $L_{2,3}$ XES of a-Si and n^+ doped poly-Si, a spectral feature above the valence band maximum at 100 eV was observed. A detailed quantification suggests that this feature might be attributed to occupied defect states in amorphous samples. The observed absence for p^+-type and undoped poly-Si samples and the fact that these features shift and gain intensity for n^+-doped samples upon SPC suggests a second origin: occupied dopant states.

The SPC-induced crystallization processes of a-Si:H(P) samples deposited on ZnO:Al/glass and SiN_x/glass substrates were directly compared with Si $L_{2,3}$ XES in order to study the impact of the substrate on crystallization behavior. The crystallization velocity of a-Si:H was found to be faster if the Si thin film was deposited on ZnO:Al/glass substrates. This might be explained with aluminum diffusing from the ZnO:Al into the Si during SPC, where the atoms may act as crystallization centers (like boron). An evaluation of the SiO_2 spectral contribution confirmed the oxidation of the Si/ZnO:Al interface. The fact that the fitted SiO_2 components for the Si thin films on SiN_x/glass substrates were lower than those found for the Si/ZnO:Al/glass samples, points to ZnO:Al as the (oxygen) source for the observed interface oxidation of Si. As a conclusion, it can be speculated that this accompanies the liberation of Zn and Al atoms, which as a consequence can then diffuse into the Si during SPC, which might be detrimental to the device.

The investigation of a thickness series of a-Si:H(P) on ZnO:Al/glass substrates compared to respective a-Si:H(P)/SiN_x/glass samples with Si $L_{2,3}$ XES before (i.e., as-deposited) and after SPC again confirmed interface oxidization upon SPC. An unusual spectral shape was found for thin samples that could not be explained satisfyingly by a superposition of a-S, c-Si and SiO_2 reference spectra. The residuum of the corresponding fits exhibited a maximum at 98 eV that could not be explained with possible interface species, such as zinc silicate and aluminum silicate. Thus the 98 eV feature was further investigated and it was found (by carefully monitoring the spectral changes induced by heating of a-Si:H and by hydrogen passivation of poly-Si) that its intensity is related to the hydrogen content of the Si samples. Evaluating the

intensities upon SPC for thin poly-Si layers also suggested a possible intensity increase of this feature related to the interface or the surface-bulk ratio of the samples.

An investigation of the poly-Si/ZnO:Al interface with x-ray photoelectron emission spectroscopy (X-PEEM), again confirmed interface oxidation. Furthermore, spatially resolved x-ray photoelectron spectra of sample areas where the poly-Si cover layer was mechanically removed from the ZnO:Al hinted at the formation of Si sub oxides or zinc silicate as an interface species.

By performing a "depth resolved" investigation of a-SiO_x:H(B) and µc-Si:H(B) on ZnO:Al/glass with hard x-ray photoelectron spectroscopy (HAXPES) the thickness and deposition rate of the Si cover layer could be determined. Through the evaluation of surface sensitive Si 1s core level spectra, a surface band bending was observed limited to the very top of the studied samples. This might be related to surface oxidization or the amorphous/distorted surface layer. This was taken into account when determining the electronic structure of the buried Si/ZnO interface. The interface induced band bending and band offset was determined by two different methods. In any case, by estimating the conduction band minimum (CBM) of ZnO:Al by adding the optical band gap of ZnO to the position of the ZnO:Al valence band maximum (VBM), the tunnel barrier between the VBM of the Si cover layers and the ZnO:Al CBM was determined. A tunnel barrier of (0.22 ± 0.31) eV for the a-SiO_x:H(B)/ZnO:Al and (-0.08 ± 0.31) eV was found for the µc-Si:H(B)/ZnO:Al contact. The lower tunnel barrier for µc-Si:H(B) explains the empirically found solar cell efficiency increase when using an µc-Si(B) buffer layer between a-SiO_x:H(B) and the ZnO:Al TCO front contact in p-i-n a-Si:H solar cells.

Expanding on these findings, one would try to confirm and verify the presence of an amorphous/distorted surface layer with surface-sensitive lab-based methods like x-ray photoelectron spectroscopy (XPS) or ultraviolet photoelectron spectroscopy (UPS) in a next step. If confirmed, the effect of this surface layer on the interface formation in respective solar cell structures, as e.g. the ZnO:Al/Si interface (if ZnO:Al is deposited onto Si – a very prominent interface in Si thin-film devices), would be of particular interest. Additionally, the different doping efficiencies ("active" dopant atoms) in c-Si and a-Si may have an effect on the electronic structure at the ZnO:Al/Si interface. The impact of different velocities of crystallization (due to, e.g. different dopants) on complete Si-based solar cell stacks also needs additional attention, as e.g. the presence of different dopants might introduce

performance-limiting effects like different grain sizes for differently doped areas or in-plane grain boundaries due to doping gradients. It may also be interesting to study the SPC-induced diffusion of dopants across initially well-designed interfaces and how this is influenced by the different rates of crystallization. In addition, the diffusion of substrate elements into the different silicon layers of the solar cell device is composed and/or interfacial chemical reactions need to be prevented and hence this topic also requires further analysis efforts. If all these aspects of thin-film Si PV are understood and optimized, a competition with other thin-film technologies on the sole basis of solar cell efficiency may be possible.

References

[1] M. A. Green, K. Emery, Y. Hishikawa, W. Warta, and E. D. Dunlop, "Solar cell efficiency tables (version 40)," *Progress in Photovoltaics: Research and Applications*, vol. 20, no. 5, pp. 606–614, 2012.

[2] S. Benagli, D. Borrello, E. Vallat-Sauvain, J. Meier, U. Kroll, J. Hötzel, J. Bailat, J. Steinhauser, M. Marmelo, G. Monteduro, and L. Castens, "High-Efficiency Amorphous Silicon Devices on LPCVD-ZnO TCO Prepared in Industrial KAI TM-M R&D Reactor," in *EUPVSEC Proceedings*, 2009, pp. 2293 – 2298.

[3] D. Staebler and C. Wronski, "Reversible Conductivity Changes in Discharge-Produced Amorphous Si," *Applied Physics Letters*, vol. 31, no. 4, pp. 292–294, 1977.

[4] X. Deng and E. A. Schiff, "Amorphous Silicon–Based Solar Cells," in *Handbook of Photovoltaic Science and Engineering*, A. Luque and S. Hegedus, Eds. John Wiley & Sons, Ltd, 2005, pp. 505–565.

[5] A. V. Shah, H. Schade, M. Vanecek, J. Meier, E. Vallat-Sauvain, N. Wyrsch, U. Kroll, C. Droz, and J. Bailat, "Thin-film silicon solar cell technology," *Progress in Photovoltaics: Research and Applications*, vol. 12, no. 2–3, pp. 113–142, 2004.

[6] J. Meier, S. Dubail, R. Platz, P. Torres, U. Kroll, J. A. Anna Selvan, N. Pellaton Vaucher, C. Hof, D. Fischer, H. Keppner, R. Flückiger, A. Shah, V. Shklover, and K.-D. Ufert, "Towards high-efficiency thin-film silicon solar cells with the 'micromorph' concept," *Solar Energy Materials and Solar Cells*, vol. 49, no. 1–4, pp. 35–44, Dec. 1997.

[7] M. A. Green, P. A. Basore, N. Chang, D. Clugston, R. Egan, R. Evans, D. Hogg, S. Jarnason, M. Keevers, P. Lasswell, J. O'Sullivan, U. Schubert, A. Turner, S. R. Wenham, and T. Young, "Crystalline silicon on glass (CSG) thin-film solar cell modules," *Solar Energy*, vol. 77, no. 6, pp. 857–863, Dec. 2004.

[8] R. B. Bergmann, G. Oswald, M. Albrecht, and V. Gross, "Solid-phase crystallized Si films on glass substrates for thin film solar cells," *Solar Energy Materials and Solar Cells*, vol. 46, no. 2, pp. 147–155, May 1997.

[9] T. Matsuyama, K. Wakisaka, M. Kameda, M. Tanaka, T. Matsuoka, S. Tsuda, S. Nakano, Y. Kishi, and Y. Kuwano, "Preparation of High-Quality n-Type Poly-Si Films by the Solid Phase Crystallization (SPC) Method," *Japanese Journal of Applied Physics*, vol. 29, pp. 2327–2331, 1990.

[10] O. Nast, T. Puzzer, L. M. Koschier, A. B. Sproul, and S. R. Wenham, "Aluminum-induced crystallization of amorphous silicon on glass substrates above and below the eutectic temperature," *Applied Physics Letters*, vol. 73, no. 22, pp. 3214–3216, Nov. 1998.

[11] K. Ishikawa, M. Ozawa, C.-H. Oh, and M. Matsumura, “Excimer-Laser-Induced Lateral-Growth of Silicon Thin-Films,” *Japanese Journal of Applied Physics*, vol. 37, no. Part 1, No. 3A, pp. 731–736, 1998.

[12] M. Keevers, T. Young, U. Schubert, and M. A. Green, “10% Efficient CSG Minimodules,” presented at the 22nd European Photovoltaic Solar Energy Conference, Milan, 2007.

[13] K. Ellmer, A. Klein, and B. Rech, *Transparent Conductive Zinc Oxide: Basics and Applications in Thin Film Solar Cells*. Springer, 2008.

[14] R. A. Street, *Hydrogenated Amorphous Silicon*. Cambridge University Press, 2005.

[15] T. F. Schulze, “Structural, electronic and transport properties of amorphous/crystalline silicon heterojunctions,” PhD thesis, Technische Universität Berlin, 2011.

[16] D. E. Polk and D. S. Boudreaux, “Tetrahedrally Coordinated Random-Network Structure,” *Physical Review Letters*, vol. 31, no. 2, pp. 92–95, Jul. 1973.

[17] P. A. Fedders and D. A. Drabold, “Theory of boron doping in a-Si:H,” *Physical Review B*, vol. 56, no. 4, pp. 1864–1867, Jul. 1997.

[18] K. Winer, R. A. Street, N. M. Johnson, and J. Walker, “Impurity incorporation and doping efficiency in a-Si:H,” *Physical Review B*, vol. 42, no. 5, pp. 3120–3128, Aug. 1990.

[19] T. Sontheimer, “Design of electron beam evaporated Si thin films for solid phase crystallized solar cells on glass,” PhD thesis, Technische Universität Berlin, Berlin, 2011.

[20] Akihisa Matsuda, Katsuhiko Nomoto, Yoshiaki Takeuchi, Atsushi Suzuki, Akimasa Yuuki, and J. Perrin, “Temperature dependence of the sticking and loss probabilities of silyl radicals on hydrogenated amorphous silicon,” *Surface Science*, vol. 227, no. 1–2, pp. 50–56, Mar. 1990.

[21] A. G. Dirks and H. J. Leamy, “Columnar microstructure in vapor-deposited thin films,” *Thin Solid Films*, vol. 47, no. 3, pp. 219–233, Dec. 1977.

[22] D. Henderson, M. H. Brodsky, and P. Chaudhari, “Simulation of structural anisotropy and void formation in amorphous thin films,” *Applied Physics Letters*, vol. 25, no. 11, pp. 641–643, Dec. 1974.

[23] M. Werner, U. Schubert, C. Hagendorf, M. Schneider, M. Keevers, and R. Egan, “Thin Film Morphology, Growth and Defect Structure of e-Beam Deposited Silicon on Glass,” presented at the 24th European Photovoltaic Solar Energy Conference, Hamburg, 2009, pp. 2482 – 2485.

[24] C. C. Tsai, J. C. Knights, G. Chang, and B. Wacker, “Film formation mechanisms in the plasma deposition of hydrogenated amorphous silicon,” *Journal of Applied Physics*, vol. 59, no. 8, pp. 2998–3001, Apr. 1986.

[25] C. Becker, T. Sontheimer, S. Steffens, S. Scherf, and B. Rech, “Polycrystalline silicon thin films by high-rate electronbeam evaporation for photovoltaic applications – Influence of substrate texture and temperature,” *Energy Procedia*, vol. 10, no. 0, pp. 61–65, 2011.

[26] C. Becker, F. Ruske, T. Sontheimer, B. Gorka, U. Bloeck, S. Gall, and B. Rech, “Microstructure and photovoltaic performance of polycrystalline silicon thin films on temperature-stable ZnO:Al layers,” *Journal of Applied Physics*, vol. 106, no. 8, pp. 084506–084506–7, Oct. 2009.

[27] C. Spinella, S. Lombardo, and F. Priolo, “Crystal grain nucleation in amorphous silicon,” *Journal of Applied Physics*, vol. 84, no. 10, pp. 5383–5414, Nov. 1998.

[28] G. L. Olson and J. A. Roth, “Kinetics of solid phase crystallization in amorphous silicon,” *Materials Science Reports*, vol. 3, no. 1, pp. 1–77, 1988.

[29] D. T. Wu, “The time lag in nucleation theory,” *The Journal of Chemical Physics*, vol. 97, no. 4, pp. 2644–2650, Aug. 1992.

[30] C. Agashe, O. Kluth, J. Hüpkes, U. Zastrow, B. Rech, and M. Wuttig, “Efforts to improve carrier mobility in radio frequency sputtered aluminum doped zinc oxide films,” *Journal of Applied Physics*, vol. 95, no. 4, pp. 1911–1917, Feb. 2004.

[31] O. Kluth, B. Rech, L. Houben, S. Wieder, G. Schöpe, C. Beneking, H. Wagner, A. Löffl, and H. . Schock, “Texture etched ZnO:Al coated glass substrates for silicon based thin film solar cells,” *Thin Solid Films*, vol. 351, no. 1–2, pp. 247–253, Aug. 1999.

[32] O. Kluth, G. Schöpe, J. Hüpkes, C. Agashe, J. Müller, and B. Rech, “Modified Thornton model for magnetron sputtered zinc oxide: film structure and etching behaviour,” *Thin Solid Films*, vol. 442, no. 1–2, pp. 80–85, Oct. 2003.

[33] M. Wimmer, “Thermische Nachbehandlung von aluminiumdotiertem Zinkoxid und die Silizium/Zinkoxid-Grenzfläche,” PhD thesis, Technische Universität Berlin, 2011.

[34] M. Berginski, “Lichtstreuende Oberflächen, Schichten und Schichtsysteme zur Verbesserung der Lichteinkopplung in Silizium-Dünnschichtsolarzellen,” PhD thesis, Rheinisch-Westfälischen Technischen Hochschule Aachen, 2007.

[35] E. Burstein, “Anomalous Optical Absorption Limit in InSb,” *Physical Review*, vol. 93, no. 3, pp. 632–633, Feb. 1954.

[36] T. S. Moss, “The Interpretation of the Properties of Indium Antimonide,” *Proceedings of the Physical Society. Section B*, vol. 67, no. 10, pp. 775–782, Oct. 1954.

[37] K. H. Kim, K. C. Park, and D. Y. Ma, “Structural, electrical and optical properties of aluminum doped zinc oxide films prepared by radio frequency magnetron sputtering,” *Journal of Applied Physics*, vol. 81, no. 12, pp. 7764–7772, Jun. 1997.

[38] M. Suchea, S. Christoulakis, N. Katsarakis, T. Kitsopoulos, and G. Kiriakidis, “Comparative study of zinc oxide and aluminum doped zinc oxide transparent thin films grown by direct current magnetron sputtering,” *Thin Solid Films*, vol. 515, no. 16, pp. 6562–6566, Jun. 2007.

[39] B. E. Sernelius, K.-F. Berggren, Z.-C. Jin, I. Hamberg, and C. G. Granqvist, “Band-gap tailoring of ZnO by means of heavy Al doping,” *Physical Review B*, vol. 37, no. 17, pp. 10244–10248, Jun. 1988.

[40] W. Yang, Z. Wu, Z. Liu, A. Pang, Y.-L. Tu, and Z. C. Feng, “Room temperature deposition of Al-doped ZnO films on quartz substrates by radio-frequency magnetron sputtering and effects of thermal annealing,” *Thin Solid Films*, vol. 519, no. 1, pp. 31–36, Oct. 2010.

[41] A. Einstein, “Über einen die Erzeugung und Verwandlung des Lichtes betreffenden heuristischen Gesichtspunkt,” *Annalen der Physik*, vol. 322, no. 6, pp. 132–148, 1905.

[42] NREL RReDC, “Reference Solar Spectral Irradiance: Air Mass 1.5.” [Online]. Available: http://rredc.nrel.gov/solar/spectra/am1.5/.

[43] C. J. Chen, “Appendix E: AM1.5 Reference Solar Spectrum,” in *Physics of Solar Energy*, John Wiley & Sons, Inc., 2011, pp. 307–312.

[44] M. A. Green, *Solar cells: operating principles, technology, and system applications*. Prentice-Hall, 1982.

[45] H.-G. Wagemann and H. Eschrich, *Photovoltaik: Solarstrahlung und Halbleitereigenschaften, Solarzellenkonzepte und Aufgaben*. Springer, 2007.

[46] A. Banerjee, T. Su, D. Beglau, G. Pietka, F. Liu, G. DeMaggio, S. Almutawalli, B. Yan, G. Yue, J. Yang, and S. Guha, “High efficiency, multi-junction nc-Si:H based solar cells at high deposition rate,” in *2011 37th IEEE Photovoltaic Specialists Conference (PVSC)*, 2011, p. 003583.

[47] T. F. Schulze, L. Korte, F. Ruske, and B. Rech, “Band lineup in amorphous/crystalline silicon heterojunctions and the impact of hydrogen microstructure and topological disorder,” *Physical Review B*, vol. 83, no. 16, p. 165314, Apr. 2011.

[48] Y. Tawada, M. Kondo, H. Okamoto, and Y. Hamakawa, “Hydrogenated amorphous silicon carbide as a window material for high efficiency a-Si solar cells,” *Solar Energy Materials*, vol. 6, no. 3, pp. 299–315, Mar. 1982.

[49] Y. Tawada, H. Okamoto, and Y. Hamakawa, “a-SiC:H/a-Si:H heterojunction solar cell having more than 7.1% conversion efficiency,” *Applied Physics Letters*, vol. 39, no. 3, pp. 237–239, Aug. 1981.

[50] R. Biron, C. Pahud, F.-J. Haug, J. Escarré, K. Söderström, and C. Ballif, “Window layer with p doped silicon oxide for high Voc thin-film silicon n-i-p solar cells,” *Journal of Applied Physics*, vol. 110, no. 12, pp. 124511–124511–7, Dec. 2011.

[51] M. L. Terry, D. Inns, and A. G. Aberle, “Rapid Thermal Annealing and Hydrogen Passivation of Polycrystalline Silicon Thin-Film Solar Cells on Low-Temperature Glass,” *Advances in OptoElectronics*, vol. 2007, pp. 1–11, 2007.

[52] B. Rau, T. Weber, B. Gorka, P. Dogan, F. Fenske, K. Y. Lee, S. Gall, and B. Rech, “Development of a rapid thermal annealing process for polycrystalline silicon thin-film solar cells on glass,” *Materials Science and Engineering: B*, vol. 159–160, no. 0, pp. 329–332, Mar. 2009.

[53] B. Gorka, B. Rau, P. Dogan, C. Becker, F. Ruske, S. Gall, and B. Rech, “Influence of Hydrogen Plasma on the Defect Passivation of Polycrystalline Si Thin Film Solar Cells,” *Plasma Processes and Polymers*, vol. 6, no. S1, pp. S36–S40, 2009.

[54] C. Becker, H. Häberlein, G. Schöpe, J. Hüpkes, and B. Rech, “Contact resistivity measurements of the buried Si–ZnO:Al interface of polycrystalline silicon thin-film solar cells on ZnO:Al,” *Thin Solid Films*, vol. 520, no. 4, pp. 1268–1273, Dec. 2011.

[55] H. Lüth, *Solid Surfaces, Interfaces and Thin Films*. Springer, 2001.

[56] S. Hüfner, S. Schmidt, and F. Reinert, “Photoelectron spectroscopy—An overview,” *Nuclear Instruments and Methods in Physics Research Section A: Accelerators, Spectrometers, Detectors and Associated Equipment*, vol. 547, no. 1, pp. 8–23, Jul. 2005.

[57] S. Hüfner, *Photoelectron Spectroscopy: Principles and Applications*. Springer, 2003.

[58] D. Attwood, *Soft X-Rays and Extreme Ultraviolet Radiation: Principles and Applications*. Cambridge University Press, 2007.

[59] D. Briggs and M. P. Seah, *Practical Surface Analysis: Auger and X-ray photoelectron spectroscopy*. Wiley, 1983.

[60] C. D. Wagner, “Auger parameter in electron spectroscopy for the identification of chemical species,” *Analytical Chemistry*, vol. 47, no. 7, pp. 1201–1203, Jun. 1975.

[61] C. D. Wagner, “Auger lines in x-ray photoelectron spectrometry,” *Analytical Chemistry*, vol. 44, no. 6, pp. 967–973, May 1972.

[62] G. Moretti, “Auger parameter and Wagner plot in the characterization of chemical states by X-ray photoelectron spectroscopy: a review,” *Journal of Electron Spectroscopy and Related Phenomena*, vol. 95, no. 2–3, pp. 95–144, Oct. 1998.

[63] C. D. Wagner, L. H. Gale, and R. H. Raymond, “Two-dimensional chemical state plots: a standardized data set for use in identifying chemical states by x-ray photoelectron spectroscopy,” *Analytical Chemistry*, vol. 51, no. 4, pp. 466–482, Apr. 1979.

[64] O. Renner and J. Zemek, “Density of amorphous silicon films,” *Czechoslovak Journal of Physics*, vol. 23, no. 11, pp. 1273–1276, Nov. 1973.

[65] S. Tougaard, *QUASES-IMFP-TPP2M*. 2002.

[66] S. Tanuma, C. J. Powell, and D. R. Penn, “Calculations of electron inelastic mean free paths. V. Data for 14 organic compounds over the 50–2000 eV range,” *Surface and Interface Analysis*, vol. 21, no. 3, pp. 165–176, 1994.

[67] S. Ueda, Y. Katsuya, M. Tanaka, H. Yoshikawa, Y. Yamashita, S. Ishimaru, Y. Matsushita, and K. Kobayashi, “Present Status of the NIMS Contract Beamline BL15XU at SPring-8,” *AIP Conference Proceedings*, vol. 1234, no. 1, pp. 403–406, Jun. 2010.

[68] F. Schaefers, M. Mertin, and M. Gorgoi, “KMC-1: a high resolution and high flux soft x-ray beamline at BESSY,” *Review of Scientific Instruments*, vol. 78, no. 12, p. 123102, Dec. 2007.

[69] M. Gorgoi, S. Svensson, F. Schäfers, G. Öhrwall, M. Mertin, P. Bressler, O. Karis, H. Siegbahn, A. Sandell, H. Rensmo, W. Doherty, C. Jung, W. Braun, and W. Eberhardt, “The high kinetic energy photoelectron spectroscopy facility at BESSY progress and first results,” *Nuclear Instruments and Methods in Physics Research Section A: Accelerators, Spectrometers, Detectors and Associated Equipment*, vol. 601, no. 1–2, pp. 48–53, Mar. 2009.

[70] M. Gorgoi, S. Svensson, F. Schäfers, W. Braun, and W. Eberhardt, “Hard X-ray high kinetic energy photoelectron spectroscopy at the KMC-1 beamline at BESSY,” *The European Physical Journal - Special Topics*, vol. 169, no. 1, pp. 221–225, 2009.

[71] H. Stöcker, *Taschenbuch der Physik: Formeln, Tabellen, Übersichten*. Deutsch, 2004.

[72] “Correspondence with Mihaela Gorgoi.”

[74] F. Kronast, J. Schlichting, F. Radu, S. k. Mishra, T. Noll, and H. a. Dürr, “Spin-resolved photoemission microscopy and magnetic imaging in applied magnetic fields,” *Surface and Interface Analysis*, vol. 42, no. 10–11, pp. 1532–1536, 2010.

[75] M. O. Krause, “Average L-shell fluorescence, Auger, and electron yields,” *Physical Review A*, vol. 22, no. 5, pp. 1958–1961, Nov. 1980.

[76] F. Evangelisti, F. Patella, R. A. Riedel, G. Margaritondo, P. Fiorini, P. Perfetti, and C. Quaresima, “Core Excitons in Amorphous Semiconductors,” *Physical Review Letters*, vol. 53, no. 26, pp. 2504–2507, Dec. 1984.

[77] W. Eberhardt, G. Kalkoffen, C. Kunz, D. Aspnes, and M. Cardona, “Photoemission Studies of 2p Core Levels of Pure and Heavily Doped Silicon,” *physica status solidi (b)*, vol. 88, no. 1, pp. 135–143, 1978.

[78] B. L. Henke, E. M. Gullikson, and J. C. Davis, “X-Ray Interactions: Photoabsorption, Scattering, Transmission, and Reflection at E = 50-30,000 eV, Z = 1-92,” *Atomic Data and Nuclear Data Tables*, vol. 54, no. 2, pp. 181–342, Jul. 1993.

[79] M. Bär, L. Weinhardt, O. Fuchs, J. Klaer, J. Peiser, H.-W. Schock, and C. Heske, “Chemical Bath Deposition of CdS Thin Films on Cuins2 and Si Substrates - A Comparative X-Ray Emission Study,” in *Conference Record of the 2006 IEEE 4th World Conference on Photovoltaic Energy Conversion*, 2006, vol. 1, pp. 416 –419.

[80] Lawrence Berkeley National Laboratory, “X-Ray Attenuation Length,” 2012. [Online]. Available: http://henke.lbl.gov/optical_constants/atten2.html.

[81] J. J. Jia, T. A. Callcott, J. Yurkas, A. W. Ellis, F. J. Himpsel, M. G. Samant, J. Stöhr, D. L. Ederer, J. A. Carlisle, E. A. Hudson, L. J. Terminello, D. K. Shuh, and R. C. C. Perera, “First experimental results from IBM/TENN/TULANE/LLNL/LBL undulator beamline at the advanced light source,” *Review of Scientific Instruments*, vol. 66, no. 2, pp. 1394–1397, Feb. 1995.

[82] Advanced Light Source, “High Resolution and Flux for Materials and Surface Science Beamline 8.0.1,” 2009. [Online]. Available: http://www.als.lbl.gov/als/als_users_bl/8.0.1-Overview.pdf.

[83] Advanced Light Source, “Soft X-Ray Fluorescence (SXF) Spectrometer • Beamline 8.0.1,” 2009. [Online]. Available: http://www.als.lbl.gov/als/als_users_bl/8.0.1-SXF.pdf.

[84] M. Boots, *ALS sxedaq*. University of Saskatchewan.

[85] A. Bianconi, “Core excitons and inner well resonances in surface soft x-ray absorption (SSXA) spectra,” *Surface Science*, vol. 89, no. 1–3, pp. 41–50, 1979.

[86] R. Loudon, “The Raman effect in crystals,” *Advances in Physics*, vol. 50, no. 7, pp. 813–864, 2001.

[87] R. Bisaro, J. Magario, K. Zellama, S. Squelard, P. Germain, and J. F. Morhange, “Solid-phase crystallization kinetics in doped a-Si chemical-vapor-deposition films,” *Physical Review B*, vol. 31, no. 6, pp. 3568–3575, Mar. 1985.

[88] S. Huang, S. Xu, Q. Cheng, J. Long, and K. Ostrikov, “Aluminum-assisted crystallization and *p*-type doping of polycrystalline Si,” *Applied Physics A: Materials Science & Processing*, vol. 97, no. 2, pp. 375–380, Nov. 2009.

[89] Z. Iqbal, S. Vepřek, A. P. Webb, and P. Capezzuto, “Raman scattering from small particle size polycrystalline silicon,” *Solid State Communications*, vol. 37, no. 12, pp. 993–996, Mar. 1981.

[90] I. H. Campbell and P. M. Fauchet, “The effects of microcrystal size and shape on the one phonon Raman spectra of crystalline semiconductors,” *Solid State Communications*, vol. 58, no. 10, pp. 739–741, Jun. 1986.

[91] E. Bustarret, M. A. Hachicha, and M. Brunel, “Experimental determination of the nanocrystalline volume fraction in silicon thin films from Raman spectroscopy,” *Applied Physics Letters*, vol. 52, no. 20, pp. 1675–1677, May 1988.

[92] C.-Y. Peng, C.-F. Huang, Y.-C. Fu, Y.-H. Yang, C.-Y. Lai, S.-T. Chang, and C. W. Liu, “Comprehensive study of the Raman shifts of strained silicon and germanium,” *Journal of Applied Physics*, vol. 105, no. 8, pp. 083537–083537–10, Apr. 2009.

[93] D. Abou-Ras, R. Caballero, C.-H. Fischer, C. a. Kaufmann, I. Lauermann, R. Mainz, H. Mönig, A. Schöpke, C. Stephan, C. Streeck, S. Schorr, A. Eicke, M. Döbeli, B. Gade, J. Hinrichs, T. Nunney, H. Dijkstra, V. Hoffmann, D. Klemm, V. Efimova, A. Bergmaier, G. Dollinger, T. Wirth, W. Unger, A. a. Rockett, A. Perez-Rodriguez, J. Alvarez-Garcia, V. Izquierdo-Roca, T. Schmid, P.-P. Choi, M. Müller, F. Bertram, J. Christen, H. Khatri, R. w. Collins, S. Marsillac, and I. Kötschau, "Comprehensive Comparison of Various Techniques for the Analysis of Elemental Distributions in Thin Films," *Microscopy and Microanalysis*, vol. 17, no. 05, pp. 728–751, 2011.

[94] D. Abou-Ras, U. Rau, and T. Kirchartz, *Advanced Characterization Techniques for Thin Film Solar Cells*. John Wiley & Sons, 2011.

[95] V. Randle and O. Engler, *Introduction to Texture Analysis:: Macrotexture, Microtexture, and Orientation Mapping, Second Edition*. Taylor & Francis, 2009.

[96] D. Abou-Ras, U. Jahn, M. Nichterwitz, T. Unold, J. Klaer, and H.-W. Schock, "Combined electron backscatter diffraction and cathodoluminescence measurements on CuInS2/Mo/glass stacks and CuInS2 thin-film solar cells," *Journal of Applied Physics*, vol. 107, no. 1, pp. 014311–014311–8, Jan. 2010.

[97] S. Sadewasser, D. Abou-Ras, D. Azulay, R. Baier, I. Balberg, D. Cahen, S. Cohen, K. Gartsman, K. Ganesan, J. Kavalakkatt, W. Li, O. Millo, T. Rissom, Y. Rosenwaks, H.-W. Schock, A. Schwarzman, and T. Unold, "Nanometer-scale electronic and microstructural properties of grain boundaries in Cu(In,Ga)Se-2," *Thin Solid Films*, vol. 519, no. 21, pp. 7341–7346, Aug. 2011.

[98] C. Ossadnik, S. Vepřek, and I. Gregora, "Applicability of Raman scattering for the characterization of nanocrystalline silicon," *Thin Solid Films*, vol. 337, no. 1–2, pp. 148–151, Jan. 1999.

[99] J.-E. Rubensson, D. Mueller, R. Shuker, D. L. Ederer, C. H. Zhang, J. Jia, and T. A. Callcott, "Excitation-energy dependence in the L2,3 fluorescence spectrum of Si," *Physical Review Letters*, vol. 64, no. 9, pp. 1047–1050, Feb. 1990.

[100] P. A. Bruhwiler and S. E. Schnatterly, "Empirical application of Dyson's equation to the L2,3 soft-x-ray–emission transition densities of states of c-Si and a-Si:H," *Physical Review B*, vol. 39, no. 17, pp. 12649–12654, Jun. 1989.

[101] R. S. Crisp and D. Haneman, "Band structures, gap states and doping effects in amorphous hydrogenated and crystalline silicon studied by soft X-ray emission," *Journal of Physics: Condensed Matter*, vol. 3, no. 48, pp. 9637–9650, Dec. 1991.

[102] WaveMetrics, *IGOR Pro*. .

[103] H. Richter, Z. P. Wang, and L. Ley, "The one phonon Raman spectrum in microcrystalline silicon," *Solid State Communications*, vol. 39, no. 5, pp. 625–629, Aug. 1981.

[104] R. J. Kobliska and S. A. Solin, "Raman Spectrum of Wurtzite Silicon," *Physical Review B*, vol. 8, no. 8, pp. 3799–3802, Oct. 1973.

[105] M. N. Islam and S. Kumar, “Influence of crystallite size distribution on the micro-Raman analysis of porous Si,” *Applied Physics Letters*, vol. 78, no. 6, p. 715, 2001.

[106] M. Wojdyr, *fityk*. .

[107] C. V. Thompson, “Grain Growth in Thin Films,” *Annual Review of Materials Science*, vol. 20, no. 1, pp. 245–268, 1990.

[108] R. B. Bergmann, F. G. Shi, H. J. Queisser, and J. Krinke, “Formation of polycrystalline silicon with log-normal grain size distribution,” *Applied Surface Science*, vol. 123–124, pp. 376–380, Jan. 1998.

[109] L. Houben, M. Luysberg, and R. Carius, “Microtwinning in microcrystalline silicon and its effect on grain-size measurements,” *Physical Review B*, vol. 67, no. 4, p. 045312, Jan. 2003.

[110] M. Bär, M. Wimmer, R. G. Wilks, M. Roczen, D. Gerlach, F. Ruske, K. Lips, B. Rech, L. Weinhardt, M. Blum, S. Pookpanratana, S. Krause, Y. Zhang, C. Heske, W. Yang, and J. D. Denlinger, “Impact of solid-phase crystallization of amorphous silicon on the chemical structure of the buried Si/ZnO thin film solar cell interface,” *Applied Physics Letters*, vol. 97, no. 7, pp. 072105–072105–3, Aug. 2010.

[111] M. Wimmer, M. Bär, D. Gerlach, R. G. Wilks, S. Scherf, C. Lupulescu, F. Ruske, R. Félix, J. Hüpkes, G. Gavrila, M. Gorgoi, K. Lips, W. Eberhardt, and B. Rech, “Hard x-ray photoelectron spectroscopy study of the buried Si/ZnO thin-film solar cell interface: Direct evidence for the formation of Si–O at the expense of Zn-O bonds,” *Applied Physics Letters*, vol. 99, no. 15, pp. 152104–152104–3, Oct. 2011.

[112] L. Ley, J. Reichardt, and R. L. Johnson, “Static Charge Fluctuations in Amorphous Silicon,” *Physical Review Letters*, vol. 49, no. 22, pp. 1664–1667, Nov. 1982.

[113] T. C. Chiang and F. J. Himpsel, “2.1 Band structure and core levels of tetrahedrally-bonded semiconductors,” in *Landolt-Börnstein - Group III Condensed Matter*, vol. 23a, A. Goldmann and E.-E. Koch, Eds. Berlin/Heidelberg: Springer-Verlag, pp. 15–20.

[114] R. S. Crisp, D. Haneman, and V. Chacornt, “Direct observation of gap states in a-Si: H through the Si L2,3 soft X-ray emission spectrum,” *Journal of Physics C: Solid State Physics*, vol. 21, no. 5, pp. 975–985, Feb. 1988.

[115] J. T. Sullivan, R. G. Wilks, M. T. Winkler, L. Weinhardt, D. Recht, A. J. Said, B. K. Newman, Y. Zhang, M. Blum, S. Krause, W. L. Yang, C. Heske, M. J. Aziz, M. Bär, and T. Buonassisi, “Soft x-ray emission spectroscopy studies of the electronic structure of silicon supersaturated with sulfur,” *Applied Physics Letters*, vol. 99, no. 14, pp. 142102–142102–3, Oct. 2011.

[116] M. Wimmer, D. Gerlach, R. G. Wilks, S. Scherf, R. Félix, C. Lupulescu, F. Ruske, G. Schondelmaier, K. Lips, J. Hüpkes, M. Gorgoi, W. Eberhardt, B. Rech, and M. Bär, “Chemical interaction at the buried silicon/zinc oxide thin-film solar cell interface as revealed by hard x-ray photoelectron spectroscopy,” *Submitted to Journal of Electron Spectroscopy and Related Phenomena*, Jun. 2012.

[117] J. Robertson, “Electronic structure of silicon nitride,” *Philosophical Magazine Part B*, vol. 63, no. 1, pp. 47–77, 1991.

[118] V. A. Gritsenko, Y. N. Morokov, and Y. N. Novikov, “Electronic structure of amorphous Si3N4: experiment and numerical simulation,” *Applied Surface Science*, vol. 113–114, no. 0, pp. 417–421, Apr. 1997.

[119] T. Sontheimer, C. Becker, U. Bloeck, S. Gall, and B. Rech, “Crystallization kinetics in electron-beam evaporated amorphous silicon on ZnO:Al-coated glass for thin film solar cells,” *Applied Physics Letters*, vol. 95, no. 10, Sep. 2009.

[120] O. Nast and A. J. Hartmann, “Influence of interface and Al structure on layer exchange during aluminum-induced crystallization of amorphous silicon,” *Journal of Applied Physics*, vol. 88, no. 2, pp. 716–724, Jul. 2000.

[121] A. Klein, C. Körber, A. Wachau, F. Säuberlich, Y. Gassenbauer, R. Schafranek, S. P. Harvey, and T. O. Mason, “Surface potentials of magnetron sputtered transparent conducting oxides,” *Thin Solid Films*, vol. 518, no. 4, pp. 1197–1203, Dec. 2009.

[122] National Institute of Standards and Technology, “NIST X-ray Photoelectron Spectroscopy (XPS) Database.” [Online]. Available: http://srdata.nist.gov/xps/Default.aspx.

[123] S. B. Amor, M. Jacquet, P. Fioux, and M. Nardin, “XPS characterisation of plasma treated and zinc oxide coated PET,” *Applied Surface Science*, vol. 255, no. 9, pp. 5052–5061, Feb. 2009.

[124] J. J. Yeh and I. Lindau, “Atomic subshell photoionization cross sections and asymmetry parameters: $1 \leqslant Z \leqslant 103$,” *Atomic Data and Nuclear Data Tables*, vol. 32, no. 1, pp. 1–155, Jan. 1985.

[125] J. F. Moulder, W. F. Stickle, and P. E. Sobol, *Handbook of X-ray Photoelectron Spectroscopy*, 1992nd ed. Perkin-Elmer, Physical Electronics Division, 1992.

[126] R. A. Street, C. C. Tsai, J. Kakalios, and W. B. Jackson, “Hydrogen diffusion in amorphous silicon,” *Philosophical Magazine Part B*, vol. 56, no. 3, pp. 305–320, 1987.

[127] C. Virojanadara and L. I. Johansson, “Studies of oxidized hexagonal SiC surfaces and the SiC/SiO2 interface using photoemission and synchrotron radiation,” *Journal of Physics: Condensed Matter*, vol. 16, no. 17, pp. S1783–S1814, May 2004.

[128] T. Eickhoff, “Photoemissionsuntersuchungen an vergrabenen Grenzschichten SiO2/Si, SiO2/SiC und Thiolen auf Gold mit 3,0–5,5 keV Röntgenstrahlung,” Dissertation, Universität Hamburg, 2002.

[129] B. Li, Y. Adachi, J. Li, H. Okushi, I. Sakaguchi, S. Ueda, H. Yoshikawa, Y. Yamashita, S. Senju, K. Kobayashi, M. Sumiya, H. Haneda, and N. Ohashi, “Defects in ZnO transparent conductors studied by capacitance transients at ZnO/Si interface,” *Applied Physics Letters*, vol. 98, no. 8, pp. 082101–082101–3, Feb. 2011.

[130] M. Bär, B.-A. Schubert, B. Marsen, R. G. Wilks, S. Pookpanratana, M. Blum, S. Krause, T. Unold, W. Yang, L. Weinhardt, C. Heske, and H.-W. Schock, “Cliff-like conduction band offset and KCN-induced recombination barrier enhancement at the CdS/Cu2ZnSnS4 thin-film solar cell heterojunction,” *Applied Physics Letters*, vol. 99, no. 22, pp. 222105–222105–3, Nov. 2011.

[131] Y. Igarashi, T. Yamaji, and S. Nishikawa, “A New Mechanism of Failure in Silicon p+/n Junction Induced by Diffusion Barrier Metals,” *Japanese Journal of Applied Physics*, vol. 29, pp. L2337–L2340, 1990.

Publications

M. Bär, M. Wimmer, R. G. Wilks, M. Roczen, D. Gerlach, F. Ruske, K. Lips, B. Rech, L. Weinhardt, M. Blum, S. Pookpanratana, S. Krause, Y. Zhang, C. Heske, W. Yang, and J. D. Denlinger, "Impact of solid-phase crystallization of amorphous silicon on the chemical structure of the buried Si/ZnO thin film solar cell interface," *Applied Physics Letters*, vol. 97, no. 7, pp. 072105–072105–3, Aug. 2010.

M. Wimmer, M. Bär, D. Gerlach, R. G. Wilks, S. Scherf, C. Lupulescu, F. Ruske, R. Félix, J. Hüpkes, G. Gavrila, M. Gorgoi, K. Lips, W. Eberhardt, and B. Rech, "Hard x-ray photoelectron spectroscopy study of the buried Si/ZnO thin-film solar cell interface: Direct evidence for the formation of Si–O at the expense of Zn-O bonds," *Applied Physics Letters*, vol. 99, no. 15, pp. 152104–152104–3, Oct. 2011.

X. Song, R. Caballero, R. Félix, D. Gerlach, C. A. Kaufmann, H.-W. Schock, R. G. Wilks, and M. Bär, "Na incorporation into Cu(In,Ga)Se2 thin-film solar cell absorbers deposited on polyimide: Impact on the chemical and electronic surface structure," *Journal of Applied Physics*, vol. 111, no. 3, pp. 034903–034903–8, Feb. 2012.

M. Wimmer, D. Gerlach, R. G. Wilks, S. Scherf, R. Félix, C. Lupulescu, F. Ruske, G. Schondelmaier, K. Lips, J. Hüpkes, M. Gorgoi, W. Eberhardt, B. Rech, and M. Bär, "Chemical interaction at the buried silicon/zinc oxide thin-film solar cell interface as revealed by hard x-ray photoelectron spectroscopy," *Submitted to Journal of Electron Spectroscopy and Related Phenomena*, Jun. 2012.

D. Gerlach, D. Wippler, R. G. Wilks, M. Wimmer, M. Lozac'h, R. Félix, S. Ueda, H. Yoshikawa, K. Lips, B. Rech, M. Sumiya, K. Kobayashi, M. Gorgoi, J. Hüpkes, and M. Bär, "p-type a-Si:H/ZnO:Al and µc-Si:H/ZnO:Al Thin-film Solar Cell Structures – A Comparative Hard X-ray Photoelectron Spectroscopy Study," *Submitted to IEEE Journal of Photovoltaics*, Jun. 2012.

Conferences

D. Gerlach, M. Wimmer, R. G. Wilks, T. F. Schulze, M. Roczen, Y. Zhang, F. Ruske, M. Blum, S. Pookpanratana, S. Krause, W. Yang, J. D. Denlinger, K. Lips, L. Weinhardt, C. Heske, B. Rech, and M. Bär, "Influence of solid phase crystallization on the chemical structure of the deeply buried Si/ZnO interface," *25th European Photovoltaic Solar Energy Conference*, Valencia, Spain, Sept. 2010 – Poster presentation

D. Gerlach, M. Wimmer, S. Hass, R. Félix, K. Lips, B. Rech, L. Tati Bismaths, J. Herrero-Albillos, F. Kronast, R. G. Wilks, M. Bär, J. P. Theisen, F. Erfurth, F. Reinert, and L. Weinhardt, "Chemical micro-structure of interfaces in thin-film solar cells investigated by PEEM," *Joint BER II and BESSY II Users' Meetings*, Berlin, Germany, Dec. 2010. – Poster presentation

D. Gerlach, M. Wimmer, R. G. Wilks, C. Becker, T. F. Schulze, M. Blum, L. Weinhardt, W. Yang, F. Ruske, K. Lips, C. Heske, B. Rech, and M. Bär, "Solid-phase crystallization of amorphous silicon thin-film solar cell absorbers studied by soft x-ray emission spectroscopy," *Advanced Light Source User Meeting*, Berkeley, USA, 2011. – Poster presentation

D. Gerlach, M. Wimmer, R. G. Wilks, C. Becker, T. F. Schulze, M. Blum, L. Weinhardt, W. Yang, F. Ruske, K. Lips, C. Heske, B. Rech, and M. Bär, "Monitoring solid-phase crystallization of amorphous silicon: Impact of deposition temperature and chemical changes in the Si/ZnO structure," *26th European Photovoltaic Solar Energy Conference*, Hamburg, Germany, Sept. 2011 – Poster presentation

D. Gerlach, D. Wippler, R. G. Wilks, M. Wimmer, M. Lozac'h, R. Félix, S. Ueda, H. Yoshikawa, K. Lips, B. Rech, M. Sumiya, K. Kobayashi, M. Gorgoi, J. Hüpkes, and M. Bär, "Electronic structure of the p-type amorphous and microcrystalline Si:H/ZnO:Al interface," *38th IEEE Photovoltaic Specialists Conference*, Austin, USA, Jun. 2012 – Oral presentation
(Best Student Award in Area 5: Thin Film Based PV Technologies)

Acknowledgements

First of all I want to thank Marcus Bär for the opportunity to work in this newly formed, international group and for supervising this PhD thesis.

Regan Wilks I'd like to thank for the fruitful discussions along the way and his patience in correcting Germish out of this thesis.

Mark Wimmer I want to thank for his patience in supplying humongous amounts of samples, the fruitful discussions and companionship especially during long HIKE beamtime shifts.

Roberto Félix has been a great co-PhD-student and I enjoyed working and sharing an office with him.

Special thanks go to the beamline scientists Mihaela Gorgoi (HIKE, BESSY II), Florian Kronast (SPEEM, BESSY II) and Wanli Yang (Beamline 8.0, ALS) for using their endstations and helpful advice during beamtimes.

For providing samples and input during experimentation and interpretation I would like to thank Christiane Becker (HZB), David Wippler and Jürgen Hüpkes (Forschungszentrum Jülich).

For EBSD I'd like to thank Daniel Abou-Ras and for Raman spectroscopy measurements Janis Jeanne Merkel.

All members of the "extended Clemens Heske group" from Würzburg, Karlsruhe and Las Vegas I would like to thank for their collaboration and the companionship during ALS beamtimes and at the IEEE PVSC conference in Austin.

Thanks to all past and present members of the Young Investigator Group Interface Design (EN-1) for the helping hand - be it in the lab, at beamtimes or with data evaluation.

I'd like to thank Dieter Schmeißer for reading and commenting on the draft of this thesis.

Special thanks go to my parents, my brother and the rest of my family for their support through all my life.